CHAPTER 3
ELMy H-MODE OPERATION IN JET

D. C. McDONALD,[a]* Y. ANDREW,[a] G. T. A. HUYSMANS,[b] A. LOARTE,[c]
J. ONGENA,[d] J. RAPP,[e] and S. SAARELMA[a]

[a]*Euratom/UKAEA Fusion Association, Culham Science Centre, Abingdon*
 Oxfordshire OX14 3DB, United Kingdom
[b]*Association Euratom-CEA, CEA/DSM/DRFC, Centre de Cadarache*
 13108 St. Paul lez Durance, France
[c]*EFDA Close Support Unit Garching, Boltzmannstrasse 2*
 D-85748 Garching bei München, Germany
[d]*LPP-ERM/KMS, Euratom-Belgian State Association, Brussels, Belgium*
[e]*Forschungszentrum Jülich GmbH, Euratom Association, Jülich, Germany*

A wide range of studies on JET have contributed greatly to the development of the ELMy H-mode as a high-performance scenario for fusion devices and to the understanding of the physical processes that underlie it. Development has focused on the production of a high-performance, high-density, stationary scenario suited to deuterium-tritium operation and with small edge energy loads. Physics studies have made strong progress in the understanding of the L-H threshold, energy confinement, *pedestal physics, and edge-localized mode behavior. A strong focus of this work has been providing a basis for extrapolation to future machines, such as ITER, for which, as the largest existing tokamak, JET has been of particular importance.*

KEYWORDS: *H-mode, confinement, ELMs*

Note: Some figures in this paper are in color only in the electronic version.

Contents—Chapter 3

*E-mail: dmcd@jet.uk

I. INTRODUCTION

ELMy H-modes have been widely studied at JET for more than 20 years. The principal aim has been to understand the physics of the mode sufficient for it to be optimized and scaled up to future burning plasma experiments and reactors.

I.A. The H-Mode

The H-mode, discovered in the ASDEX tokamak[1] in 1982, is a mode of plasma operation with high energy confinement times and is characterized by an edge transport barrier. It is often associated with edge phenomena known as edge-localized modes.

The energy confinement time τ_E is the ratio of the plasma stored energy to the power flowing out across its edge. If the energy confinement time were unaffected by changes to plasma parameters, it would represent the decay time for the stored energy. However, in practice this is never the case. The energy confinement time is a key plasma performance parameter because of its relationship to the fusion product Q. The fusion product, defined as the ratio of the power produced by a burning plasma to that put into it, is a measure of the efficiency of a burning plasma. For fusion reactors, it can be shown[2] that, approximately, $Q \propto nT\tau_E$, where n is the plasma density and T is the plasma temperature. Thus, understanding and optimizing the energy confinement time is crucial to maximizing the predicted power in a fusion reactor or burning plasma experiment, such as ITER (Ref. 3).

When auxiliary heating is applied to a plasma, it usually begins in a mode of operation with a relatively low energy confinement time, known as the L-mode. The local energy transport in L-mode plasmas comes from turbulent transport processes (see Chap. 10 in this issue[4]). If the power is increased sufficiently, the plasma will undergo a transition to a higher confinement mode of operation, known as the H-mode. The power required to achieve this transition is known as the L-H threshold power, P_{L-H}. One reason for the improved confinement in H-modes is the existence of an edge transport barrier (ETB). An ETB, also known as a pedestal, is a region of reduced energy transport, localized to the plasma edge, resulting from the suppression of turbulent transport by sheared flows in the poloidal direction. ETBs are formed at the L-H transition and are characteristic to all H-modes. Usually, they are regulated by periodic relaxations of the plasma edge by processes known as edge-localized modes (ELMs). During ELMs, the high density and temperature gradients and large currents of the ETBs trigger magnetohydrodynamic (MHD) instabilities. These gradients are reduced as particles and energy leave the plasma during the resulting ELM crash. In ELMy H-modes, the edge gradients will then begin to increase before the whole process is repeated. The particles and energy released during the ELM crash result in highly spatially and temporally localized deposits of energy on plasma-facing components. The parameter space for ELMy H-mode operation is restricted by global MHD instabilities, discussed in Chap. 8 in this issue,[5] and by density limits. A reliable empirical scaling for the density limit has been determined, known as the Greenwald density limit,[6] n_{Gr}. However, sometimes the true density limit can differ markedly from this simple scaling.

The challenge for ELMy H-mode development is to produce ELMy H-modes that extrapolate to burning plasma experiments such as ITER. To do so, they must satisfy several constraints in one integrated scenario. These include having high energy confinement and ELM losses small enough to avoid damage to plasma-facing

components. Central to these two constraints is the role of the ETB. Broadly speaking, increasing the strength of the ETB increases the plasma confinement and, at the same time, increases the ELM losses. Optimizing ELMy H-mode performance requires either balancing these two effects or finding ELMy H-modes that break this correlation.

I.B. JET H-Mode Studies

From studies performed on ASDEX (Ref. 1), H-mode operation was known to be associated with single-null diverted plasmas with ion ∇B drift toward the X-point. While still operating as a limiter machine, JET was able to produce single-null, and indeed double-null, discharges that resulted in H-modes with good confinement properties.[7,8] With neutral beam injection (NBI) heating, plasmas were produced at plasma currents of 5 MA with 11 MJ of stored energy.[9] H-modes heated with ion cyclotron resonant heating (ICRH) alone were also produced.[10] However, the resulting H-modes were found to contain high levels of impurities and to be relatively unsteady. This was resolved by the conversion of JET to a diverted machine during its refurbishment during 1992 through 1994.

Since 1994, JET has operated as a diverted machine, enabling it to consistently produce high-performance, near-stationary H-modes.[11] Stationary operation has focused on ELMy H-modes, particularly on type I and type III ELMy H-modes[12] (see Sec. IV for the definitions of ELM types). These regimes are characterized by near-stationary operation, the ability to obtain low impurity content (Z_{eff} below 2.0), and high confinement. Performing beryllium evaporations and glow discharges ≈ 2 to 3 times a week has proved vital for reducing impurity levels. ELMy H-modes have become the workhorse for near-stationary, high-performance operation on JET. In conjunction with other machines, extensive studies led to the development of the IPB98(y,2) empirical scaling for their energy confinement time, $\tau_{98(y,2)}$ (Ref. 13). During deuterium-tritium operation in 1997, a JET ELMy H-mode produced stationary operation with ion and electron temperatures ≈ 10 keV, ≈ 4 MW of fusion energy, and a fusion product of $Q \approx 0.22$, which still stands as a record.[14] Results showed that the energy confinement, the pedestal pressure, and the power required to achieve the ELMy H-mode all scaled favorably with isotope mass. JET has operated with several different divertor designs, and these have been found to have a relatively small impact on energy confinement,[15] but a larger effect on edge conditions and $P_{L\text{-}H}$ (Ref. 12). JET results have contributed to the adoption of a high-triangularity, high-density, ELMy H-mode as the baseline scenario for ITER (Ref. 3) and continue to improve the physics basis for this scenario.

Studies showing that the ELMy H-mode performance was improved by increasing triangularity δ in the range $\delta = 0.14$ to 0.38 (Ref. 16) led to the development of even higher triangularity, $\delta \geq 0.4$, ELMy H-mode scenarios. Performance at these triangularities was indeed found to be improved. One such type I ELMy H-mode discharge had parameters of $H_{98(y,2)} \approx 1.0$, $\overline{n_e} \geq 0.85 n_{Gr}$, and $\beta_N \approx 1.8$ in stationary operation,[17,18] corresponding to meeting the conditions for the ITER baseline scenario. Here $H_{98(y,2)}$ is the energy confinement time normalized to the IPB98(y,2) scaling, $\overline{n_e}$ is the line average electron density, and β_N is the normalized thermal plasma pressure. High-triangularity, $\delta \geq 0.4$, experiments also led to the first observations of type I-II ELMy H-modes in JET (Ref. 18) with reduced ELM frequencies at high density. Dimensionless transport studies, in conjunction with DIII-D, have supported the case for obtaining higher ITER performance through increasing the normalized pressure β of the operating point.[19]

Particle and energy losses during ELMs have been widely studied. For type I ELMs they have been found to scale with local pedestal parameters.[20] The resultant high divertor heat loads have also been extensively studied (see Chap. 6 in this issue[21]), leading to concerns over the suitability of some ELMy H-mode regimes in larger machines. This, in turn, has led to the development of ELMy H-modes with lower divertor power loads than those of type I ELMy H-modes. These include grassy ELMy H-modes,[22] type II ELMy H-modes,[22] impurity-seeded type III ELMy H-modes,[23] ELMy H-modes with ELMs triggered by pellets,[24] and ELMy H-modes with ELMs triggered by magnetic field perturbations.[25] All of these have been found to have reduced divertor power loads. However, grassy ELMy H-modes so far have been observed only in a small, high-collisionality region of parameter space, type II ELMy H-modes may also be restricted by collisionality; and impurity-seeded type III ELMy H-modes have been observed to have a somewhat lower confinement than an equivalent type I ELMy H-mode. Despite this, an impurity-seeded ELMy H-mode has reached parameters indicating that it may be scaled up to an ITER deuterium-tritium discharge with a fusion product of $Q \approx 10$. ELMy H-modes triggered with pellets and magnetic field perturbations show promising results that may apply to mainstream type I ELMy H-mode scenarios. Further development is required before they can be assessed as ITER-viable techniques.

Scenarios with confinement improvements from edge pedestals but without ELMs have also been explored at JET. These include the hot-ion H-mode[26] and the VH mode.[27,28] Both scenarios have been found to have confinement in excess of equivalent ELMy H-mode discharges but, due to the absence of ELMs to regulate the pedestal, have always been transient. They are not discussed in this paper. Steady "quiescent" H-modes (short QH-mode) have been achieved on JET (Ref. 29), and these will be discussed here.

The rest of this chapter is organized as follows: Sections II through VI describe the advances made at JET in the understanding of global energy confinement (Sec. II),

the L-H threshold (Sec. III), pedestal and ELM physics (Sec. IV), transport during ELMs (Sec. V), and the MHD properties of the ELMs (Sec. VI). Section VII describes attempts to mitigate the potentially harmful energy loading of the divertor and wall that result from ELM crashes. Section VIII reviews experiments on plasmas with a radiative mantle. In Sec. IX, the results are summarized and conclusions drawn. Sections I, II, IV, and IX were written by D. C. McDonald, Sec. III by Y. Andrew, Sec. V by A. Loarte, Sec. VI by G. T. A. Huysmans and S. Saarelma, Sec. VII by J. Rapp, and Sec. VIII by J. Ongena.

II. ENERGY CONFINEMENT

JET began operation, in 1983, as a limiter machine with ohmic plasmas and then, as first ICRH and then NBI heating were added in 1985 and 1986, with L-mode plasmas. Thus, confinement studies began on ohmic plasmas[30] and then L-modes with ICRH (Ref. 31) and NBI heating.[32] These studies showed that JET had achieved energy confinement times τ_E up to 0.8 s, in advance of those seen on previous, smaller machines, with confinement decreasing with increasing input power and increasing with increasing plasma current I_p, as shown in Fig. 1 (Ref. 33). These observations were broadly in line with previously derived multimachine scalings,[34] increasing confidence in the extrapolation of these scalings to next-step devices. Transport studies found that temperature

Fig. 2. Time traces of the D_α signal (arbitrary units) and the electron temperature (keV) for given r, the radius normalized to the radius of the plasma. The sudden decrease in the D_α signal marks the onset of the H-mode, and it is seen that the electron temperature undergoes an increase in slope simultaneously over a large part of the radius. (From Ref. 37.)
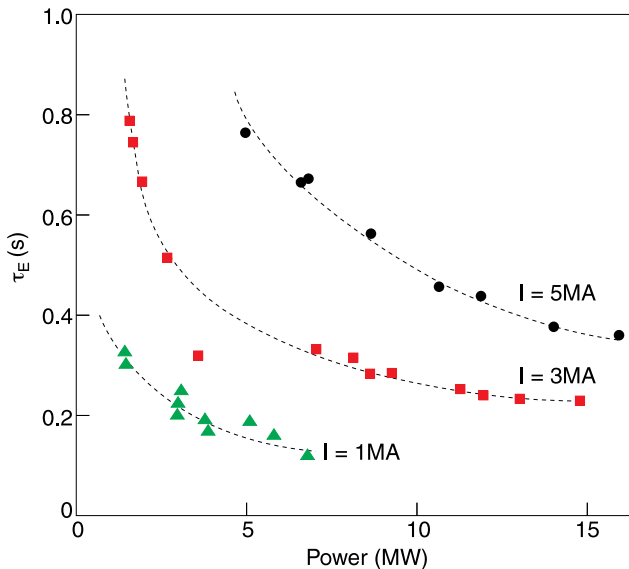

Fig. 1. The confinement time plotted against heating power for a series of JET L-mode limiter plasmas with three different plasma currents: 1 (triangles), 3 (squares), and 5 MA (circles). The dashed lines represent $\tau_E \propto P^{-\alpha}$ fits to the data for each value of plasma current. (From Ref. 33.)
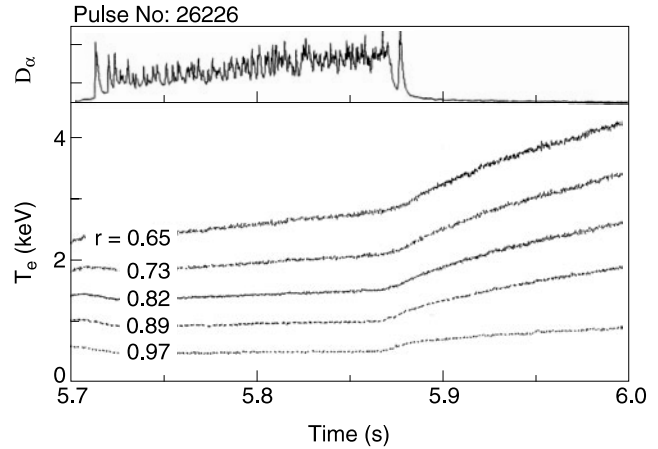
profiles were largely consistent with a scaling based on a semiempirical fit to a critical temperature gradient model.[35] These scalings predict relatively modest performance for power plants, motivating the study of higher-confinement regimes. The H-mode,[1] already known to improve confinement on several other tokamaks, was seen as a promising regime in this respect. Indeed, studies performed before the installation of the JET divertor found that confinement in H-modes had confinement times typically twice those in L-mode discharges.[8] The installation of the JET divertor resulted in more steady ELMy H-mode plasmas, which greatly facilitated confinement studies. An early and surprising discovery was that the transition to H-mode has been observed to be associated with an almost instantaneous increase in plasma confinement across much of the plasma radius.[36,37] This can be seen from Fig. 2, where, following the L-H mode transition at 5.87 s, identified by the sudden decrease in the D_α radiation, the electron temperature undergoes a sudden increase in its temporal growth rate at almost all radii. This change in behavior is much faster than a confinement time, which is typically hundreds of milliseconds, and studies found that it could be described by local transport models only if unrealistic dependencies on temperature or temperature gradient were assumed.[36,37] Thus, observed rapid transition suggests that nonlocal transport effects, such as turbulence spreading,[38–40] are present at the L-H transition. The ETB or H-mode pedestal, Fig. 3, plays a crucial role in ELMy H-mode confinement in JET. Although this role is discussed in relation to specific effects in this section, the general contribution of the pedestal to confinement is described in Sec. IV.
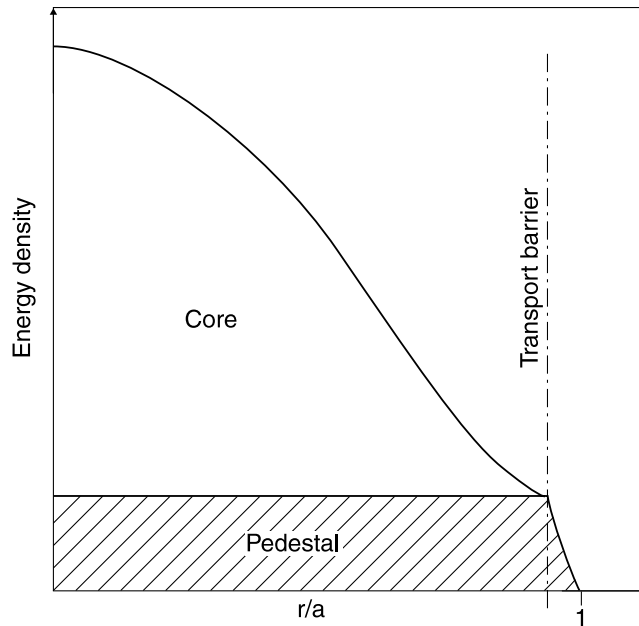
Fig. 3. An idealized profile of the energy density for a JET ELMy H-mode. The ETB is indicated. The energy confined by the transport barrier at the edge (pedestal; hashed region) and that confined in the plasma core (core) are also shown (From Ref. 66.)

In addition to H-modes, several other high-confinement regimes have been studied. These scenarios have improved core confinement, often from an internal transport barrier, and are generally referred to as advanced scenarios. Such scenarios have a higher bootstrap fraction than equivalent H-modes and so are believed to be suited to steady-state power plant operation. Advanced scenarios exhibit confinement in excess of that observed for equivalent ELMy H-modes, although they tend to be transient. Their confinement properties on JET are not discussed here; instead, the reader is referred to Chap. 4 of this issue.[41] More recently, the "hybrid" scenario has been developed on JET. This mode has many properties common to ELMy H-modes—high confinement through an ETB, stationary operation, and ELMs—but has a higher bootstrap fraction, making it better suited to very long pulse power plant operation. Again, "hybrid" scenario confinement properties are not discussed further in this paper, and the reader is once more referred to Chap. 4 of this issue.[41]

II.A. Diagnosis of Confinement

JET confinement studies rely on a wide range of diagnostics and analysis methods to determine the transport properties of its plasmas. Electron density n_e measurements are provided by an eight-channel interferometry system[42] and a lidar Thomson scattering system.[43] Z_{eff} is measured by charge-exchange spectroscopy[44] and by visible spectroscopy of bremsstrahlung radiation.[45] The fractional concentration of hydrogenic and helium species are also measured with visible spectroscopy. Electron temperature T_e measurements are taken from the lidar Thomson scattering system or from electron cyclotron emission diagnostics.[46–48] Ion temperature T_i is measured with charge-exchange spectroscopy and X-ray crystal spectrometry.[49,50] Radiated power is measured with a bolometry system[51] and neutron emissions using neutron yield monitors.[52] Equilibria are currently reconstructed using the EFIT code[53] based on data from magnetic coils,[54] with the IDENT code[55] being used for this purpose prior to 1994. Fast particle energies are calculated from the PENCIL (Ref. 56) and PION (Ref. 57) codes—or a fitted formula[58]—and removed from the diamagnetic energy measurement to give the plasma thermal energy. Pedestal diagnosis, used to determine energy confinement in the pedestal region, is discussed in Sec. IV.

II.B. Influence of Divertor Design, Configuration, and Shape

JET has operated with three divertor designs, beginning with the relatively open MkI (Ref. 59) and moving to the more closed MkII (Ref. 12) and the gas box MkIIGB (Ref. 60) designs. Poloidal cross sections of these three divertor designs are summarized in Fig. 1 of Ref. 21. The MkII divertor was modified slightly during its first year, from its original MkIIA design to its final MkIIAP design.[12] All of these divertors have enabled stationary ELMy H-modes, in contrast to the pre-1994 undiverted plasmas, which tended to be nonstationary. A survey of ELMy H-modes from all three divertors showed that MkI and MkII diverted plasmas had similar confinement properties but that plasmas in the MkIIGB divertor had a slightly higher confinement. This can be seen in Fig. 4, where the energy confinement times, normalized to the IPB98(y,2) scaling[13] $\tau_{E,98(y,2)}$, are plotted against the line average electron density $\overline{n}_e$, normalized to the Greenwald density limit[6] n_{Gr}. It can be seen that the normalized confinement time for plasmas with the MkIIGB divertor lie systematically above those of the MkI and MkII divertors. However, the effect is weak, with an estimated improvement of only $\approx 8\%$. Further, determination of the size of the effect is affected by the fact that because of the nature of the permissible magnetic configurations in a given divertor design, plasmas tended to have different shapes and volumes from one design to another. Plasma geometry is known to affect confinement, and this is accounted for in the analyses by expressing confinement relative to a multimachine confinement scaling that includes geometry. However, the confidence that can be placed in the resulting confinement change is limited by both uncertainties in the scalings and variations between the geometrical scalings of JET and the multimachine scaling.
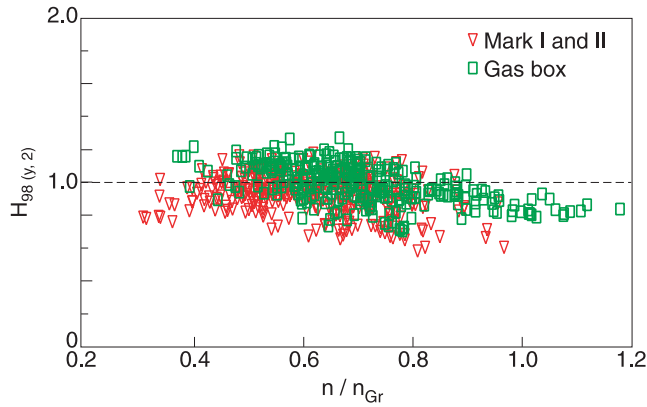
Fig. 4. $H_{98(y,2)}$ ($\equiv \tau_E/\tau_{E,98(y,2)}$) versus $\overline{n_e}/n_{Gr}$ for a data set of JET type I ELMy H-modes. MkI and MkII (triangles) and MkIIGB (squares) divertor data are shown. (From Ref. 15.)

Fig. 5. Degradation of the normalized confinement $H_{98(y,2)}$ as a function of plasma density for a series of gas scans with edge triangularity from 0.14 to 0.46. Data for triangularity up to 0.38 were obtained with the MkIIA JET divertor. The highest-triangularity, 0.46, data were obtained with the MkIIGB divertor. Open symbols correspond to type III ELMs. Electron density was taken from the lidar diagnostic[43] both for n_e and in the calculation of $H_{98(y,2)}$. (From Ref. 18.)

JET ELMy H-modes have been produced with a wide range of strike point configurations and varying divertor flux expansions. A dedicated study was performed on plasmas in the MkII divertor, involving a series of discharges with plasma current of 2.5 MA and toroidal field of 2.5 T, heated by ≈12 MW of NBI power only. The discharges had magnetic configurations with a range of strike point positions and flux expansions and triangularities δ that varied from 0.20 to 0.32. Analysis indicated that the impact of the magnetic configuration on plasma confinement was weak and acted through the moderation of ELM frequency.[12] Energy confinement was found to decrease with increasing ELM frequency, with the ELM frequency itself appearing to be dependent on magnetic configuration. No reproducible dependency on strike point position or flux expansion could be determined, but a clear decrease in ELM frequency with increasing triangularity was observed.

Further JET studies have confirmed a positive influence of triangularity on confinement. The most extensive set of comparison discharges was composed of discharges performed with the MkII and MkIIGB divertors.[16,18] The MkII divertor discharges have plasma current of 2.6 MA and toroidal field of 2.7 T, heated by ≈12 MW of NBI power only. Gas fueling was used to produce a range of densities in three configurations with triangularities of 0.14, 0.23, and 0.38. The MkIIGB divertor discharges have plasma current of 2.5 MA and toroidal field of 2.7 T and are heated by ≈15 MW of NBI power only. Gas fueling was again used to produce a density scan, in a configuration in which triangularity was 0.47. Figure 5 shows the confinement time, normalized to the IPB98(y,2) scaling, plotted against the line average density normalized to the Greenwald density limit. Normalized confinement decreases with increasing density in all of these gas-fueled density scans, but it is clear that there is a general increase in confinement with increasing tri-

angularity, for the same density. In addition, the achievable density also increases with triangularity. The analysis of these discharges indicates that triangularity acts on confinement through its effect on the edge pedestal. For the δ ≈ 0.14 to 0.38 discharges, type I ELM frequency decreases with increasing triangularity. This is associated with an increase in pedestal confinement, which is in qualitative agreement with modeling, based on neoclassical transport in the pedestal region, with the pedestal gradient limited by MHD stability.[61] In the highest-triangularity (δ ≈ 0.46) discharges, which were with the MkIIGB divertor, mixed type I-II ELMs are observed. Studies varying upper and lower triangularity separately suggest that upper triangularity seems to have the stronger effect.[62] The complexity of the impact of triangularity on confinement, together with its relation to the effect of density and gas fueling, does not make it well suited to be expressed by a simple scaling. Attempts have been made to derive such a scaling for JET (Refs. 15 and 16), but these have not been found to extrapolate to other machines.

The variation in plasma elongation permitted by the JET vessel design is relatively limited, but a study was performed in the MkIIGB divertor with elongation κ varied by 19%, from 1.55 to 1.85 (Ref. 63). This was performed with the MkIIGB divertor at fixed current,

1.8 MA, and safety factor, $q_{95} \approx 3.3$, where q_{95} is the safety factor q at the surface with normalized flux of 0.95. Results showed that confinement improved with increasing elongation by 15%, in line with the multi-machine scaling IPB98(y,2) of $\tau_E \propto \kappa^{0.78}$. A point to note here is that because of the link between safety factor and elongation, $q \approx \kappa B/I$, the magnetic field varied across this scan. Thus, the magnitude of the elongation scaling is somewhat sensitive to the assumed field scaling. However, the impact of this effect on the measured confinement is estimated to be relatively small, $<3\%$.

Taken together, the results of this subsection support high-triangularity, high-elongation magnetic configurations, in a relatively closed divertor, as the most favorable mode of operation for high-performance ELMy H-modes. This is indeed the magnetic configuration and divertor design adopted by ITER.

II.C. Effect of Ion Species

Following hydrogen and deuterium L-mode experiments, which showed a weak increase in confinement with increasing hydrogen isotope mass,[64] ELMy H-mode confinement studies were performed with matched discharges in hydrogen, deuterium, and tritium.[16] These studies were performed with the MkII divertor, with gas fueling and NBI-only heating of 10 to 12 MW. Figure 6

shows the confinement times for these discharges, normalized to the ITER97-P(y) scaling,[65] versus the density normalized to the Greenwald density limit. The ITER97-P(y) scaling has a weak isotopic mass M scaling of $\tau_E \propto M^{0.20}$. Although the density dependence of the discharges is not well represented by that of the ITER97-P(y) scaling, it can be seen that the isotopic mass dependence is broadly in line with this scaling. The impact of isotopic mass on confinement appears to be dominated by its effect on the edge pedestal. ELM frequency was found to decrease with increasing atomic mass for equivalent hydrogen, deuterium and tritium discharges. Associated with the different ELM frequencies, the pedestal pressure was seen to increase with increasing isotopic mass. This can be seen in Fig. 7, where the electron temperature at the pedestal top is plotted against the electron density at the pedestal top for a series of hydrogen, deuterium, and tritium discharges. Curves of constant electron pressure are plotted also. The trend is clearly for the pedestal pressure to increase with increasing mass, indicating an improvement in pedestal confinement. This is discussed more fully in Sec. IV.B. A study of the core confinement for the same discharges found that it decreased slightly with increasing isotopic mass.[66] Deuterium-tritium ELMy H-mode discharges were also found to follow the $\tau_E \propto M^{0.20}$ trend, and one of these discharges, pulse 42983, was able to achieve a fusion product in stationary conditions
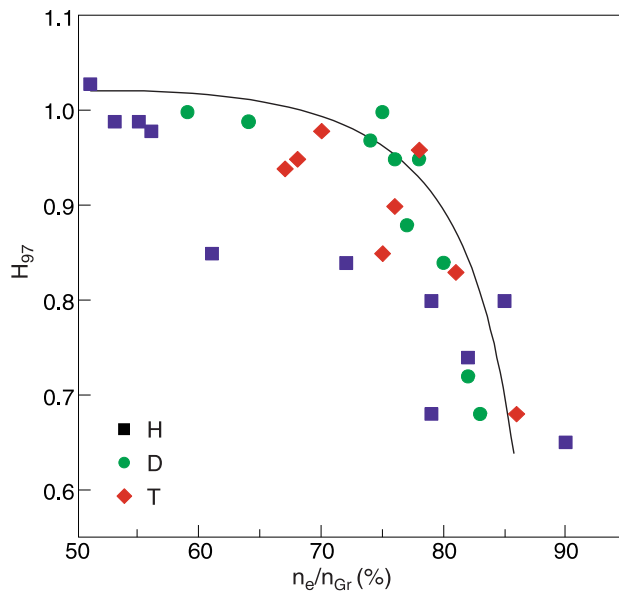

Fig. 6. Confinement normalized to ITER97-P(y) scaling, H_{97}, as a function of the density scaled to the Greenwald density limit. Data taken during stationary phases of hydrogen (squares), deuterium (circles), and tritium (diamonds) plasmas. The data set in the figure includes discharges with $1.7 \leq I_p$ (MA) and $B_T \leq 3$ T. All the discharges included have $q_{95} \approx 3.3$ and NBI power of 10 to 12 MW. (From Ref. 16.)
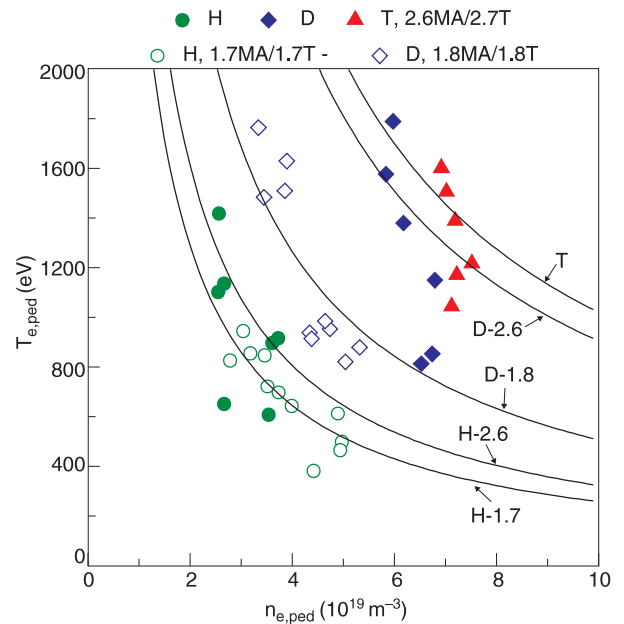

Fig. 7. The maximum edge pedestal n_e and T_e for five series of gas scans at fixed plasma shape. Closed symbols, 2.6 MA and 2.7 T in hydrogen, deuterium, and tritium; open symbols, 1.7 MA and 1.7 T in hydrogen and 1.8 MA and 1.8 T in deuterium. The n_e and T_e data are from lidar profiles at the fixed major radius of 3.75 m. (From Ref. 16.)

of $Q \approx 0.22$, which remains the record value. JET's confirmation of the scaling of isotopic mass to tritium and deuterium-tritium discharges is of particular importance for increasing confidence in the extrapolation of deuterium-only experiments to ITER.

As well as hydrogenic ion species, JET has studied the confinement properties of ELMy H-modes in ^{4}He (Ref. 67). A series of type I ELMy H-mode helium plasmas and deuterium-only reference plasmas were produced with the MkIIGB divertor, with $q_{95} \approx 3.3$ and plasma current and fields of 1 MA/1 T, 1.8 MA/1.8 T, and 2 MA/2 T. The deuterium discharges were heated by deuterium NBI only, and the ^{4}He discharges by ^{4}He NBI with, in one discharge, some additional ICRH. The ^{4}He discharges were found to have lower confinement than an equivalent deuterium plasma. Figure 8 shows the confinement time normalized to IPB98(y,2) scaling, $H_{98(y,2)}$, against the mean ion charge Z for these discharges. The ^{4}He plasmas clearly have poorer confinement, consistent with a scaling of $\tau_E \propto Z^{-0.75 \pm 0.08}$. This would imply that ^{4}He plasmas have poorer confinement than an equivalent hydrogen plasma. Interestingly, these results contrast with L-mode studies of ^{3}He plasmas, which found them to have confinement times similar to those for deuterium plasmas.[64] Type III ELMy H-modes were also observed in ^{4}He and were found to have an approximately 35% lower confinement than that of equivalent type I ELMy H-modes. The H-mode density limit in ^{4}He plasmas was

also studied and found to be broadly similar to that for an equivalent deuterium plasma.[68]

Although there is no value in operating power plants in helium plasmas, the JET experiments were motivated by an interest in operating ITER in ^{4}He, in contrast to hydrogen, during its initial low-activation phase. The results indicated that operation was possible, with performance somewhat below a hydrogen plasma but with a more favorable L-H mode threshold. However, the very different edge and divertor physics observed in ^{4}He plasmas[69] mean that these results will be difficult to extrapolate to deuterium and deuterium-tritium operation. As a result, early operation in hydrogen seems the preferred option for ITER.

II.D. Density and Fueling Effects

Fueling on JET is predominantly from gas injection at the edge. In addition, there is some contribution from NBI, when applied, and some experiments have been performed with direct pellet injection, in which small pellets of frozen deuterium are injected directly into the plasma core. The improvement in fusion performance with density means that good confinement at high density is a key requirement for ITER and power plant plasmas. JET has achieved high confinement, $H_{98(y,2)} \approx 1$, at densities approaching and exceeding the Greenwald density limit using high triangularity,[16,17] density peaking,[70] and pellets.[71–73]

In relation to the moderately positive density scalings found in the multimachine scalings, such as $\tau_E \propto \bar{n}_e^{0.41}$ for IPB98(y,2), JET ELMy H-mode confinement is generally observed to decrease with increasing density for gas-fueled discharges.[16,17,63] This can be seen in Figs. 5 and 6, where the normalized confinement decreases with increasing density for gas scans of hydrogen, deuterium, and tritium discharges in magnetic configurations of varying triangularity with both the MkII and MkIIGB divertors. For the tritium discharges in Fig. 6, there is some evidence of agreement with the IPB98(y,2) scaling at low density, followed by decreasing confinement relative to IPB98(y,2) at higher density, but in general a fairly steady decrease is observed with no sign of agreement with the scalings, even at low density. This behavior can be explained by either of the following:

1. confinement in these plasmas having a density dependence different from that of the IPB98(y,2) scaling

2. gas fueling having a negative impact on the pedestal confinement.[74]

An increase in type I ELM frequency with increasing gas fueling is observed in most JET scans with, at the highest fueling levels, a transition to type III ELMs. As result of this, high confinement at high density cannot usually be achieved through gas fueling of JET discharges, but a
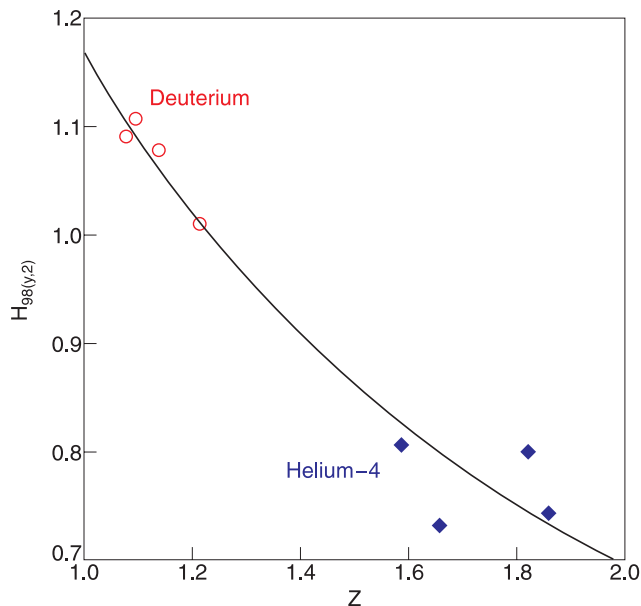

Fig. 8. Dependence of the energy confinement time on mean isotope charge for JET MkIIGB ^{4}He (diamonds) and deuterium reference (circles) type I ELMy H-mode plasmas. The confinement time is normalized to the ELMy H-mode scaling IPB98(y,2). The solid line represents a $H_{98(y,2)} \propto Z^{-0.75}$ scaling. (From Ref. 67.)

number of different strategies to achieve this have been developed. The most successful of these strategies, so far, has been increasing triangularity, as discussed in Sec. II.B.

An alternative method explored at JET for achieving high confinement at densities in excess of the Greenwald limit has been through increased density peaking.[70] This has been achieved through moderated gas fueling of a type I ELMy H-mode leading to a steady increase of density peaking over time. Figure 9 shows an example of a discharge that used this recipe to achieve $H_{98(y,2)} \approx 0.96$ at $\overline{n_e}/n_{Gr} \approx 1.0$ and $\beta_N \approx 2$, where $\beta_N \equiv 100 aB\beta/I_p$ is the normalized β, with β being the ratio of the plasma pressure to the magnetic pressure, and a is the plasma minor radius. This discharge was with the MkIIGB divertor, with a high-triangularity magnetic configuration ($\delta \approx$ 0.5), plasma current and field of 1.9 MA and 2 T, and ≈ 10 MW of NBI heating. Density can be seen to increase throughout the full heating phase, with relatively little change in confinement. Although such discharges are stationary over several confinement times, density is always evolving, and if heated for long enough, they will terminate when reaching a MHD or density limit.

Pellet injection has also been used to achieve high confinement and high density on JET (Refs. 71, 72, and 73). This method has proved to be successful at pushing density above the Greenwald limit. However, as for the gas fueling experiments, normalized confinement has been observed to decrease with increasing density.

The physics of the H-mode density limit itself has also been studied.[75] A database of gas-fueled JET dis-

charges that reached the density limit was created mainly from dedicated density limit studies. Because density limits are primarily an edge phenomenon, the edge pedestal density was taken as the determining parameter. The density limit studies were performed at a range of magnetic fields, plasma currents, heating powers, and triangularities. The H-mode density limit was defined at the transition from type III ELMy H-mode back to L-mode, rather than the confinement limitation at the transition from type I to type III ELMy H-mode. Divertor detachment (see Chap. 6 of this issue[21]) was observed to be associated with these transitions and so is believed to be the physics mechanism responsible for the H-mode density limits. By combining with data from ASDEX Upgrade experiments, a database suitable for extrapolation to ITER was produced. Although the Greenwald density limit was found to be in the correct absolute range to the observed H-mode density limits, it was a relatively poor predictor. A direct empirical fit to the database showed a markedly different scaling to the Greenwald density limit scaling and was found to be a significantly better predictor. This empirical scaling has been compared to a model, based on the detachment process described by a simple two-point model in the scrape-off layer (SOL). This so-called BLS-model was found to be in good agreement with the empirical scaling derived from the experimental database.[75] Extrapolation to ITER led to an unfavorable lower density limit prediction in the baseline scenario. However, correlations in the database and the small number (two) of machines from which the database was drawn mean that these predictions cannot be made with
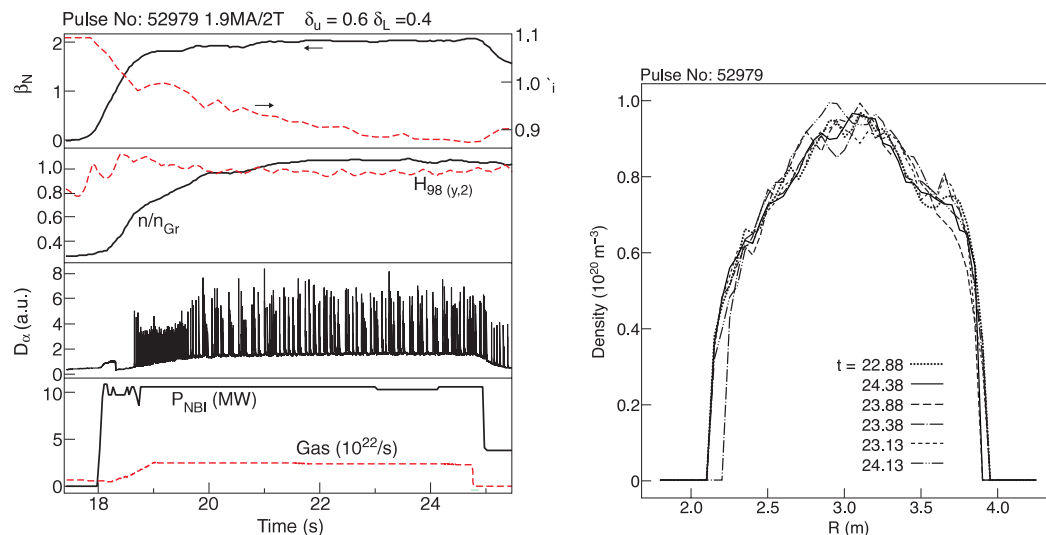
Fig. 9. Data from a quasi-stationary ELMy H-mode plasma at the Greenwald density limit. The figure on the left shows time traces of plasma parameters: top, normalized plasma pressure (solid line) and internal inductance (dashed line); second panel, line average electron density scaled to the Greenwald density limit (solid line) and energy confinement time normalized to the IPB98(y,2) scaling[13] (dashed line); third panel, D_α emission from the outer divertor region; and bottom, injected NBI power (solid line) and gas fueling rate (dashed line). The figure on the right shows the electron density against radial position for a line of sight near to the plasma midplane at six different time points. (From Ref. 70.)

confidence. The results do give concern regarding the use of the Greenwald density limit to predict the H-mode density limit on ITER and indicate that further studies are required before confident estimates can be made.

II.E. Effect of Heating Schemes

JET ELMy H-modes have been dominantly heated by both NBI and ICRH. The JET NBI system comprises two beam boxes, each with eight positive ion neutral injectors. These can be configured to launch hydrogen, deuterium, tritium, and helium, with a variety of energies, typically in the range 80 to 160 keV. The maximum injected power for the whole system, so far, is 23 MW. JET has operated with two ICRH antennae, but the results reported here relate to the post-1994 system (see Chap. 9 of this issue[76]). This comprises four antennae, each with four current straps. The system allows monopole, dipole, and quadrupole phasing. Fundamental and second-harmonic hydrogen, ^{3}He, and second-harmonic tritium minority heating schemes[77] have all been used to heat H-modes.

To assess the impact of the two heating schemes on confinement, studies that varied the ratio of ICRH/NBI have been performed.[78–80] The most extensive of these was performed with the MkIIGB divertor and involved varying the ratio of the two heating schemes while keeping their combined power level at 11 to 12 MW (Ref. 80). ICRH power varied from 0 to 10 MW and NBI from 11 to 1.2 MW. The ICRH scheme was on-axis minority hydrogen heating at ≈ 42 MHz. A single-null, moderate

triangularity ($\delta \approx 0.25$) configuration was used with plasma current and field of 2.0 MA and 2.6 to 2.7 T. Density was kept fixed through use of some small gas fueling, 90% deuterium and 10% hydrogen combining to give $\approx 10^{21}$ electrons$\cdot$s^{-1}. Figure 10a shows the global confinement results, with normalized confinement decreasing with increasing NBI fraction. The total decrease in confinement across the scan is only 10%, which is comparable to the estimated error of the measurements. Local transport analyses, Fig. 10b, show that the ions are the dominant loss channel, and no significant dependence of ion thermal diffusivity upon the ICRH/NBI ratio is observed. The ELM behavior did not vary greatly across the scan and the pedestal pressure remained constant. The mild improvement in confinement with increased ICRH power fraction was explained by the more on-axis heating of the ICRH. The impact of toroidal torque and toroidal rotation, which would have correlated positively with the fraction of NBI power, on the energy confinement was not studied. In common with the other studies, this would suggest that choice of heating scheme does not greatly affect the confinement but that confinement does increase slightly with increasing ICRH fraction.

Related to the heating scheme used is the impact of the ratio of electron to ion temperature on confinement. Several JET studies of this effect have been performed.[81,82] One such study[81] took a set of moderate triangularity ($\delta \approx 0.3$) with plasma current and field of 2.8 MA and 2.8 T. NBI and on-axis minority hydrogen ICRH at ≈ 42 MHz was used to vary the ratio of the electron to ion temperature, at the radius where square root–normalized
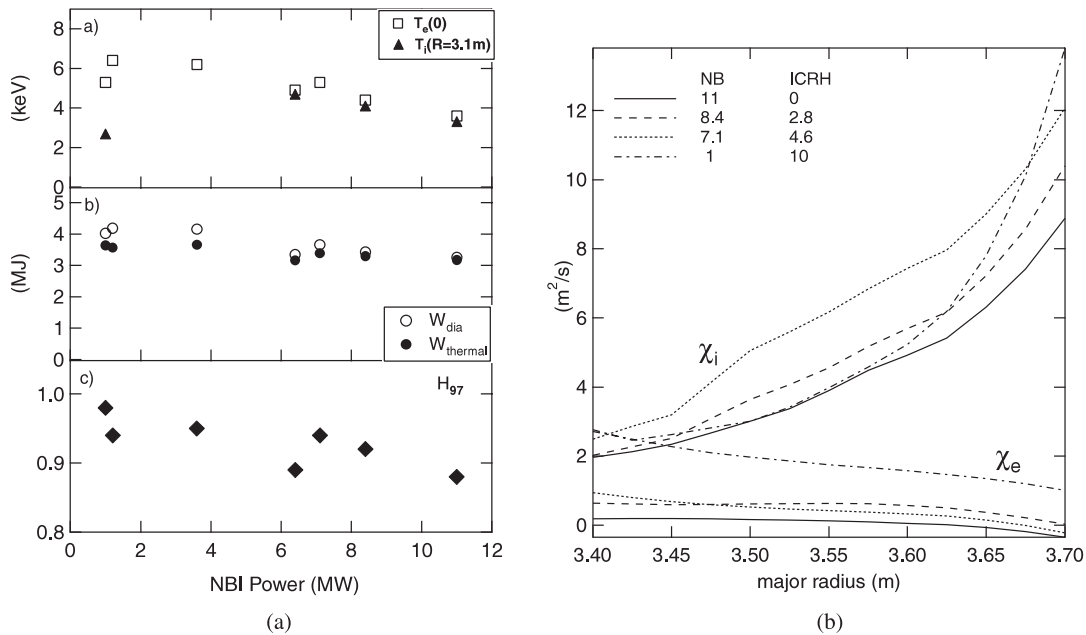

Fig. 10. Overview of (a) confinement and (b) local ion (electron) thermal diffusivities $\chi_{i(e)}$ for discharges with varying fractions of ICRH and NBI power. The data are taken at $t \approx 23$ s. (From Ref. 80.)

toroidal flux ≈ 0.6, from 1.0 to 2.1. Results indicate that confinement time is not greatly affected by the ratio of electron to ion temperature.

II.F. Dimensionless Parameter Scaling Studies

Assuming that confinement is dominated by the physics of fully ionized plasmas, the normalized confinement time can be expressed in terms of dimensionless parameters that reduce the number of degrees of freedom of the problem by one.[83] The commonly chosen parameters are the normalized Larmor radius $\rho^* \propto T^{1/2}/(aB)$, $\beta \propto nT/B^2$, and the normalized collisionality $\nu^* \propto an/T^2$. These parameters are defined locally, but it is also possible to construct global definitions.[84] Unless otherwise stated, these global definitions will be used for the values and scaling quoted in this subsection. The choice of ρ^*, β, and ν^* can be shown to be useful for separating various classes of physics models of plasma confinement.[85] Dimensionless studies thus provide a method for relating experimental results to physics models. JET is of particular interest in this respect because its plasmas lie closest to those of ITER in dimensionless parameter space. As can be seen from Fig. 11, JET values of the dimensionless parameters are typically in the range $\rho^* \approx 0.003$ to 0.005, $\beta_N \approx 1$ to 2, and $\nu^* \approx 0.1$ to 1, compared with ITER baseline parameters of $\rho^* \approx 0.0019$, $\beta_N \approx 1.8$, and $\nu^* \approx 0.026$. Figure 11 also shows that a greater emphasis on high-density, high-β_N discharges in 2000 and 2001 resulted in increased coverage of the high-ν^*, high-β_N region of normalized parameter space.

II.F.1. Identity

Identity experiments attempt to match all dimensionless parameters between two machines of different size.[86] JET's large size, in relation to other machines, makes it an important part of such experiments. Engineering parameters must be varied as $B \propto a^{-5/4}$, $I \propto a^{-1/4}$, $n \propto a^{-2}$, and $T \propto a^{-1/2}$. If this is done, the normalized confinement time $B\tau_E$ should be identical. The condition that normalized confinement is unaffected by this transform is known as the Kadomtsev constraint.

A collaboration between JET and DIII-D produced matched dimensionless parameter discharges between the two machines.[87,88] The discharges had matched geometry and safety factor, $q_{95} = 3.6$. The JET discharge had $a = 0.97$ cm, $B = 1.05$ T, $\overline{n}_e = 2.1 \times 10^{19}$ m^{-3}, and stored energy of 0.88 MJ. The DIII-D discharge had $a = 0.56$ cm, $B = 2.1$ T, $\overline{n}_e = 6.4 \times 10^{19}$ m^{-3}, and stored energy of 0.68 MJ. ρ^*, β, and ν^* were all matched to within 10%. The normalized confinements agreed to within the 10% estimated errors, with $B\tau_E = 0.27$ T for JET and $B\tau_E = 0.26$ s for DIII-D. Analysis of the local transport showed that the normalized thermal diffusivities were also in good agreement across the region of evaluation, square root–normalized toroidal flux from 0.30 to 0.75. These results are a clear demonstration of the identity principle.

Identity experiments have also been carried out between JET and ASDEX Upgrade,[89] and JET and Alcator C-Mod.[90] Matches of ρ^*, β, and ν^* for the resulting discharges were less good, but the results remained consistent with the Kadomtsev constraint.
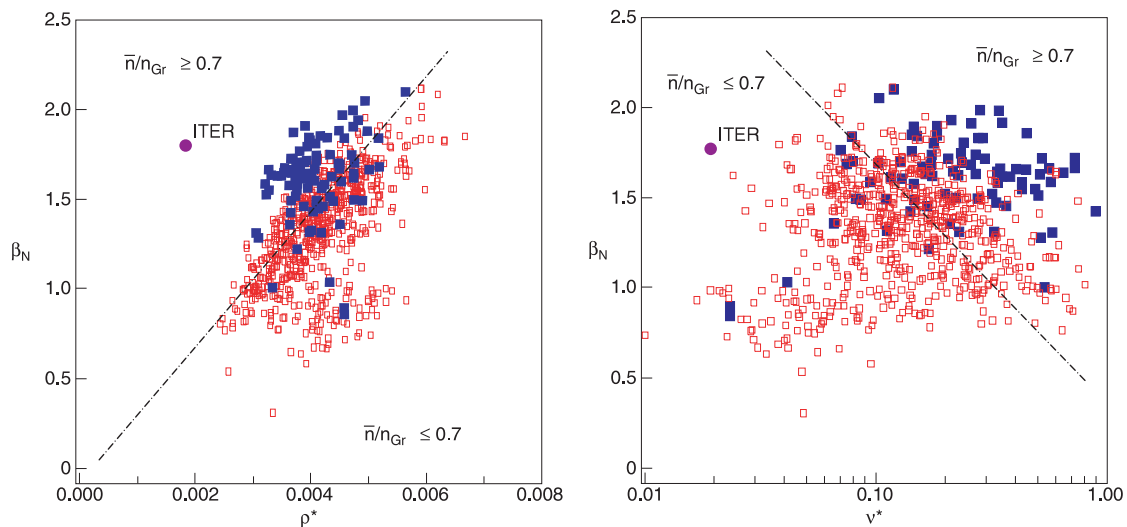
Fig. 11.   Dimensionless phase space covered by JET ELMy H-mode discharges 1994 through 2001 with 1.8 MA $< I_p <$ 2.7 MA. The parameters shown are the global ρ^*, β, and ν^* (Ref. 84). Data are taken from the JET Steady State Database.[15] Open symbols correspond to data obtained before 2000, solid symbols to those obtained since. The dashed-dotted line roughly divides the diagram in a region below and above $\overline{n}_e/n_{\mathrm{Gr}} = 0.7$, where $\overline{n}_e$ is the line average electron density and n_{Gr} is the Greenwald density limit. The ITER baseline design point is indicated by a closed circle. (From Ref. 17.)

More recently, this issue has been revisited. This follows from the observed decrease in normalized confinement with increasing density seen in JET gas-fueled discharges,[12,16,18] which can be interpreted as a possible dependence of confinement on the proximity to the Greenwald density limit.[15] This is equivalent to a dependence of normalized confinement on the Greenwald fraction, $f_{Gr} = \overline{n_e}/n_{Gr}$. Because the Greenwald density limit is inconsistent with models based only on the physics of fully ionized plasmas, such a dependency would violate the Kadomtsev constraint. To test this, JET performed two experiments, the first with DIII-D (Ref. 91), the second with Alcator C-Mod.[92] In both experiments, a pair of discharges matching ρ^*, β, and ν^* and a pair of discharges matching ρ^*, β, and f_{Gr} were produced. If proximity to the Greenwald density limit were the dominant effect in gas-fueled density scans, the ρ^*, β, and f_{Gr} matches would be expected to have a closer match for the normalized confinement times than the ρ^*, β, and ν^* matches. The JET/C-Mod experiment represented the largest range in plasma size, and hence gave the clearest results. JET plasmas were produced in a similar shape, $\kappa \approx 1.67$ and $\delta \approx 0.40$ to 0.48, with a similar safety factor $q_{95} = 4.3$. Figure 12a shows the normalized confinement for the matched ρ^* and β discharges plotted against ν^*. The JET discharge that matches the ν^* of the Alcator C-Mod discharge also matches its normalized confinement within the estimated error. Figure 12b shows the normalized confinement for the matched ρ^* and β discharges plotted against f_{Gr}. The JET discharge that matches the f_{Gr} of the Alcator C-Mod discharge clearly has a normalized confinement that is significantly higher (with regard to the estimated errors). The local transport was also found to reflect this behavior. The JET/DIII-D comparison also showed similar behavior, but the smaller range in sizes meant that the results were less clear. Taken together, these results support the applicability of the Kadomtsev constraint and show that, for the parameter range explored, proximity to the Greenwald density limit does not impact on confinement.

In addition to the identity experiments, a related experiment has been carried out between JET and JT-60U (Ref. 93). The design of these devices means that it is not possible to match the aspect ratio. In the experiments, the JET aspect ratio was 16% below that of JT-60U, but other shape parameters were well matched, $\kappa \approx 1.45$ to 1.48 and $\delta \approx 0.27$ to 0.28. The aim was to produce dimensionless parameters for the pedestal that, with the exception of aspect ratio, were otherwise well matched. However, despite an extensive scan of heating and fueling, it was not possible to match the dimensionless parameters ρ^*, β, and ν^*, at the pedestal, between the two machines. This is an interesting result in itself, as it implies that the pedestal characteristics are strongly affected by either the aspect ratio or another unmatched parameter, such as toroidal rotation or toroidal field ripple. Subsequent JET studies have found that confinement decreases with increasing toroidal field ripple, although it is unclear whether this is due to the change in toroidal ripple itself or the associated change in toroidal rotation.[94,95] Either of these effects would be consistent with the results of the JET and JT-60U identity experiments discussed here.

II.F.2. Normalized Larmor Radius

The dependence of confinement on normalized Larmor radius ρ^* distinguishes between Bohm-like, $B\tau_E \propto \rho^{*-2}$, and gyro-Bohm-like, $B\tau_E \propto \rho^{*-3}$, transport models. ρ^* is the only dimensionless parameter whose ITER value cannot be matched on present-day machines. Thus, ρ^* studies are important for determining the underlying physics models, and studies on JET, the machine with the closest ρ^* to ITER, are of particular relevance. These studies have taken the form of ρ^* scans, in which β and ν^* are fixed and ρ^* is varied to determine its scaling. To
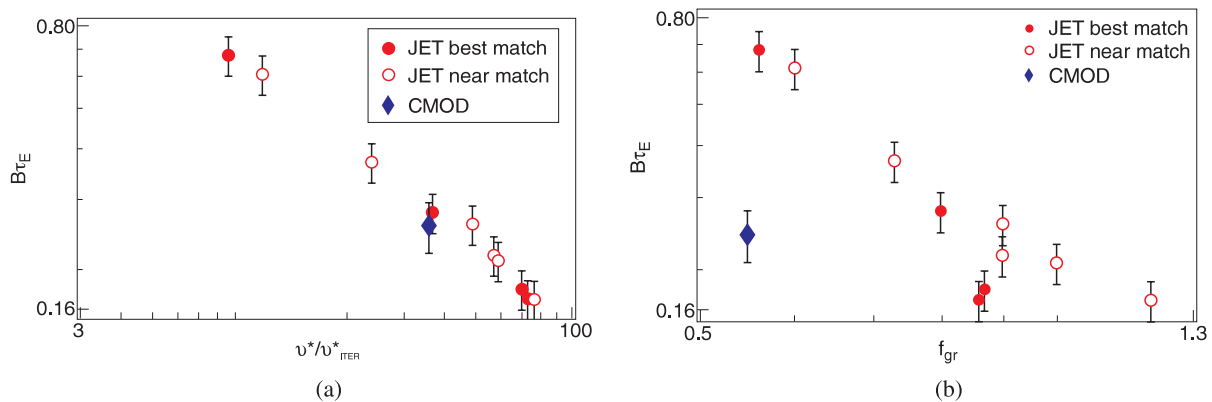

Fig. 12. Normalized energy confinement time versus ν^* calculated at (a) the $x = 0.6$ and (b) Greenwald fraction for a C-Mod discharge and JET discharges that match the C-Mod discharge with respect to ρ^*, β, q profile, and shape. Here, x is the square root–normalized poloidal flux. (From Ref. 92.)

achieve this, engineering parameters must be varied as $I \propto B$, $n \propto B^{4/3}$, and $T \propto B^{2/3}$.

Following the first ELMy H-mode ρ^* studies, on DIII-D (Ref. 96), JET performed a similar study with the MkII divertor.[97] Three type I ELMy H-mode ρ^* scans were performed, with a different set of β and ν^* for each scan. The β values chosen corresponded to $\beta_N = 1.5$, 1.6, and 2.0. The field range for the largest scan was 1 to 2.6 T. All three scans were consistent with a gyro-Bohm-like $B\tau_E \propto \rho^{*-2.7}$ scaling. This result is consistent with the DIII-D studies, which found a somewhat stronger $B\tau_E \propto \rho^{*-3.1}$, but still essentially gyro-Bohm-like, dependency. These results are shown in Fig. 13, where the normalized confinement times from the JET and DIII-D ρ^* scans, together with those from the identity discharges, have been plotted against that predicted by the ITERH93-P scaling.[98] This scaling was derived empirically from a multimachine ELMy H-mode database and has a ρ^* scaling of $B\tau_E \propto \rho^{*-2.7}$. It can be seen that all three JET ρ^* scans, and the DIII-D ρ^* scan, lie parallel to the ITERH93-P scaling. The JET and DIII-D experiments were coordinated so that similar ν^* were used in the $\beta_N = 2.0$ scan.[97] This enables them to be combined into a multimachine ρ^* scan, with considerably extended range, which extrapolates to essentially the same value for the ITER baseline operating point as would be given by the ITERH93-P scaling. These experiments have thus provided an essentially independent prediction of ITER confinement, using a single parameter extrapolation in ρ^*. It should be noted, however, that the parameters taken were for the pre-1999 ITER Final Design Report, so a similar study remains to be performed for the current design.[3] However, the consistency of this method with the scaling derived empirically from a multimachine database means that this method would be, once again, expected to support the prediction from these scalings.

A JET study in type III ELMs, performed, with the MkIIGB divertor, also found close to gyro-Bohm-like confinement, $B\tau_E \propto \rho^{*-2.9\pm0.5}$ (Ref. 99). At the same time, a type I ρ^* scan was also performed. This had a wider field range than the previous scans, 1.2 to 3.1 T, but the NBI heating profile was found to vary sufficiently to affect the global confinement. Despite this, the local confinement properties could be studied, and the normalized thermal diffusivity χ/B was found to be consistent with a gyro-Bohm-like scaling, $\chi/B \propto \rho^{*3.2\pm0.4}$.

Taken together, all the JET results support a gyro-Bohm-like scaling for plasma confinement in both the type I and type III ELMy H-mode regimes. In conjunction with the DIII-D results, the results reinforce the empirical multimachine scaling estimates of the ITER baseline operating point.

II.F.3. Normalized Plasma Pressure

The dependence of confinement on normalized plasma pressure β essentially distinguishes between electrostatic transport models, which are largely β independent, and electromagnetic transport models, which are strongly β dependent.[100] Since the fusion product, on a given machine at a given field, scales as $Q \propto \beta\tau_E$, knowledge of the β scaling is also important for determining the optimal operating point on ITER. JET studies of the β scaling have taken the form of β scans, in which ρ^* and ν^* are fixed and β is varied to determine its scaling. To achieve this, engineering parameters must be varied as $I \propto B$, $n \propto B^4$, and $T \propto B^2$.

Two separate β scaling studies have been performed on JET (Refs. 19 and 101). The most extensive of these studies was performed with the MkIIGB divertor and involved three ELMy H-mode β scans.[19] One of these scans was performed in a low-shape configuration, $\kappa \approx 1.6$ and $\delta \approx 0.2$, with a safety factor of $q_{95} \approx 3.2$. This covered a range of field of $B \approx 1.5$ to 1.9 T, with a resulting β scan of $\beta_N \approx 0.7$ to 2.0. The normalized confinement was found to be almost unchanged across the scan, consistent with a $B\tau_E \propto \beta^{-0.01\pm0.11}$ scaling. This almost negligible β dependence is in line with the other two scans in this study (Fig. 14). Similar results were found in the other JET study. These results contradict the decreasing confinement with increasing β seen in the empirically derived multimachine scalings.

A negligible dependence of confinement on β was also seen in experiments on DIII-D (Refs. 100 and 102). However, experiments on JT-60U (Ref. 103) and Asdex
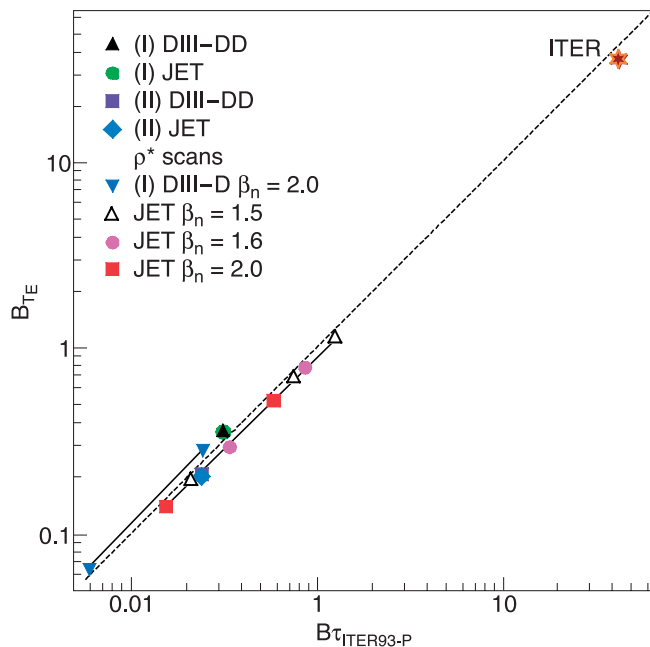

Fig. 13. Normalized energy confinement time $B\tau_E \propto \omega_{ci}\tau_E$ plotted against the empirically derived scaling law ITERH93DP. The discharges shown are from dedicated ρ^* scans, in ITER-like conditions, performed on DIII-D and JET. (From Ref. 13.)
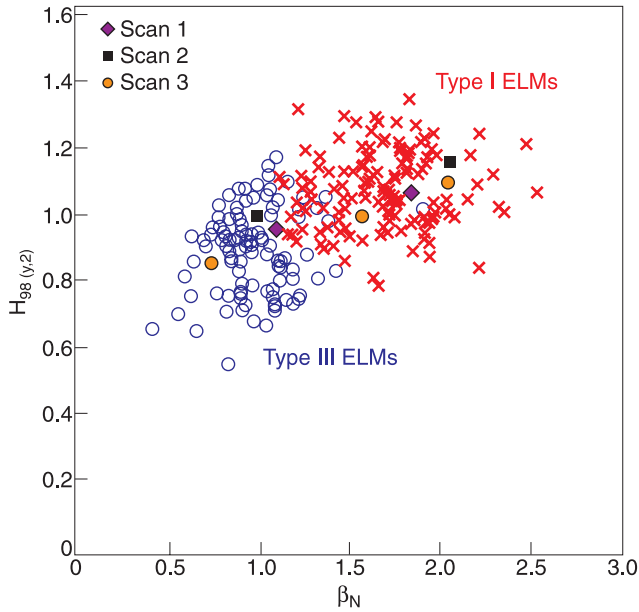
Fig. 14. Consistency of the energy confinement with the IPB98(y,2) scaling. $H_{\text{IPB98(y,2)}} = \tau_E/\tau_{\text{IPB98(y,2)}}$. Data are taken from gas-fueled, ICRH- and NBI-heated, JET stationary ELMy H-modes from 1994 through 2001 (crosses for type I ELMy H-modes, open circles for type III ELMy H-modes) with three dedicated β scans overlaid. Each scan is represented by a different symbol (closed diamonds, squares, or circles) and has different values of ρ^* and ν^*, for a range of β. (From Ref. 19.)

Upgrade[104] results show a decrease in plasma confinement with increasing β.

For ITER, the β-independent scaling observed on JET would imply a $Q \propto \beta\tau_E$ scaling for the fusion product. This would enable improved confinement fusion performance at high β (Ref. 105).

II.F.4. Normalized Collisionality

The impact of normalized collisionality ν^* on energy confinement involves several competing processes. Thus, unlike ρ^* and β, collisionality does not neatly separate classes of transport models. Nevertheless, the ν^* scaling does distinguish between individual transport models. For this reason the ν^* confinement scaling has been studied on JET. The studies have taken the form of ν^* scans, in which ρ^* and β are fixed and ν^* is varied to determine its scaling. To achieve this, engineering parameters must be varied as $I \propto B$, $n \propto B^0$, and $T \propto B^2$.

Two scans have been performed.[97,99] The most extensive scan was a four-point scan with the MkIIGB divertor.[99] This scan was in a high-shape, $\kappa \approx 1.67$ and $\delta \approx 0.4$, configuration with a safety factor of $q_{95} \approx 4.4$. The field was varied from 0.96 to 1.6 T, resulting in a ν^* range of a factor of 9.4. Confinement was found to de-

crease with increasing collisionality as $\beta\tau_E \propto \nu^{*-0.35\pm0.04}$. This is consistent with the other scan, performed with the MkII divertor, which found $\beta\tau_E \propto \nu^{*-0.27}$. Both of these scalings are stronger than the negligible collisionality scaling, $\beta\tau_{E,98(y,2)} \propto \nu^{*-0.01}$, given by IPB98(y,2). Dedicated collisionality scans on other machines also show decreasing confinement with increasing collisionality, although a range of scalings are observed.[92] This may result from confinement having a strongly non–power law dependency on collisionality, but further work is required to resolve this. The strong correlation between density and collisionality means that there is a close relation between the differences in

1. the observed ν^* scaling on JET and that seen in IPB98(y,2) discussed here

2. the observed density scaling on JET and IPB98(y,2) discussed in Sec. II.D.

A scaling with an improved form for the collisionality dependence would be expected to better describe the results of JET density scans. Alternatively, a negative dependence of confinement on the gas-fueling rate could explain the discrepancy between IPB98(y,2) and the JET collisionality scans discussed here. However, such a dependency would appear to contradict the results of the identity experiments discussed in Sec. II.F.1.

II.F.5. Isotope

If the hydrogen isotope is permitted to vary, an additional dimensionless parameter is introduced. This is most conveniently taken as the atomic mass of the hydrogenic species, M. For an M scan, ρ^*, β, and ν^* are matched between plasmas with different hydrogenic species. To achieve this, engineering parameters must be varied as $B \propto M^{3/4}$, $I \propto M^{3/4}$, $n \propto M$, and $T \propto M^{1/2}$.

JET has performed the only such experiment, with the MkII divertor.[106] A hydrogen discharge was run at 1 MA and 1 T with a plasma stored energy of 0.82 MJ. This was matched to a deuterium discharge at 1.7 MA and 1.7 T with a plasma stored energy of 2.42 MJ. The normalized confinement times were $B\tau_E/M \approx 0.29$ Ts for the hydrogen discharge and $B\tau_E/M \approx 0.32$ Ts for the deuterium discharge. This indicates a negligible ion mass dependency. The normalized thermal diffusivities $M\chi/B$ for this pair are shown in Fig. 15. The hydrogen and deuterium profiles are seen to agree within the estimated errors of the measurements. This is consistent with the global confinement measurements.

Thus, the global confinement appears to be independent of the dimensionless parameter M. This is in contrast to the positive isotope mass scaling seen in the IPB98(y,2) scaling, $B\tau_{E,98(y,2)}/M \propto M^{0.96}$. It should be noted that although the JET isotope experiments found a mass scaling similar to that of IPB98(y,2) when engineering parameters were fixed, there was insufficient spread in the other engineering parameters to produce a
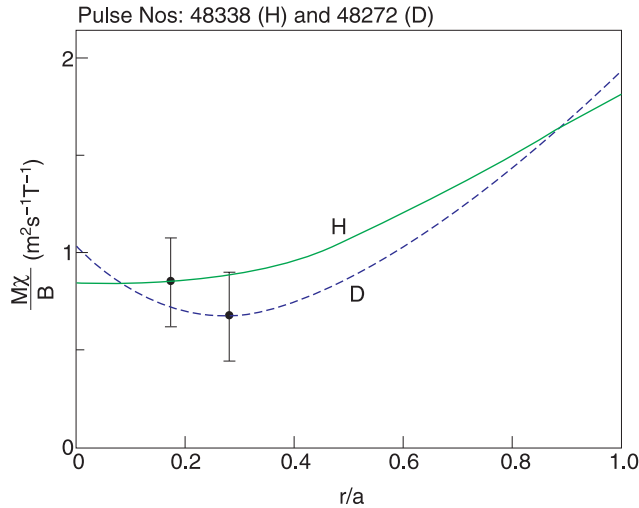
Pulse Nos: 48338 (H) and 48272 (D)

Fig. 15. The normalized effective conductivity versus the radial coordinate for a hydrogen H (solid line) and a deuterium (dashed line) discharge with matched ρ^*, β, and ν^*. (From Ref. 106.)

scaling law from the JET studies alone that could be converted to dimensionless parameters. As a result, it is not possible to say whether the weak mass dependence observed in dimensionless parameter space for the experiments of this subsection is consistent or inconsistent with the $\tau_E \propto M^{0.20}$ scaling observed in the experiments of Sec. II.C. The same applies to the consistency between the results discussed in this section and the pedestal pressure scaling results discussed in Secs. II.C and IV.B.

II.G. Conclusions

Early JET experiments found that ohmic and L-mode plasma confinement on JET is broadly consistent with established multimachine scalings, motivating the development and study of ELMy H-mode regime. The transition from L-mode to H-mode has been observed to involve an abrupt improvement in confinement across most of the plasma, leading to stationary ELMy H-modes with approximately double the confinement of an equivalent L-mode.

ELMy H-mode confinement has been seen to improve with increasing triangularity, through its impact on pedestal behavior. Ion species studies have shown that confinement improves with mass, for hydrogenic plasmas. Importantly for ITER, this has been shown to apply to tritium and mixed deuterium-tritium plasmas. Helium plasmas have been observed to have confinement times below those of hydrogen plasmas. A modest improvement in normalized confinement has been observed with the move to more closed divertor designs. Elongation has been shown to improve confinement. ICRH and NBI-heated plasmas have been shown to have similar confine-

ment properties, with ICRH plasmas having slightly better performance. Dimensionless parameter experiments and analyses have found an electrostatic, gyro-Bohm-like scaling of confinement and local transport, supporting drift wave models of turbulence.

Taken as a whole, these results have strongly influenced the choice of the ELMy H-mode in a high-triangularity, high-current, high-density plasma as the baseline scenario for ITER. They have also increased confidence in ITER reaching its baseline performance goals and offer routes to exceeding them.

III. L-H TRANSITION STUDIES

The transition from L- to H-mode is characterized by a reduction in transport near the edge of the confined plasma and the formation of steep gradients in electron and ion temperature and density. This ETB, often referred to as the H-mode pedestal, is typically a few centimeters wide on JET, and its formation at the L-H transition is associated with a threshold power P_{th}. Since the ELMy H-mode is the reference operating scenario on the next-step fusion device, ITER, there has been considerable effort to characterize and improve the understanding of the behavior of H-mode access on JET. JET has contributed strongly to the physics basis of the L-H transition used in the design of ITER, including contributing to the development of multimachine scalings for P_{th} (Refs. 13 and 107). Therefore, experiments have been performed over a wide range of operating conditions. Highlights from the recent work on JET in this area are reviewed here.

III.A. H-Mode Access at Low Density

In all tokamaks the threshold power for H-mode access, P_{th}, is observed to increase approximately linearly with electron density n_e. However, a minimum P_{th} as a function of n_e has been demonstrated on several machines, including COMPASS-D (Refs. 108 and 109), JT-60U (Ref. 110), Alcator C-Mod,[111] and DIII-D (Ref. 112). Furthermore, it has been noted that there had been insufficient documentation of P_{th} toward low density to make a prediction for ITER (Ref. 113). For example, questions remain as to how the minimum P_{th} at low-density threshold varies with magnetic field B_T or plasma current I_p (Ref. 113).

The departure of P_{th} on JET from the ITER n_e scaling at very low plasma densities has been widely observed at JET (Refs. 114 through 117). Low-density H-mode threshold data from COMPASS-D, JT-60U, and JET have also been compared with an Alfvén drift instability theory.[118]

In Ref. 117 a series of density scans were performed on JET with the MkIIGB septum divertor shown in Fig. 16a at I_p/B_T values of 2.5 MA/2.7 T, 2.5 MA/2.6 T, 2.5 MA/2.4 T, and 2.2 MA/2.4 T. The values of P_{th} and
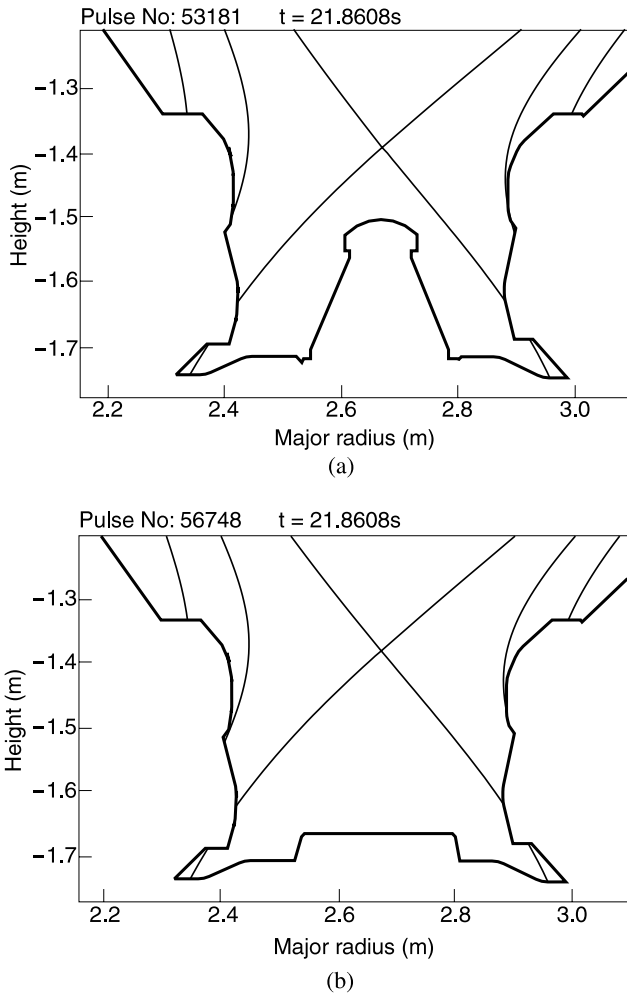
Fig. 16. JET's (a) MkIIGB septum divertor and (b) MkIIGB
         SRP divertor. (From Ref. 117.)

pedestal electron temperature at the L-H transition, T_e^{ped},
are shown in Figs. 17a and 17b as a function of edge
electron density n_e^{ped} (Ref. 117). All the data show a clear
minimum in P_{th} and T_e^{ped}, with their highest values at the
lowest values of n_e. The electron density scans at 2.5
MA/2.7 T and 2.5 MA/2.6 T were later repeated with
the MkIIGB septum replacement plate (SRP) divertor,
shown in Fig. 16b (Ref. 117). Results from this scan are
shown in Figs. 18a and 18b for P_{th} and T_e^{ped}, respectively.
Despite lowering the n_e to values very similar to those of
the original scan, no evidence of departure from the lin-
ear scaling with n_e was observed. Comparisons of the
pedestal T_e show this local, edge parameter to be rela-
tively insensitive to the removal of the divertor septum.

    The effect of convective heat losses on the H-mode
P_{th} on JET under low-density conditions has been re-
cently considered using the one-dimensional (1-D) trans-
port code RITM (Ref. 119) to calculate contributions to
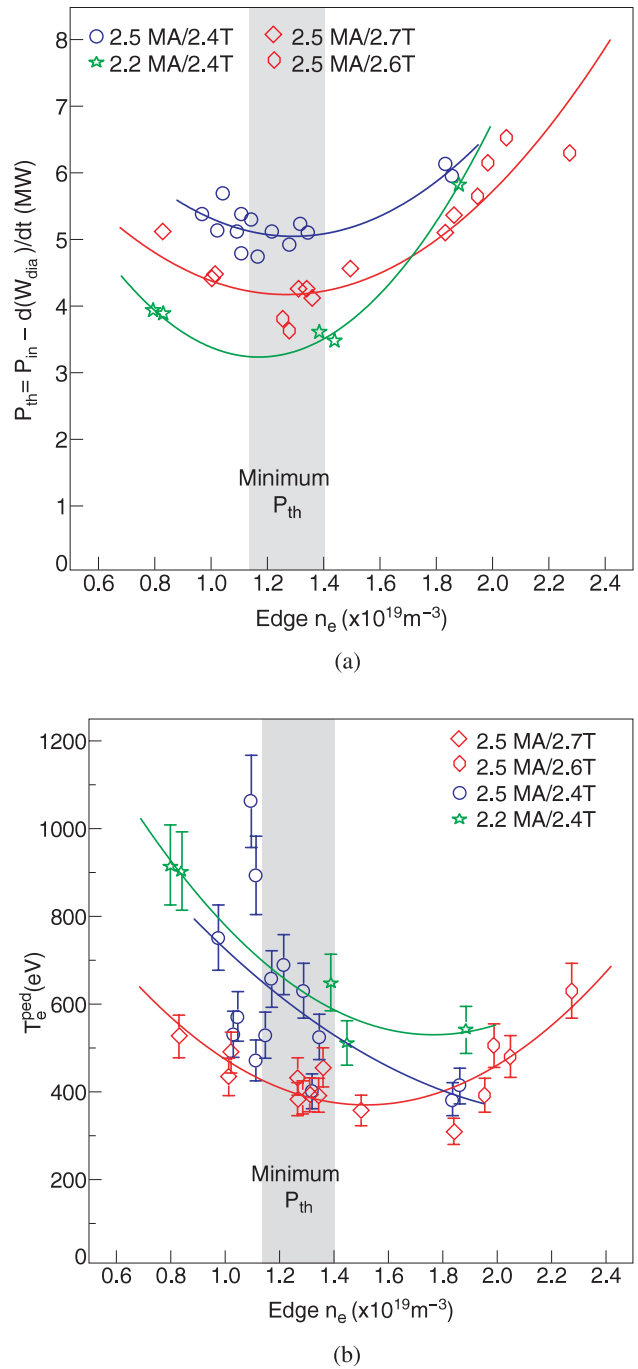
Fig. 17. (a) Power threshold P_{th} and (b) pedestal electron tem-
         perature T_e^{ped} at the L-H transition plotted as a func-
         tion of edge n_e for the MkIIGB septum divertor density
         scans. The solid lines represent fits to the data. (From
         Ref. 117.)

the local thermal transport.[120] It was found that when the
fraction of modeled convective heat losses does not ex-
ceed 50%, the calculated P_{th} agrees well with multi-
machine scalings. On the other hand, increases in the

(a)

(b)

Fig. 18. (a) P_{th} and (b) T_e^{ped} for the MkIIGB septum and SRP divertors plotted as a function of edge n_e. The solid lines represent fits to the data. (From Ref. 117.)

III.B. Effect of the Divertor Geometry on the L-H Transition

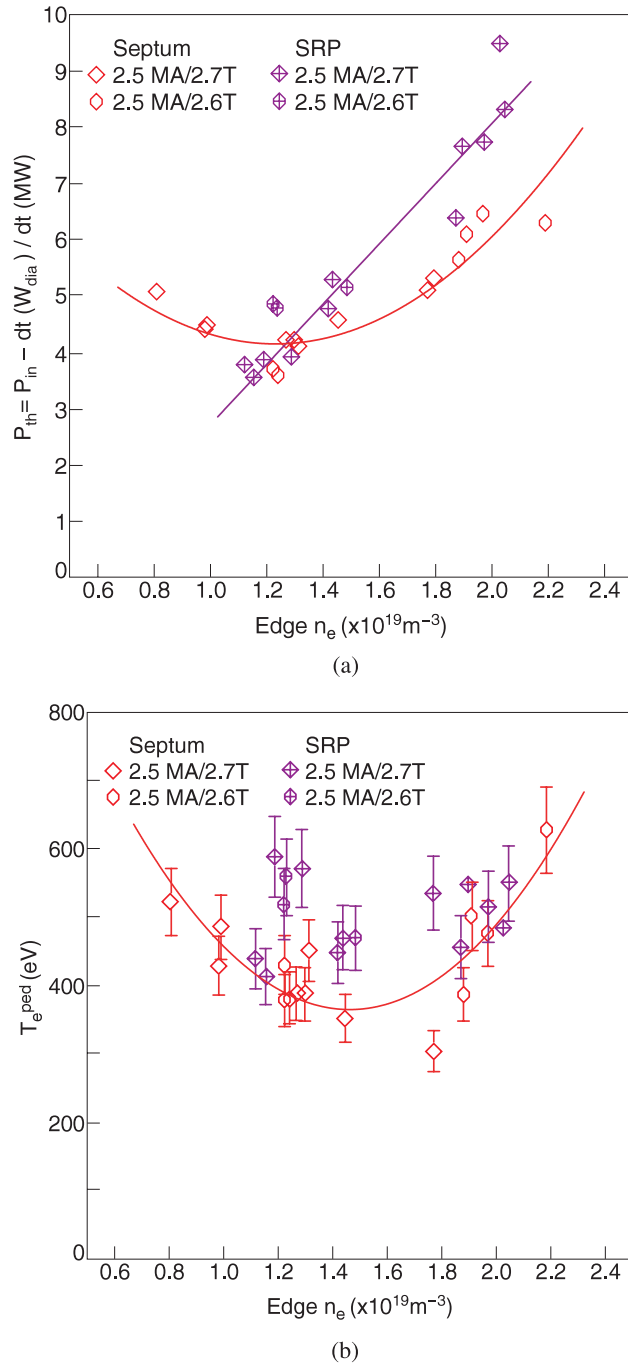One of the major results from JET operation with the MkIIAP divertor was the demonstration of the strong influence of the divertor configuration on the L-H transition P_{th} (Ref. 114) when it was reported that P_{th} was higher with the strike points on the vertical targets than with them on the horizontal target plates. The accompanying pedestal electron temperature T_e^{ped} was also found to be higher with the strike points on the vertical target plates. With the installation of the MkIIGB divertor, operation with the strike points on the horizontal target plates was no longer possible, due to the presence of the septum. However, plasma operation with an X-point height scan onto the septum, as shown in Fig. 19 demonstrated a very significant effect on P_{th}. The power required to access the H-mode was lowered by almost a factor of 2 when the X-point was lowered onto the divertor septum as shown in Fig. 20, with a corresponding drop in T_e^{ped}. This result was taken to indicate that in addition to the pedestal T_e^{ped}, some other parameter must control the access to the H-mode under such conditions.[121] This study also found the decrease in P_{th} and T_e^{ped} to correlate well with increasing divertor neutral density with lowered X-point height.[122] The P_{th} and T_e^{ped} appear to be sensitive to increased vertical proximity between the region of recycling and the X-point. A similar effect was considered on JFT-2M in Ref. 123 to explain the experimental observation of H-mode triggering on the injection of neutrals through gas puffing at the X-point. Following the initial experiment in deuterium plasmas, a similar X-point height scan was repeated with helium plasmas, as reported in Ref. 67. The trend of decreasing P_{th} with decreasing X-point height was reproduced with the helium plasmas, also shown in Fig. 20. These results support
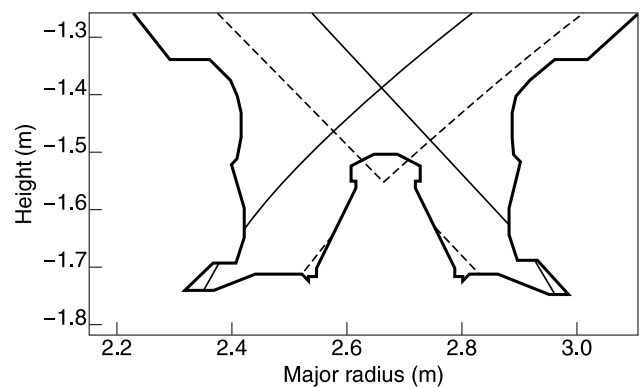
Fig. 19. JET MkIIGB divertor region for the range of configuration used in the P_{th} X-point height scan. The height of the X-point was varied from 13 cm above the septum (solid line) to 5 cm below the septum (dashed line). (From Ref. 67.)

heat losses due to modeled convected heat losses led to values of P_{th} several times higher than that of the multimachine scaling. These conditions have been compared with low-density JET discharges, for which this model would expect increased levels of heating power to establish the ETB (Ref. 120).

Fig. 20. Impact of the X-point height on the L-H power threshold for NBI-heated deuterium (circles) and helium (diamonds) JET MkIIGB divertor plasmas. The L-H threshold power is normalized to the scaling given in Eq. (1) of Ref. 67. (From Ref. 67.)

Fig. 21. Power threshold for the L-H transition normalized to the scaled power threshold from Ref. 107 plotted against distance from the septum top. (From Ref. 122.)

L-H transition models that involve neutral penetration, although such models would also need to explain why the helium and deuterium plasmas demonstrate similar trends in P_{th} dependence when their ionization properties differ.

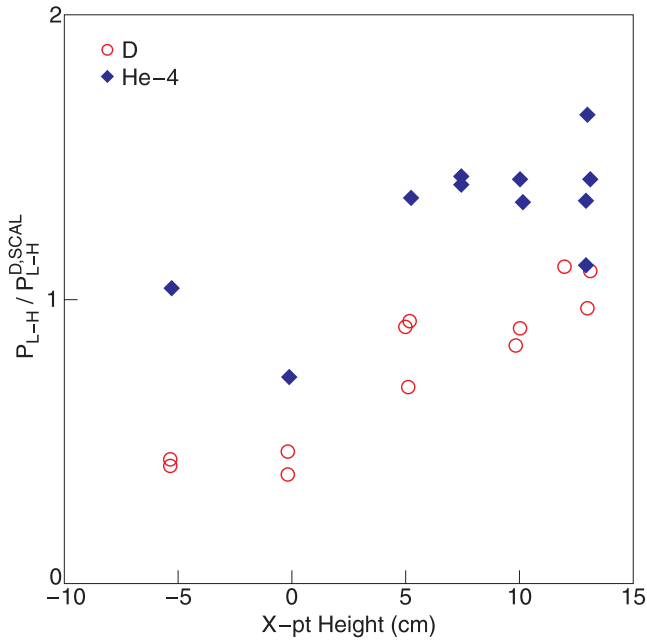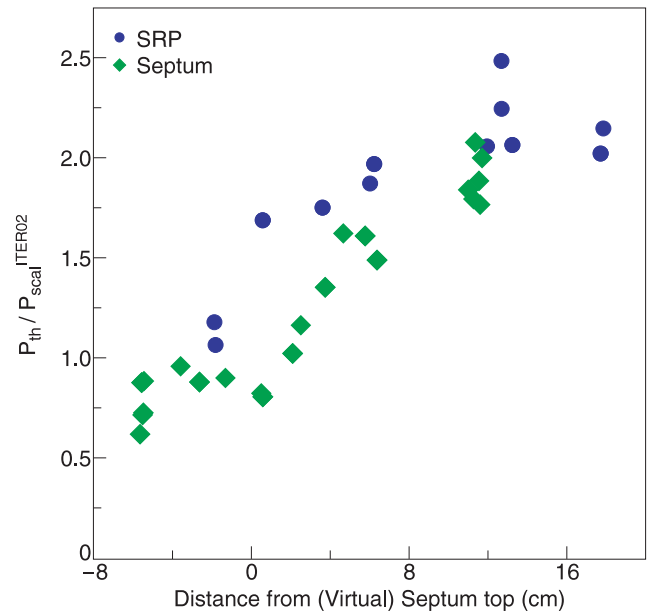The substitution of the divertor septum with the SRP during 2003 meant that the inner and outer divertor legs were no longer separated as shown in Fig. 16b. A new set of experiments was run to isolate the influence of the divertor septum on the L-H transition under otherwise similar conditions.[122] The reduction in P_{th} with decreasing X-point height observed with the MkIIGB septum divertor was reproduced with the SRP, as shown in Fig. 21. For comparison purposes, measurements of X-point height were taken relative to the septum top for the MkIIGB experiments and relative to where the septum top would have been (virtual septum top) for the experiments with the SRP. While the strike points remained on the vertical targets with an X-point height range of 17 to 6 cm above the (virtual) septum top, no clear variation in P_{th} was measured. However, once the strike points moved onto the horizontal targets and the X-point height was decreased from 6 cm above to 6 cm below the (virtual) septum top, the power threshold for H-mode access decreased by a factor of 2. In addition, there was found to be no difference in T_e^{ped} between the two divertors. Both sets of data had a corresponding decrease in T_e^{ped} with decreasing X-point height. With decreasing X-point height below 6 cm above

the (virtual) septum top, the strike points and both the inner and outer SOL move inward along the horizontal targets. P_{th} was therefore considered to be sensitive to the increased vertical proximity between the region of recycling (top of septum or horizontal target plates) and the X-point. It should be noted that for the MkIIGB discharges only, the septum acted as a limiter once the X-point height above the septum top approached zero.

III.C. Plasma Shape Effects on the L-H Transition

The influence of increased upper triangularity δ_{upper} was investigated by fixing the lower triangularity and varying δ_{upper} from 0.21 to 0.38 across the same n_e range at I_p/B_T of 2.5 MA/2.7 T, presented in Ref. 122. Variation of δ_{upper} was found to have no effect on P_{th} or the pedestal T_e or T_i (measured in the L-mode phase as close as possible in time to the L-H transition) across the n_e range scanned, Fig. 22a.

The role of δ_{lower} on H-mode access was also examined with the MkIISRP divertor using two magnetic configurations with $\delta_{upper}/\delta_{lower}$ of 0.23/0.23 and 0.43/0.33 at I_p/B_T of 2.5 MA/2.7 T. To accommodate the increase in δ_{lower}, the X-point was lowered and the outer divertor strike point was shifted from the vertical to the horizontal target. A density scan with the two configurations demonstrated P_{th} to be very similar at the lowest densities, whereas for values of edge n_e above 1.8×10^{19} m^{-3}, the increased plasma shaping reduced P_{th} by up to 25%. The pedestal top T_i was the same for the two configurations, whereas pedestal T_e was lower for the configuration with
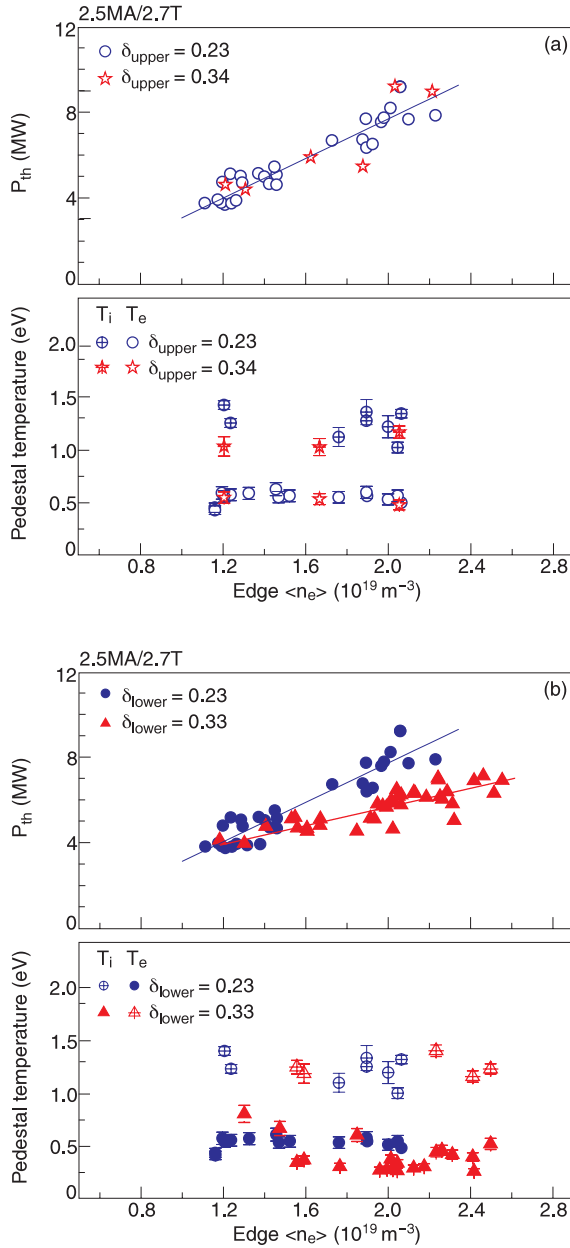
Fig. 22. Comparison of the L-H transition P_{th} and pedestal T_i and T_e values for plasmas with $\delta_{upper}/\delta_{lower}$ of (a) 0.23/0.23 and 0.34/0.23 and (b) 0.23/0.23 and 0.43/0.33. (From Ref. 122.)

Fig. 23. Measured P_{th} for both forward and reversed field plotted as a function of scaling for P_{th} taken from Ref. 107. (From Ref. 124.)

III.D. Reversed B_T Dependence

The effect of reversed B_T direction on the L-H transition has also been studied on JET with the MkIISRP divertor and results are reported in Ref. 124. Reference forward field plasmas (forward B_T) with coinjected NBI and ion ∇B drift toward the X-point were repeated as reversed B_T shots, with ion ∇B drift away from the X-point and counter NBI. The reverse B_T plasmas were run by reversing the direction of both B_T and I_p. Comparison of the reversed B_T discharges with forward field plasmas in Fig. 23 shows that P_{th} was found to be very similar across the n_e and B_T scans performed on JET. This is in contrast to results from DIII-D and ASDEX Upgrade, in which P_{th} was measured to be significantly higher with ion ∇B directed away from the X-point and with co-NBI in the direction of I_p (Refs. 125, 126, and 127). This result is also in contrast to results from Alcator C-Mod with ICRH-only heated plasmas.[128] Despite showing very similar P_{th} to the forward field shots, the reversed B_T values of T_e^{ped} and T_i^{ped} at the L-H transition are lower, although the approximately linear dependence on B_T was reproduced, as shown in Fig. 24.

III.E. Conclusions

JET studies have contributed strongly to the experimental basis for the L-H transition. This has led to the derivation and validation of multimachine scalings that describe the broad dependence of P_{th} on global parameters such as machine size, density, and magnetic field. However, the confidence intervals of these scalings are

increased δ_{lower}. Since δ_{upper} was found to have no influence on P_{th}, it is thought that the decrease in P_{th} with increased δ_{upper} is due to the lowering of the X-point height and the movement of the outer strike point from the vertical to the horizontal target, required to accommodate the increased magnetic shaping. These results indicate that the edge temperature required for the L-H transition is dependent on plasma geometry, which may partly explain the variation of P_{th} with geometry.
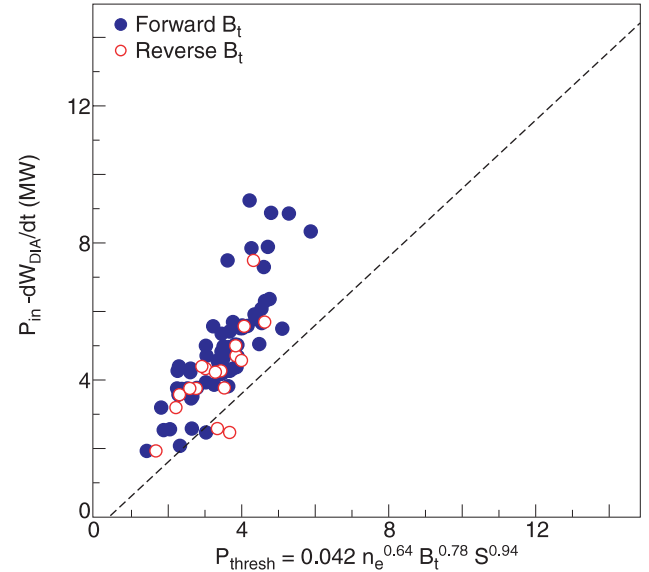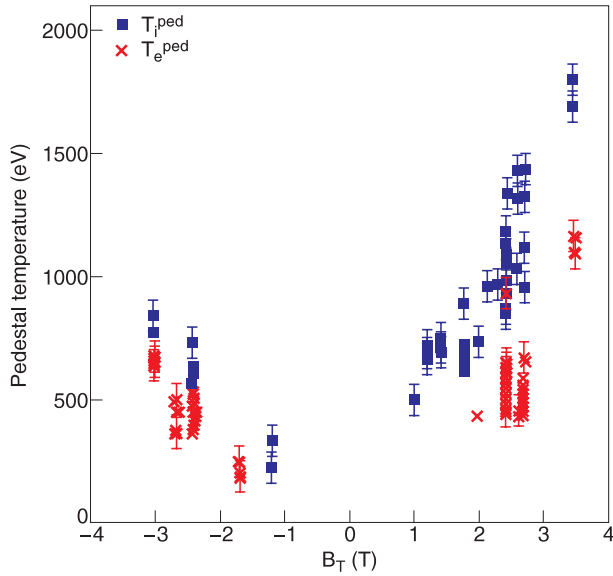
Fig. 24. Scaling of T_i^{ped} and T_e^{ped} at the L-H transition with B_T in both forward and reverse directions. The positive values of B_T correspond to ion ∇B toward the X-point, whereas negative B_T has ion ∇B directed away. (From Ref. 124.)

large, and more detailed studies of the L-H threshold are required to increase assurance in extrapolations to larger machines such as ITER. At low densities, the L-H power threshold is observed to increase with decreasing density, a potential concern for ITER. Divertor configuration is also observed to strongly affect the L-H threshold, with low X-points having been shown to be favorable for reaching the L-H threshold. The L-H power threshold in higher-triangularity plasmas, with decreased X-point height, has been found to have a density scaling different from that in equivalent lower-triangularity plasmas, with increased distance from X-point to target. The dependence of the L-H threshold on the direction of the toroidal magnetic field has also been studied. This important topic remains an area of active research on JET.

IV. PEDESTAL PHYSICS AND ELM BEHAVIOR

JET pedestal studies began with type I ELMy H-modes, which provided the first stationary, high-confinement, $H_{98(y,2)} \geq 1$, scenario on JET. Studies at high triangularity, $\delta \geq 0.4$, led to the identification of the mixed ELM, type I-II ELMy H-modes, which have confinement properties similar to those of type I ELMy H-modes but are generally able to achieve higher densities. Type III ELMy H-modes have lower confinement and pedestal pressure than type I ELMy H-modes, but their reduced ELM size has made them of interest as a

low–power load scenario. The aim of achieving both high confinement and low power load in a single scenario has led to investigation of the pure type II ELMy H-modes and grassy ELMy H-modes. The pedestal physics and ELM behavior of all of these modes are described here, but first a summary of the available diagnosis of the JET plasma edge is presented.

IV.A. Diagnosis

Pedestal diagnosis is complicated by the high resolution required to resolve the pedestal region, which has a typical radial width of <10 cm. A common method used to determine the pedestal density and ion and electron temperatures is given in Ref. 16. An electron cyclotron emission (ECE) diagnostic is used to identify the radial position of the top of the pedestal and to measure the electron temperature at the pedestal top, $T_{e,ped}$, Fig. 25. The ion temperature at the pedestal top, $T_{i,ped}$, is then measured with charge-exchange spectroscopy (CXSE) and the electron density at the pedestal top, $n_{e,ped}$, with interferometry. Because of the cutoff properties of the waves used by the JET ECE system, the edge electron temperature of plasmas with magnetic field B_T below 1.7 T cannot be measured. The electron density at the top of the pedestal is measured using the radially most outward
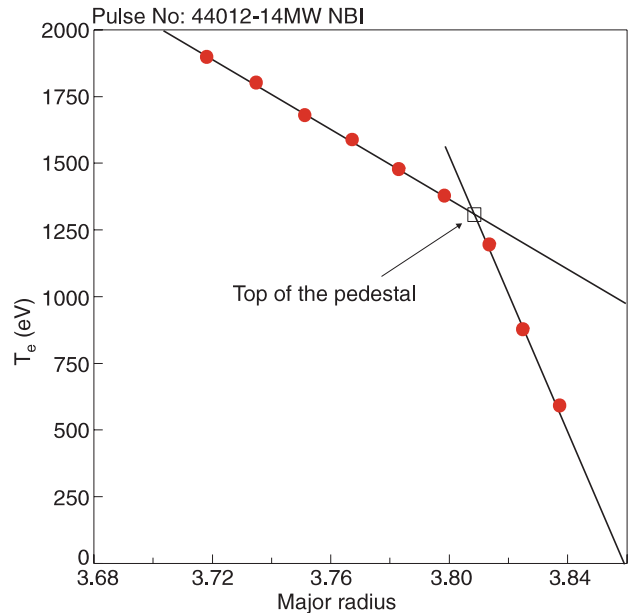

Fig. 25. Electron temperature profile measured with the ECE heterodyne radiometer. This profile was taken during the stationary phase of an ELMy H-mode (pulse 44012, 14 MW NBI), in between two type I ELMs. The circles indicate the experimental points and the square the extrapolated position of the edge pedestal. (From Ref. 16.)

vertical channel of the interferometry system, which lies just within the pedestal for most JET configurations. The line average electron density that this measures is a good approximation of the density at the pedestal top.[78]

Additional pedestal diagnostics include the edge lidar system.[129] The line of sight of the edge lidar system is poloidally angled (Fig. 26) which results in a near-tangential intersection with the edge flux surfaces. This enables the system to achieve spatial resolutions equivalent to ≈ 2 cm at the midplane. Temporal resolution is 1 Hz. Depending on the plasma and diagnostic configuration, either the pedestal top or the pedestal gradient can be measured. Through combination with ECE and interferometry, pedestal profiles of electron density and temperature have been produced[130] (Fig. 27). However, such
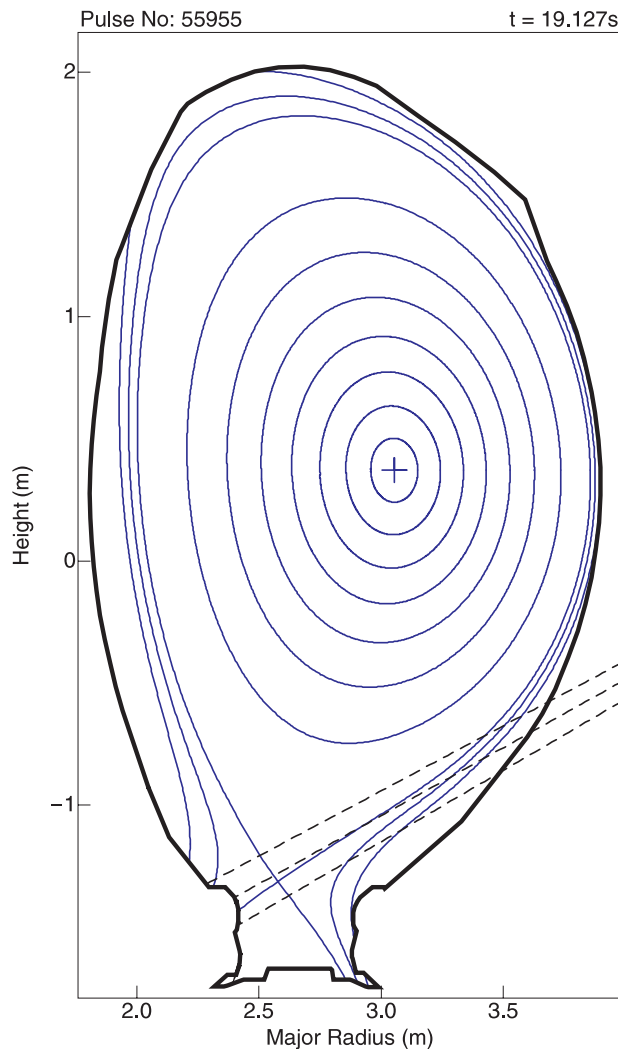

Fig. 26. Range of the edge lidar lines of sight (dashed line). The magnetic surfaces shown are those for the upper diagnostic–optimized configuration (DOC-U; Ref. 130). (From Ref. 130.)

analyses can be performed only for a limited set of plasma configurations. As a result, JET studies have been able to determine scalings only for the parameters at the pedestal top. The separation of these scalings into pedestal width and pedestal gradient effects remains to be studied. Ongoing diagnostic upgrades, including the installation of the high-resolution Thomson scattering diagnostic,[131] are expected to further improve pedestal diagnosis in this respect.

IV.B. Type I ELMy H-Modes

The main characteristics of pedestal behavior in low-triangularity, $\delta < 0.3$, type I ELMy H-modes on JET can be seen from a study of the edge operational space in MkIIA (Ref. 12; see Fig. 28). The L-H transition occurs at low edge density and temperature, and this is commonly followed by a period of high-frequency ELMs, referred to as transition ELMs, during which edge temperature and density rise. This is followed by an ELM-free period, during which edge pressure increases until a critical pressure is reached. The plasma then enters a type I ELM cycle that begins with an ELM crash at the critical pressure limit, at which edge density and temperature decrease on a time scale of ~ 0.1 ms. Edge density and temperature then increase, on a time scale of ~ 10 to 100 ms, until the critical pressure limit is reached again and the cycle repeats. As the gas fueling increases, the pedestal density prior to the ELM crash increases but the pedestal temperature decreases such that the pedestal pressure p_{ped} remains fixed or, in other studies, scales as $p_{ped} \propto n_{e,ped}^{-1}$ (Ref. 16). At sufficiently high gas fueling, a transition to a type III ELMy H-mode occurs, with a sudden decrease in the critical pedestal pressure and an increase in ELM frequency.

Studies of MkIIA, type I ELMy H-modes indicated that for fixed B_T and plasma current I_p, the critical pedestal pressure was proportional to the mean Larmor radius of either the thermal or fast ion populations.[78,79] To resolve the issue, a systematic study was performed on a series of type I ELMy H-modes produced in JET with the MkIIA divertor at 2.6 MA and 2.7 T in a single-null plasma configuration with $\delta \approx 0.23$ (Ref. 16). Gas fueling was varied and three different NBI power levels were used: 8, 11, and 14 MW. The critical pedestal pressure for type I ELMy H-modes was observed to scale almost linearly with the mean Larmor radius of the thermal population and to be uncorrelated with that of the mean Larmor radius of the fast ion population (Fig. 29). Further studies in the MkIIA divertor included experiments in hydrogen, deuterium, and tritium plasmas; experiments at a range of plasma currents; and experiments in a range of plasma triangularities from $\delta \approx 0.14$ to 0.38. A fit to the data showed that for fixed plasma shape, the critical pedestal pressure could be described by a scaling of $p_{ped} \propto I_p\sqrt{MT_{ped}}$. However, it was noted that pedestal pressures of the hydrogen plasmas studied appeared to
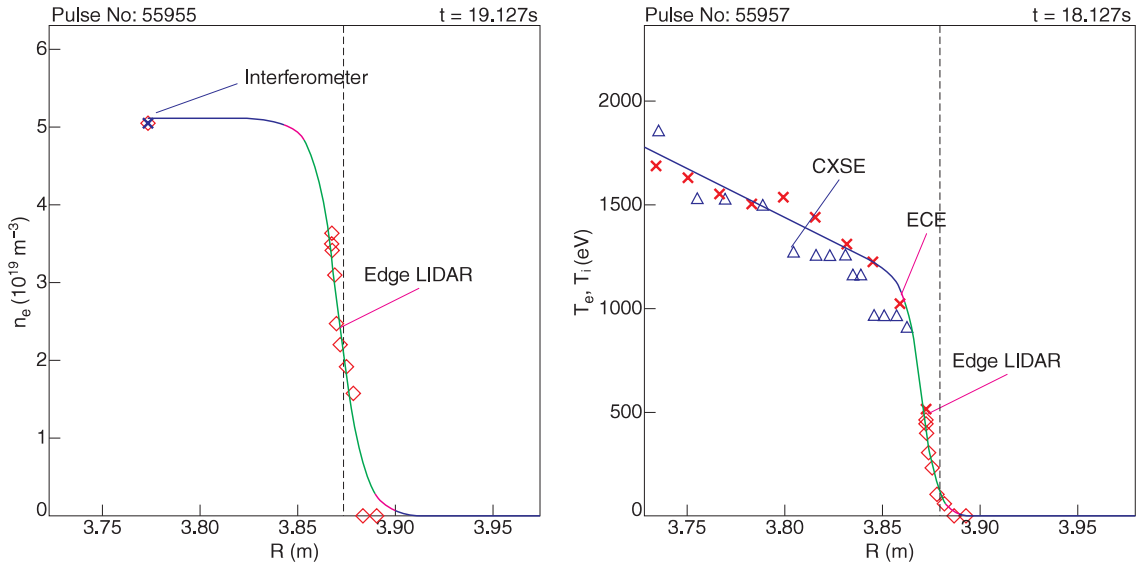
Fig. 27. Radial edge profiles of electron density and electron and ion temperature taken from interferometry, edge lidar, CXSE, and ECE. Fits of hyperbolic tangent functions to the electron density and temperature data are shown as a solid line. (From Ref. 130.)

have a somewhat weaker current scaling (see Fig. 7). The energy confined within the pedestal region, W_{ped}, was found to scale as $W_{ped} \propto I_p^{1.2} M^{0.96}$ (Ref. 66). W_{th} was found to be strongly linearly correlated with W_{ped} for a wide range of type I ELMy H-modes,[16] indicating the importance of the pedestal region in determining the global confinement properties of JET ELMy H-modes. The critical pedestal pressure was also found to increase with increasing triangularity. This is in qualitative agreement with modeling, based on neoclassical transport in the pedestal region, with the pedestal gradient limited by MHD stability.[61,132]

The impact of toroidal field direction on the type I ELMy H-mode pedestal has also been studied. This involved a series of $I_p = 2$ MA discharges in the MkIIGB divertor in both the DOC-L and DOC-U configurations.[133] Similar discharges were performed with the toroidal magnetic field and plasma current in the forward field, ion ∇B_T drift toward the X-point, and reversed field, ion ∇B_T drift away from the X-point, directions. For each configuration and field direction, a gas-fueling scan was performed to produce a range of densities. Figure 30 shows the observed critical pedestal densities and temperatures. For both configurations, it can be seen that ≈ 20 to 40% more power is required with reversed field to achieve the same pedestal pressure as with forward field. This effect is attributed to differences in the pressure pedestal width. Pedestal measurements for these discharges show that the reversed field plasmas have a narrower pressure pedestal than an equivalent forward field discharge.

IV.C. Type I-II ELMy H-Modes

Type II ELMs, characterized by having energy confinement times comparable to those of type I ELMy H-modes but with significantly smaller ELMs, have been observed on many tokamaks.[134,135] At JET, they have mostly been found in mixed type I-II ELMy H-modes. However, pure type II ELMs are observed in quasi-double-null (QDN) operation, discussed in Sec. IV.D.

Type II ELMs were first observed in JET with the MkIIGB divertor.[17,18] As reported in Ref. 18, a series of high-triangularity, $\delta \approx 0.47$, discharges was produced with the MkIIGB divertor with plasma current and magnetic field of 2.5 MA and 2.7 T. The discharges were heated with 13.5 to 15 MW of NBI. The gas fueling was varied from shot to shot, beginning with an unfueled discharge and increasing to a fueling of $\approx 5 \times 10^{22}$ electrons per second. The ELM behavior is shown in Fig. 31. As fueling increased, ELM frequency at first increased up to a maximum of ≈ 24 Hz. However, as gas fueling was increased still further, the ELM frequency decreased until the type I-III threshold was reached. Similar behavior has been observed in other JET plasmas. For the discharges in the region where ELM frequency decreases with fueling, the D_α is observed to change, Fig. 32. Compared with unfueled discharge, 52009, the D_α emission from fueled discharge 52308 can be seen to have a higher baseline level and to have small and irregular oscillations between the type I ELMs. As, for discharge 52308, the energy confinement time, pedestal pressure, and pedestal density are all observed to be close to the values for type
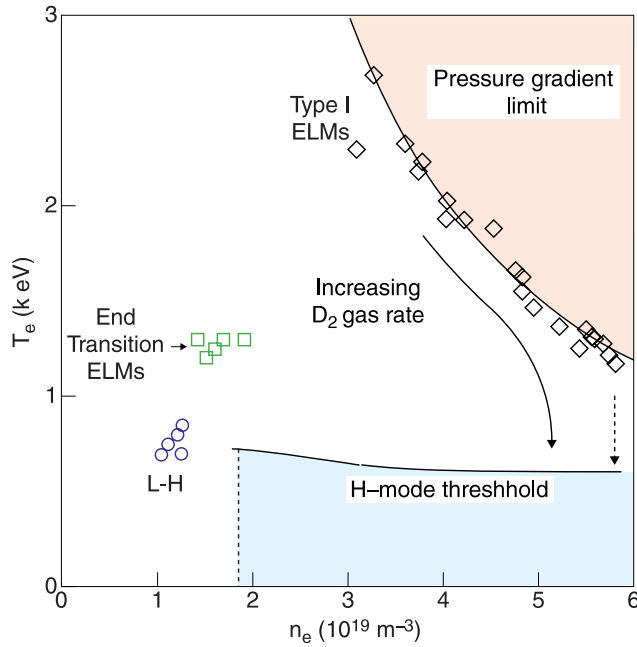
Fig. 28. Plot of edge electron temperature versus density for a series of vertical target ELMy H-modes with varying rates of gas fueling. The temperature and density values at the pressure gradient limit (diamonds) are representative of values at the top of the edge electron pedestal taken just prior to an ELM crash. The edge electron temperature and density at the L-H transition (circles) and at the end period of the transition ELMs (squares) are shown for comparison. At highest gas-fueling rates, the edge electron pressure begins to deviate from the curve of approximately constant pressure (the dashed arrow). In a few cases, transitions back to L-mode have been observed; here the curve for the H-mode threshold is schematic. (From Ref. 12.)

I ELMy H-mode discharge 52009. The observed irregular oscillations are different in nature from the more regular type III ELMs. Instead, the observed behavior is consistent with the mixed type I-II regime previously observed in ASDEX Upgrade[135] and JT-60U (Ref. 136). In addition, an enhancement of the inter-ELM density and magnetic fluctuations in the range ≈ 10 to 30 kHz is observed in the JET type I-II regime, which is consistent with the observations on other machines.[135] This is illustrated in Fig. 33, where type I ELMy H-mode discharge 52008 is compared with discharge 52308. The inter-ELM magnetic fluctuations for discharge 52308 can be seen to be approximately four times higher than for the type I ELMy H-mode in the frequency range from 10 to 40 kHz. This indicates a similar increase in the MHD turbulence. Density fluctuations show a similar trend. For frequencies ≥ 50 kHz, the magnetic fluctuations are smaller for discharge 52308 than for the type I ELMy H-mode by around an order of magnitude. The increased MHD fluctuation activity observed during the type II

(a)

(b)
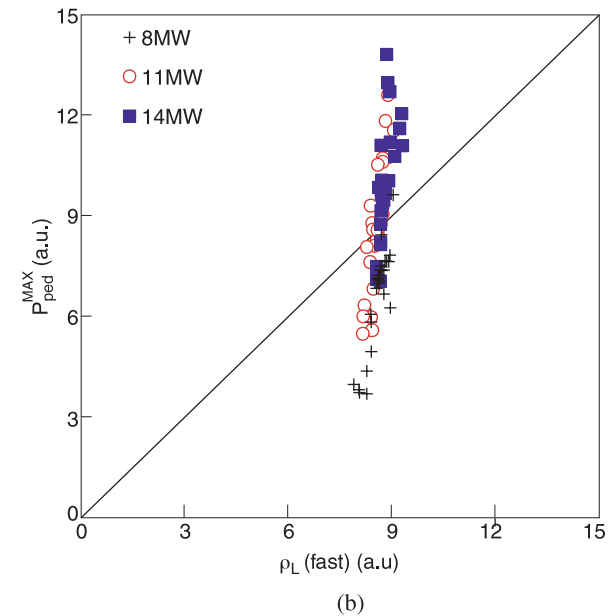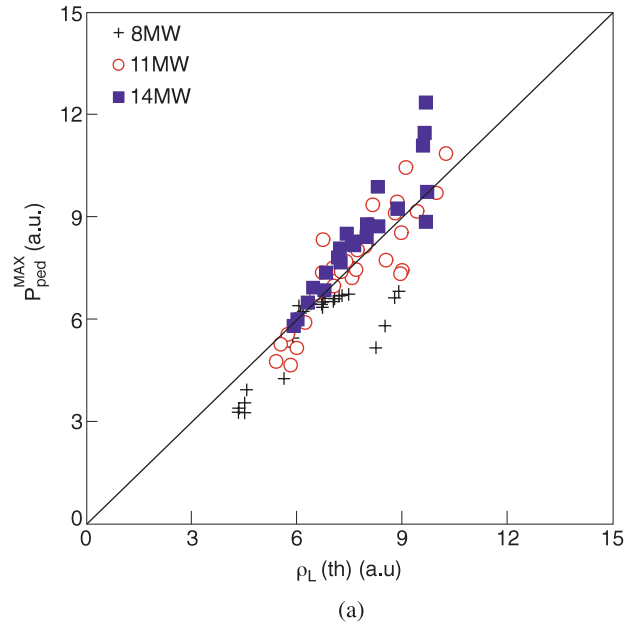
Fig. 29. Maximum edge pedestal pressure plotted as a function of (a) the Larmor radius for the thermalized ions (normalized to the average of all data) and (b) the Larmor radius for fast ions (normalized to the average of all data). The data set in both cases is from a series of ELMy H-modes produced at JET with the MkIIA divertor at 2.6 MA and 2.7 T in a single plasma configuration with $\delta = 0.23$. Gas fueling was varied and three different NBI power levels were used: 8, 11, and 14 MW. (From Ref. 16.)

ELM phases has been identified with washboard modes.[137] A study of interferometry and reflectometry data indicates that these fluctuations are radially located around the pedestal top.[22]
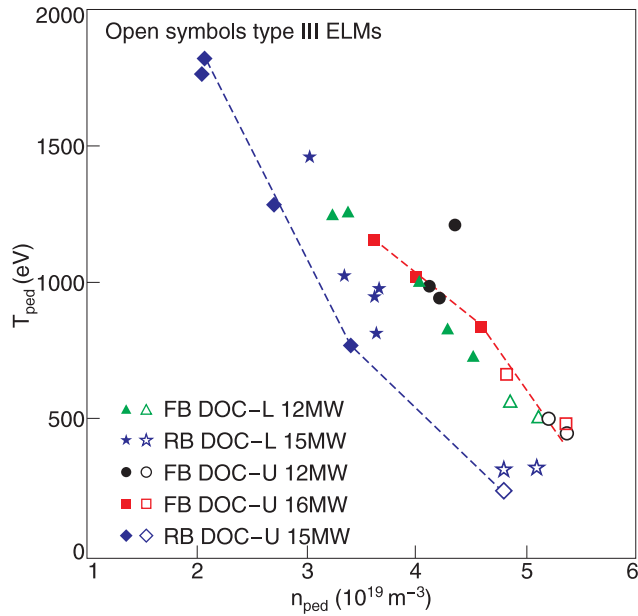
Fig. 30.   Pedestal electron temperature versus pedestal plasma density for a set of $I_p = 2$ MA forward field (FB) and reversed field (RB) discharges in JET. Two plasma configurations were used, the DOC-L and DOC-U (Ref. 133). The dashed lines highlight the forward field and reversed field discharges performed with 15 to 16 MW of auxiliary heating power in the DOC-U configuration. (From Ref. 133.)

Fig. 31.   Time traces of the D_α emission from the outer divertor region for five discharges in a gas-fueling scan at 2.5 MA, 2.7 T, and $\delta = 0.47$. The pulses are in order of increasing gas fueling, with the lowest fueling in the uppermost box. All discharges are NBI-heated with a high-power flat of 13.5 to 15 MW beginning at ≈ 17 s and extending to ≈ 20 s for discharge 52308 and beyond 22 s for the rest. The discharge number is given for each box, along with the mean type I ELM frequency during the main type I or type I-II ELMy H-mode phase. (From Ref. 18.)

A study of the type I-II ELMy H-mode operational space was made by performing gas scans in two high-triangularity, $\delta \geq 0.42$, configurations with the MkIIGB divertor for a range of plasma currents and safety factors q (Ref. 138). Type I-II ELMy H-modes were found to exist for a range of currents (1 to 3.5 MA) and safety factors and to be synonymous with high-confinement, $H_{98(y,2)} \approx 1$, high-density, $n_e \approx n_{Gr}$, operation, where $H_{98(y,2)}$ is the energy confinement time τ_E normalized to the IPB98(y,2) scaling,[13] $\tau_{98(y,2)}$, and n_{Gr} is the Greenwald density limit. Type I-II ELMy H-modes were produced in plasmas with safety factor at the 95% normalized flux surface q_{95} of $q_{95} = 3.0$ and $q_{95} = 3.6$, but not at the highest safety factor explored, $q_{95} = 4.6$ (Ref. 18). For all the type I and type I-II ELMy H-modes in the study, the ratio of the pedestal energy to the total plasma thermal energy W_{th} was found to be in the range 0.4 to 0.5. In this way, the higher pedestal pressure of the type I-II ELMy H-modes was reflected in their having a higher global confinement time. Across the whole data set, pedestal pressure was found to scale with plasma current as $p_{ped} \propto I_p^2$ or slightly weaker. This is consistent with an ideal ballooning limit stability criterion. The pedestal pressure of the type I-II ELMy H-modes was systematically above the observed scaling. Type

I-II ELMy H-modes have also been observed in a QDN configuration.[22]

IV.D. Type II ELMy H-Modes

The first pure type II ELMy H-modes on JET were achieved in a QDN configuration with the separation between the inner and outer separatrices, mapped to the outboard midplane, $\Delta_{sep} < 1$ cm (Ref. 22). The required conditions were produced by performing an identity experiment between JET plasmas and a type II ELMy H-mode plasma on ASDEX Upgrade. In an identity experiment (see Sec. II.F.1), plasma parameters are scaled such that two plasmas of different sizes have equivalent nondimensional plasma physics parameters. In the experiment discussed here, the parameters from a type II ELMy H-mode on ASDEX Upgrade were scaled up to JET. The ASDEX Upgrade plasma was a type II ELMy

Fig. 32. Comparison of the D$_\alpha$ emission from the outer divertor region for two of the pulses in Fig. 31 (top two panels). The respective total plasma stored energies (taken direc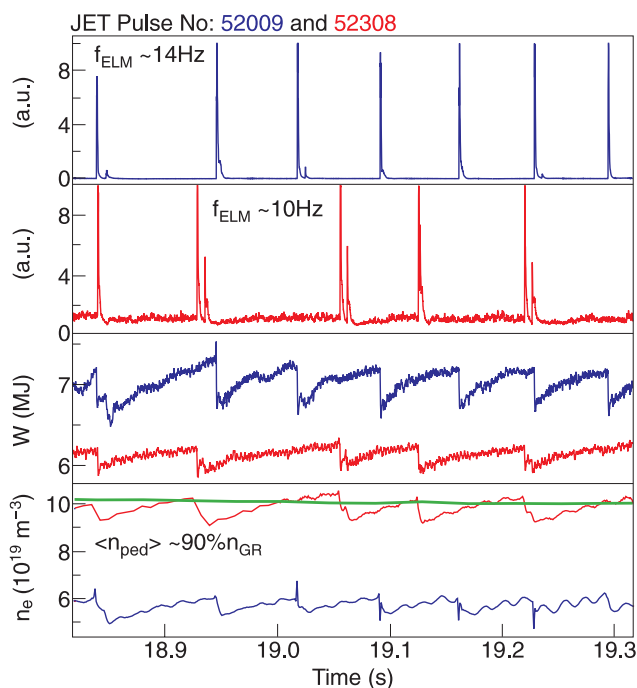tly from the diamagnetic measurement, third panel) and line average densities (bottom panel) are also shown. The dashed line in the latter represents the Greenwald density limit. (From Ref. 18.)
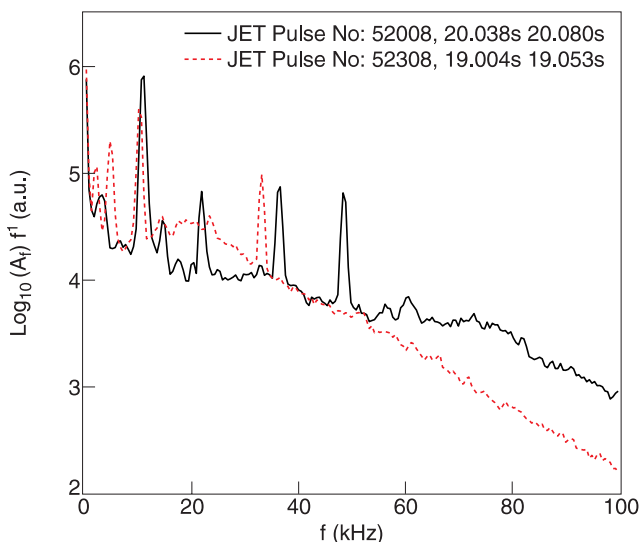

Fig. 33. Comparison of the intensity of the inter-ELM magnetic field fluctuations, associated with MHD turbulence, for pulses 52008 and 52308. Discharge 52008 is identified as having type I ELMs and discharge 52308 as having type I-II ELMs. The vertical axis is in arbitrary units. (From Ref. 18.)

H-mode in a QDN configuration with $I_p \approx 1.0$ MA, $B_T \approx$ 2.4 T, $q_{95} \approx 4.1$, $n_{ped} \approx 6.5 \times 10^{19}$ m^{-3}, and $T_{ped} \approx 350$ eV. The dimensionally identical JET pulse was in a matched configuration with $I_p \approx 0.87$ MA, $B_T \approx 1.17$ T, $q_{95} \approx 4.1$, $n_{ped} \approx 2.1 \times 10^{19}$ m^{-3}, and $T_{ped} \approx 260$ eV. The JET discharges produced had long phases with high confinement, $H_{98(y,2)} \approx 1$, no type I ELMs, stationary pedestal parameters, and MHD signatures consistent with type II activity. They were thus identified as pure type II ELMy H-modes. Figure 34 shows the time traces for two similar discharges: one with a pure type II ELMy H-mode phase (62430) and one without (62428). For discharge 62430, after the initial turning on of NBI heating power, an ELM-free phase is followed by a brief type III ELMy H-mode phase, which in turn is followed by a type II ELMy H-mode phase of ≈ 1.5 s ($\approx 4\tau_E$), where the pedestal
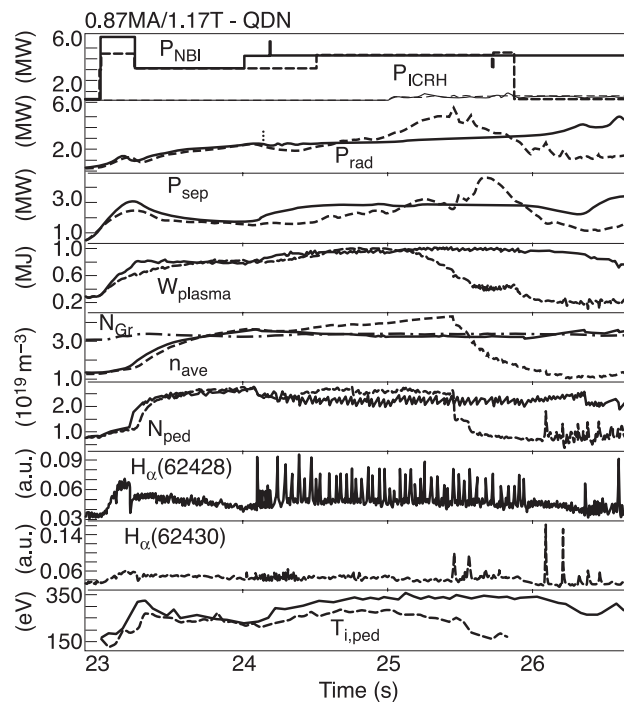
Fig. 34. Selected time traces for two pulses of a JET/ASDEX Upgrade identity experiment: solid lines, pulse 62428 (type I ELMs), and dashed lines, pulse 62430 (type II ELMs). From top to bottom: NBI and ICRH input powers (P_{NBI} and P_{ICRH}, MW); total radiated power P_{RAD} (MW); power across the separatrix P_{sep} (MW); plasma stored energy (MJ); line average density n_{ave} and Greenwald density limit n_{Gr} (dotted line) in units of 10^{19} m^{-3}; pedestal density n_{ped} in units of 10^{19} m^{-3}; divertor D$_\alpha$ emission (62428, arbitrary units); divertor D$_\alpha$ emission (62430, arbitrary units); and pedestal ion temperature $T_{i,ped}$ (eV). The shaded region highlights the phase of discharge 62430 from the start of the auxiliary heating, through the transition to H-mode ($t \approx 23.2$ s), until the loss of confinement due to core radiative collapse. (From Ref. 22.)

density and temperature remain constant in the absence of type I ELM crashes. The broadband magnetic turbulence associated with type II ELMs is observed during this phase.[139] The line average density and total radiated power can be seen to rise during this phase, and the discharge is terminated by a core radiative collapse. However, this behavior is not common to all type II ELMy H-modes. Discharge 62428 has essentially the same behavior through the early ELM-free phase but its NBI power is stepped up at ≈ 24 s, with the result that the pedestal temperature rises and the plasma enters a type I ELMy H-mode phase. The fact that discharge 62428 remains in type II ELMy H-mode when there is a similar step in NBI power at ≈ 24.5 s at similar global and local parameters suggests that the parameter space for access to type II ELMs in this experiment was narrow. The exact parametric dependence remains to be found.

At present, pure type II ELMy H-modes have been produced only in a limited region of parameter space, for which $q_{95} \geq 4$ and $\nu^* \geq 0.23$. To be relevant to burning plasmas, it must be demonstrated that type II ELMy H-modes can be maintained at lower safety factors and collisionalities. Further studies will be made in this area.

IV.E. Type III ELMy H-Modes

Type III ELMy H-modes are observed in all diverted tokamaks. They are characterized by having ELMs that are smaller and at higher frequency than those of type I ELMy H-mode.[134,140] Energy confinement is generally lower than in equivalent type I ELMy H-modes. A comprehensive review of the type III studies performed at JET can be found in Ref. 116. ELM mitigation through impurity seeding of ELMy H-modes on JET commonly results in type III ELMy H-modes. Type III ELMy H-modes produced in this way are discussed in Sec. VII. This section focuses on type III ELMy H-modes that are not seeded by impurities.

In JET, type III ELMy H-modes have been observed at a wide range of configurations, magnetic fields, and plasma currents and over density ranges from 20 to 100% of the Greenwald density limit. Type III ELMy H-modes are observed when the loss power P_{loss} is raised to just above the L-H power threshold and remains until the power threshold for access to type I ELMs P_{typeI} is reached. For $P_{loss} \approx P_{typeI}$, type I ELMy H-mode phases are often observed, but these will often be followed by a transition to a type III ELMy H-mode. In some cases this behavior will be cyclical. P_{typeI} is observed to decrease with increasing triangularity.[141] In edge parameter space, type III ELMs are observed until a critical temperature T_{crit} is reached, after which there is a transition to type I ELMs. Studies at JET (Ref. 116) have found the critical temperature to scale as $T_{crit} \propto B_T^2$ at fixed safety factor. The density dependence is more complex, with the critical temperature scaling as $T_{crit} \propto n_{e,ped}^{-1}$ at low density, or equivalently low collisionality, but being independent of

density at higher density, or equivalently high collisionality. For all the densities and collisionalities studied at JET, the dependence of the type III–to–type I transition on power, triangularity, and isotopic mass appears to be similar.[116] In addition, the ELM energy loss is always seen to be lower for type III ELMs when compared to that for type I ELMs on either side of a transition. This leads to the conclusion that there is a common physics mechanism for all the type III ELMs observed at JET.

One proposed model is that of Pogutse et al.[142] and Igitkhanov and Pogutse,[143] in which type III ELM crashes are caused by the resistive interchange instability, which is driven by magnetic flutter. The upper bound for type III ELMs is when the radial electric field just inside the separatrix becomes strong enough to stabilize the magnetic flutter. The asymptotic scaling of the resulting condition on T_{crit} can be expressed as

$$T_{crit} \sim (c_\tau^2 c_F c_\nu)^{6/17} \frac{q_{95}^{24/17} R^{4/17} B_T^{10/17}}{M^{8/17} s_{95}^{12/17}}$$

$$\text{for } \lambda_e < c_\nu q_{95} R$$

and

$$T_{crit} \sim (c_\tau^2 c_F)^{6/5} \frac{q_{95}^{18/5} B_T^2}{R^{2/5} M^{8/5} s_{95}^{12/5} n_{e,ped}^{6/5}}$$

$$\text{for } \lambda_e > c_\nu q_{95} R \quad , \qquad (1)$$

where c_τ, c_F, and c_ν are fitting constants, R is the plasma major radius, M is the isotopic plasma mass normalized to that of hydrogen, s_{95} is the safety factor shear s at the 95% normalized flux surface, and λ_e is the mean electron free path. Figure 35 shows the agreement of this model with data from type III ELMy H-modes produced at JET with similar shapes, $\delta \approx 0.22$ to 0.25, and safety factors, $q_{95} \approx 3.0$ to 3.3, for two different magnetic field ranges, $B_T \approx 2.4$ and 3.4 T (Ref. 116). Similar agreement has been seen between the Pogutse-Igitkhanov model and type III ELMy H-modes on ASDEX Upgrade, DIII-D, and Alcator C-Mod.[143] However, comparison of the model with $n_{e,ped}$ and $T_{e,ped}$ data from type III ELMy H-modes on JET with hydrogen, deuterium, and tritium plasmas found that the observed isotopic mass dependence was not well represented by the Pogutse-Igitkhanov model. In addition, comparison of the model with $n_{e,ped}$ and $T_{e,ped}$ data from type III ELMy H-modes on JET with a range of safety factors found that the observed q_{95} dependence was also not well represented by the model.

An alternative model for type III ELMs at high collisionality is that of Chankin and Saibene.[144] In this model, type III ELMs, at high densities, are driven by the resistive ballooning instability. The key parameters in determining the resistive ballooning instability threshold are the pressure gradient normalized to the ballooning limit,
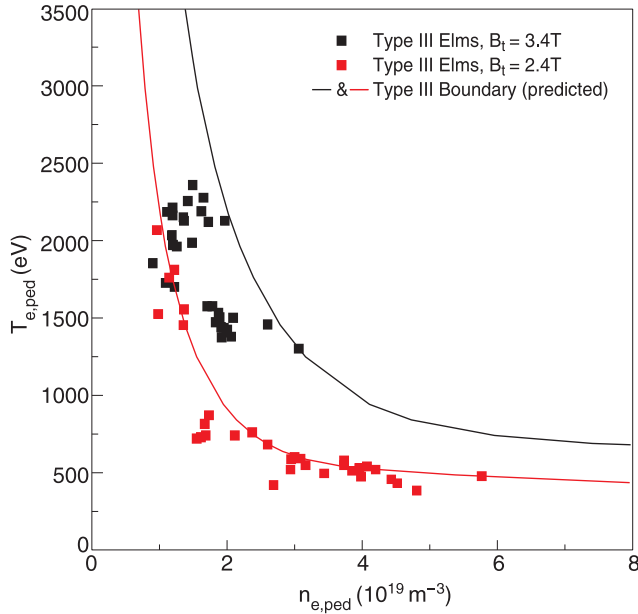
Fig. 35. Pedestal $n_e - T_e$ diagram for discharges with 2.5 MA and 2.4 to 2.6 T and with 3.3 to 3.6 MA and 3.4 T. $n_{e,ped}$ is measured with the far-infrared interferometer's outermost channel and $T_{e,ped}$ with the ECE hetero-dyne radiometer. The data are compared with the critical temperature (or upper boundary) for type III ELMs predicted by the model of Pogutse et al.[142] and Igitkhanov and Pogutse.[143] (From Ref. 116.)
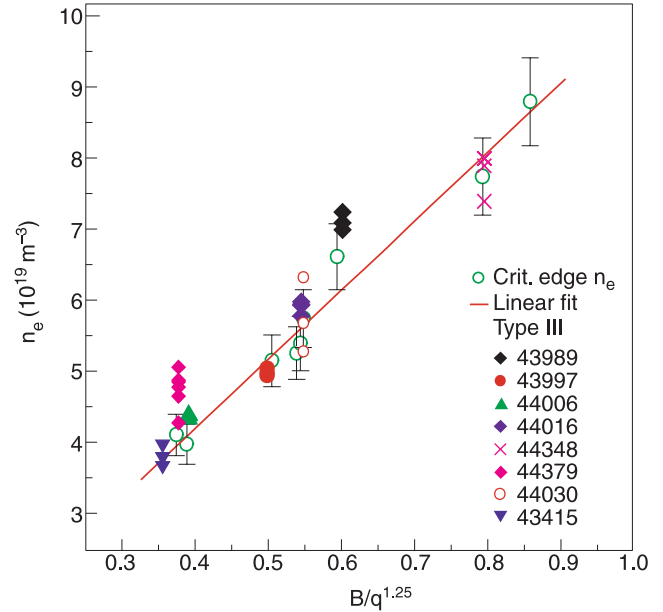

Fig. 36. Pedestal density at the type I-III ELM transition and during type III ELMs. (From Ref. 116.)

$F = q^2 R \nabla \beta / f(s)$, and the normalized collisionality, $\nu_e^* = Z_{eff} n_e qR/T_e^2$, where β is the normalized plasma pressure and Z_{eff} is the effective charge. Asymptotically, the model predicts a scaling for the threshold pedestal electron density of

$$n_{crit} \sim \frac{B_T f(s)^{1/2}}{q^{5/4} R^{3/4} Z_{eff}^{1/4}} \quad . \tag{2}$$

Experimentally, at high density, the transition from type III to type I ELMs on JET is observed to scale as $n_{crit} \propto B_T/q^{5/4}$ (Fig. 36). This agrees well with the Chankin-Saibene model.

A study of type III ELMs in internal transport barrier (ITB) plasmas, at low collisionality,[145] found that the power threshold for the type III to type I transition was dependent on the edge current profile, with a large fraction of current at the edge being favorable for maintaining the type III regime at higher powers. Current ramp experiments in type III ELMy H-modes[146] also indicate a sensitivity of the threshold for the type III to type I transition to the current fraction at the edge at low collisionality. This suggests that current-driven peeling modes may play a role in type III ELM crashes, at least at low collisionality. Numerical simulations have shown that current-driven peeling modes can be stabilized by increased pressure gradients at high power,[147] which would provide a mechanism for the transition to type I ELMs.

IV.F. Grassy ELMy H-Modes

Grassy ELMy H-modes are characterized by good confinement with small ELMs at high β_{pol}, high l_i, high δ, and high q_{95}, where β_{pol} is the plasma pressure normalized to the poloidal component of the magnetic pressure. The grassy ELMy H-mode was first observed on JT-60U (Refs. 148 and 149). In JET, grassy ELMy H-modes have been produced by performing a β_{pol} scan in ELMy H-modes in a QDN configuration with $\Delta_{sep} < 1$ cm, $\delta \approx 0.45$, $B_T = 2.7$ T, $I_p = 1.2$ to 1.5 T, and $n_e \geq 0.7 n_{Gr}$ (Ref. 22). By varying the auxiliary heating power, β_{pol} was varied in the range ≈ 1.1 to 1.9. For $\beta_{pol} \lesssim 1.5$, type I ELMy H-modes are observed, but for $\beta_{pol} \gtrsim 1.6$ to 1.7, type I ELMs disappear and the D_α emission shows irregular oscillations of the kind seen on JT-60U. Confinement and density remain high, $H_{98(y,2)} \approx 1.0$ to 1.2 and $n_e \approx 0.85 n_{Gr} q_{95}$ was observed to be in the range 6 to 7. The pedestal and core profiles remain stationary for several confinement times, indicating that edge transport and the grassy ELMs are sufficient to transport the power and particles normally transported by the type I ELMs. Studies of magnetic fluctuations show that in contrast to type I ELMy H-modes, the discharges with $\beta_{pol} \gtrsim 1.6$ to 1.7 have virtually no fluctuations above 10 kHz. This is consistent with the observed behavior for grassy ELMs in JT-60U (Ref. 139).

To study the impact of l_i on the pedestal conditions, the β_{pol} scan was compared with a series of low-l_i, $l_i \approx 0.85$, single-null, ELMy H-modes in which β_{pol} was varied in a similar range, ≈ 1.1 to 1.9. This single-null configuration has $\Delta_{sep} \gtrsim 4$ cm and κ and δ similar to those of the QDN configuration above, and a similar q_{95} range. All of these discharges were found to be type I ELMy H-modes. Figure 37 shows the pedestal pressure normalized to the plasma current,[150] p_{ped}/I_p^2, for both this low-l_i data set and the high-l_i data set of the previous paragraph. For the high-l_i plasmas, p_{ped}/I_p^2 remains almost constant with β_{pol}. Thus, in contrast to the transition from type I to type III ELMy H-modes, the transition from type I to grassy ELMy H-modes does not lead to a degradation of pedestal pressure. For the low-l_i plasmas, p_{ped}/I_p^2 increases with increasing β_{pol}, as indeed does their normalized global confinement, which increases from $H_{98(y,2)} \approx 0.7$ to $H_{98(y,2)} \approx 1.1$. The pedestal collisionality of the high-l_i, grassy ELMy H-mode discharges can also be seen to be higher than that for the low-l_i, type I ELMy H-modes. As for type II ELMy H-modes, then, grassy ELMs have currently been observed on JET only at relatively high values of q_{95} and ν^*. Because of the correlation between collisionality and β_{pol} in the existing experiments, it may even be that a sufficiently high ν^*, rather than a sufficiently high β_{pol}, is required for the formation of grassy ELMs. This can be seen in Fig. 37. To be relevant to burning plasma experiments, it has to be shown that the grassy ELM operational space can be extended to lower safety factors and collisionalities.
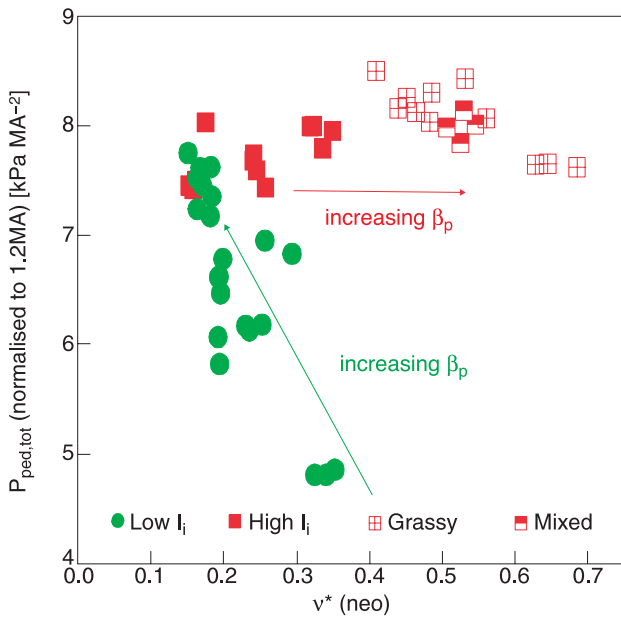

Fig. 37. p_{ped}, normalized to I_p^2, for high-l_i, $l_i > 1$, and low-l_i, $l_i \approx 0.85$, H-modes in β_{pol} scans. (From Ref. 22.)

IV.G. Conclusions

JET studies of the pedestal physics and ELM properties of type I, type I-II, type II, type III, and grassy ELMy H-modes have been presented. A range of diagnostics has enabled reliable measurement of the key physics parameters at the pedestal top. However, diagnosis of the gradient region within the pedestal has been limited. Ongoing diagnostic upgrades are expected to significantly improve this situation.

Type I ELMy H-modes have been observed over a wide range of plasma parameters. A positive dependence of critical pedestal pressure upon edge density, plasma current, isotopic mass, and triangularity has been observed and empirical scalings determined. Over a wide range of experiments, the pedestal energy is found to be strongly correlated with the total plasma thermal energy, indicating that knowledge of the pedestal behavior and ELM size is critical for determining the global confinement of type I ELMy H-modes.

Type II ELMs have been observed in JET, first in mixed type I-II ELMy H-modes. They have been shown to have the same characteristic behavior as those observed in other machines. A wide operational space for type I-II ELMy H-modes has been identified. The key parameters for their existence on JET appear to be high triangularity and plasma density. Pure type II ELMy H-modes have been achieved in a QDN plasma configuration, but further studies are required to determine their operational space. Grassy ELMy H-modes have also been produced in JET, also in a QDN configuration, and have been shown to have characteristics similar to those observed on JT-60U. The impact of β_{pol} on their critical pedestal pressure has been determined. However, grassy ELMy H-mode operation has been restricted to high safety factors and collisionalities, and it remains to be seen if they can be produced in more ITER-relevant conditions.

Type III ELMy H-modes are widely observed on JET. For given plasma parameters, their pedestal temperature has been found to be limited to a critical value above which there is usually a transition to a type I ELMy H-mode. The dependence of the critical pedestal temperature upon density, safety factor, isotope mass, and magnetic field has been studied. Both the Pogutse-Igitkhanov and Chankin-Saibene models have been found to describe some of the observed critical pedestal temperature, but a single model that describes all of the physics remains to be found.

In contrast to the case for type I and type III ELMy H-modes, the parameter space for type I-II, type II, and grassy ELMy H-modes remains to be fully explored on JET. Because of their low ELM losses, type II and grassy ELMy H-modes are of strong interest, and it is crucial that future JET studies determine whether their operational space can be extended to parameters more relevant to burning plasmas. Improvement of edge diagnosis to enable resolution of the pedestal gradient region is

crucial for validating and improving the existing physics models for all ELMy H-mode behavior on JET.

V. MAIN PLASMA ENERGY AND PARTICLE LOSSES DURING ELMs AND FLUXES TO PLASMA-FACING COMPONENTS

V.A. Introduction

Operation of next-step fusion devices with high fusion gain such as ITER, for which the objective is to achieve $Q_{DT} \geq 10$ in inductive operation, requires the "production" of high-density plasmas ($\langle n_e \rangle \geq 10^{20}$ m^{-3}) with high energy confinement time ($H_{98(y,2)} \sim 1$). The fact that these plasmas are believed to be achievable in ITER is based on scalings from type I ELMy H-mode discharges in current experimental devices with $q_{95} \geq 3$ (Ref. 151). A characteristic feature of the type I ELMy H-mode operating regime is the transient release of energy from the confined plasma onto plasma facing components (PFCs) by type I ELMs, which in ITER can contribute significantly to the overall erosion rate and to the reduction of the lifetime of these components.[152,153] This issue has led to the development of two research lines in the area of H-mode physics:

1. understanding of the physics processes responsible for the loss of plasma energy during ELMs, its transport onto PFCs, and its scaling to ITER

2. development of H-mode regimes that can match the requirements with regard to plasma density and energy confinement in ITER while maintaining very small ELM transient loads (type II and type III ELMs).

This section describes the contributions of JET to the first line of research, and Secs. VII and VIII deal with the second one.

Two lines were followed initially to develop steady-state ELMy H-mode phases at JET: high-β discharges in single-null configuration and high-fueling double-null discharges.[154] In the first case, repetitive type I ELMs were achieved for phases of 1 to 2 s with frequencies of ~5 Hz and normalized ELM energy losses $\Delta W_{ELM}/W_{plasma} \sim 5$ to 10% (where ΔW_{ELM} is the ELM energy loss and W_{plasma} is the total plasma energy). In the second case, type III ELMy H-mode plasmas were maintained for periods longer than 10 s. Given the restricted operating range at which these ELMy H-mode conditions were achieved and the availability of diagnostics, no detailed analysis of ELM energy and particle losses for these ELMy H-mode discharges has been carried out.

The introduction of the in-vessel divertor coils and the divertor cryopump with the MkI divertor in 1994, together with the associated decrease of plasma volume (by 20 to 30%) and triangularity of the JET plasmas, allowed the exploration of steady-state ELMy H-modes with type I and type III ELMs in a wide range of plasma conditions. During the MkI experimental campaigns, effort on ELM physics concentrated on the characterization of ELM power fluxes to PFCs (Ref. 155) and on the achievement of high–radiative fraction fully detached H-modes,[156] with less emphasis on the characterization of the main plasma ELM losses. Several important results concerning ELM energy fluxes to PFCs, described in Sec. V.C, were identified for the first time in this operation period, which have been confirmed by subsequent experiments at JET and other devices and by ELM modeling.

The installation of the MkIIA divertor at JET allowed long plasma operation in ELMy H-mode without the need of plasma sweeping. This, together with the recognition of the problems that ELMs pose for the operation of ITER and the improvement of the available diagnostics at JET (in particular, the fast divertor infrared camera and the ECE radiometer for fast pedestal electron temperature measurements) led to a significant increase of the research in the area of ELM losses and fluxes to PFCs at JET described in Secs. V.B and V.C (Refs. 12 and 157). This provided the first systematic results on ELM characteristics at JET, which were then continued with the installation of the MkIIGB divertor. The width and breadth of ELM research activities at JET increased markedly in 2000 and have continued with this trend to the present. This, together with subsequent improvements of diagnostics, has allowed detailed investigations of the characteristics and physics mechanisms involved in the loss of energy and particles from the main plasma and its transport to PRCs during ELMs by both empirical scalings and the development and validation of models. The description of the results obtained in this last period of JET operations constitutes the bulk of this section.

V.B. Measurements of ELM Energy and Particle Losses at JET and Their Relation with Global and Pedestal Plasma Characteristics

V.B.1. Global Behavior of ELM Energy and Particle Losses

The initial studies carried out with the MkIIA divertor[158] confirmed that the type I ELM regime achieved at JET showed global behavior similar to that of other tokamaks such as ASDEX Upgrade and DIII-D (Ref. 140), with the ELM frequency increasing with input power and decreasing with plasma current as $f_{ELM} \sim P_{inp}/I_p^2$ for discharges with no gas-fueling plasma conditions. The experiments carried out at JET determined for the first time in a systematic study the influence of gas fueling on ELM frequency[158] and energy loss[12,158] and the effect of plasma shaping both on the pedestal plasma parameters and the type I ELM energy losses.[12,16] These results
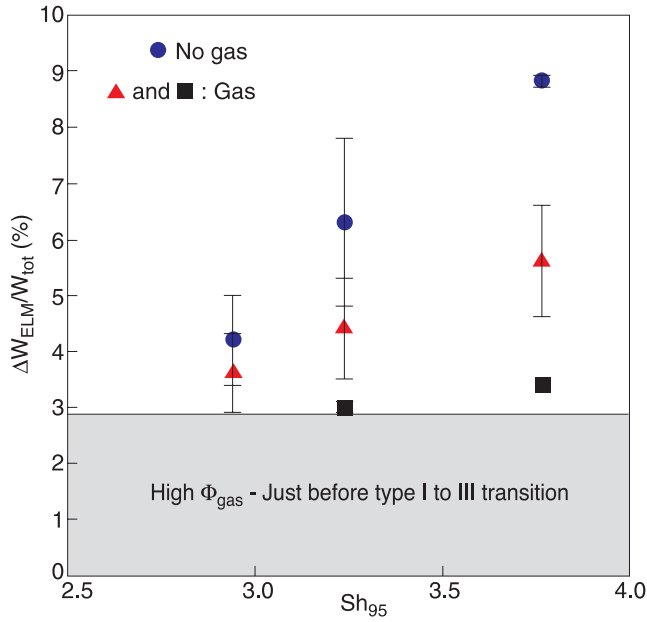
Fig. 38. Percentage of plasma energy loss per ELM versus Sh_{95}, which is the average shear calculated over a magnetic surface corresponding to 95% of the poloidal flux (which increases with plasma triangularity δ) for gas-fueling rates Φ_{gas} of 0 (circles), 1.2×10^{22} s^{-1} (triangles), and 2.3×10^{22} s^{-1} (squares) in the type I ELM regime. Losses below ~3% of W_{tot} (total plasma energy) cannot be measured. (From Ref. 16.)

Fig. 39. ELM frequency (f_{ELM}), normalized ELM power loss ($f_{ELM} \times \Delta W_{ELM}/P_{input}$), and ELM particle outflux ($f_{ELM} \times \Delta N_{ELM}$) versus gas-fueling rate Φ_{gas} for discharges with $I_p = 2.5$ MA, $B_T = 2.4$ to 2.7 T, $P_{input} = 14$ to 17 MW, and medium (~0.3) triangularity at JET. Lines are to guide the eye. (From Ref. 159.)

showed that although high-triangularity/shaping plasmas have a lower intrinsic f_{ELM} and larger ΔW_{ELM} than low-triangularity/shaping plasmas for unfueled conditions, this difference in ΔW_{ELM} was much smaller for high-density/fueling conditions, as shown in Fig. 38 (Ref. 16). Increasing gas fueling leads not only to a decrease of ΔW_{ELM} but also to an increase of the ELM frequency f_{ELM}, which compensates the decrease of ΔW_{ELM}, so that the power outflux associated with ELMs increases only weakly with fueling, as shown in Fig. 39 (Ref. 159). Together with these changes caused by increasing fueling, there is a moderate decrease of the pedestal plasma pressure and total plasma energy.[16] A model was developed to describe the correlation of these two effects for gas-fueled and impurity-fueled discharges at JET (Ref. 58). This model provided, for the first time, a correlation between the achievable $\Delta W_{ELM}/W_{plasma}$ and the normalized plasma confinement (either with respect to the ITER-89 L-mode scaling or the ITER-93 H-mode scaling), and it predicted that ELMs that lead to a small energy loss $\Delta W_{ELM}/W_{plasma} \sim 1$ to 3% are intrinsically linked to plasmas with very poor energy confinement ($H_{93} < 0.7$) and, thus, incompatible with the requirements in ITER. This physics view of the relation between ELM energy losses and overall plasma confinement was
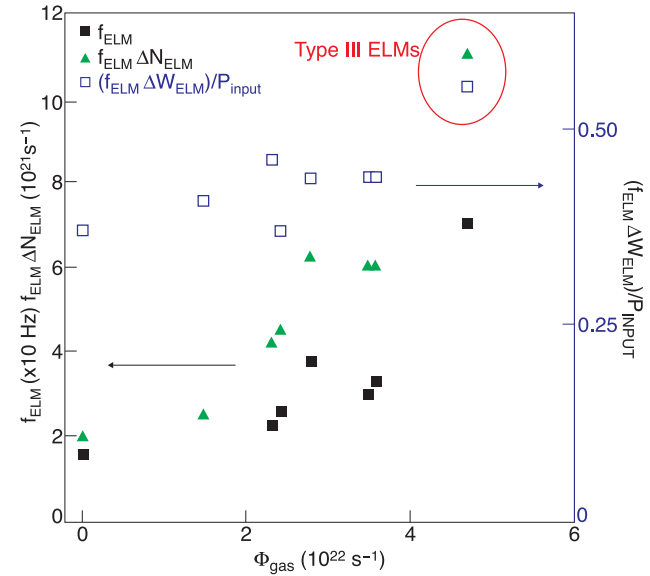
not only applicable to JET results but was also in agreement with the trends observed in ASDEX Upgrade.[160] In contrast, the normalized losses of plasma particles caused by ELMs, $\Delta N_{ELM}/N_{plasma}$, change only weakly with the increase of f_{ELM} by gas fueling. This leads to an increase of the total particle losses induced by ELMs with increasing fueling rate (and f_{ELM}), as shown in Fig. 39 (Ref. 159).

Analysis of ELM energy loss measurements from ASDEX Upgrade, DIII-D, and JET (Ref. 161) indicated that the correlation between f_{ELM} and $\Delta W_{ELM}/W_{plasma}$, although valid for the JET experiments analyzed in Ref. 58, was the result of the inter-ELM energy transport and not, as such, directly linked to the ELM energy loss. The ELM energy loss itself is thus determined by physics processes associated with the pedestal plasma parameters and their gradients (chiefly the pedestal plasma collisionality), whereas the ELM frequency would be a consequence of the inter-ELM transport and the MHD stability of the plasma edge to peeling-ballooning modes that eventually lead to the ELM crash. This new approach to the understanding of ELM physics was demonstrated by experiments at high triangularity at JET with the achievement of the so-called mixed type I-II ELMy H-mode regime.[18] In this regime, the presence of enhanced energy losses between ELMs leads to a reduction of the ELM frequency without a corresponding increase of the ELM energy loss, as shown in Fig. 40 (Ref. 159). In fact, data obtained in JET experiments spanning a
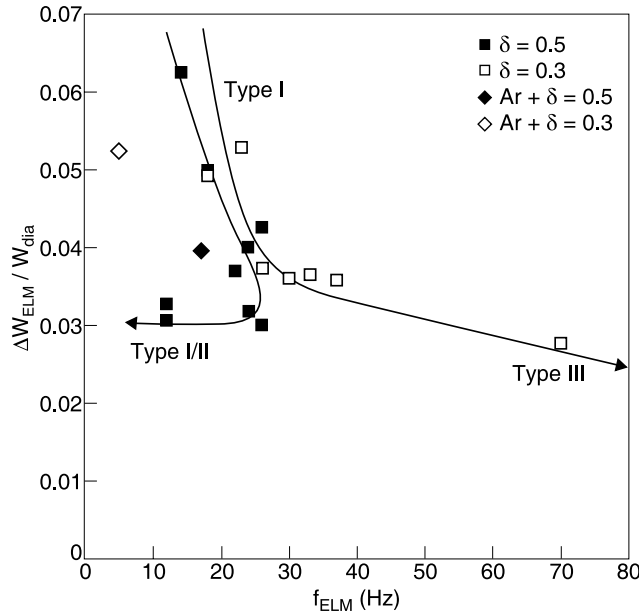
Fig. 40. Normalized ELM energy loss ($\Delta W_{\text{ELM}}/W_{dia}$) versus ELM frequency ($f_{\text{ELM}}$) for discharges with $I_p = 2.5$ MA, $B_T = 2.4$ to 2.7 T, $P_{input} = 14$ to 17 MW, and medium (~ 0.3) and high (~ 0.5) triangularity. Note the unusual decrease of f_{ELM} with constant ($\Delta W_{\text{ELM}}/W_{dia}$) for discharges with $\delta \sim 0.5$. Two discharges (at medium and high δ) with impurity seeding (Ar) are shown for comparison. Lines are to guide the eye. (From Ref. 159.)

Fig. 41. Normalized ELM energy loss ($\Delta W_{\text{ELM}}/W_{ped}$) versus pedestal plasma collisionality for a large range of type I ELMy H-mode plasmas in ASDEX Upgrade, DIII-D, JT-60U, and JET, including various plasma triangularities, ratios of P_{INPUT}/P_{L-H}, pellet-triggered ELMs, and impurity-seeded discharges (Ar). (From Ref. 20.)

large range of plasma currents, shapes, densities, and the like was instrumental in establishing the empirical correlation between the normalized ELM energy loss $\Delta W_{\text{ELM}}/W_{ped}$ (where $W_{ped} = 3k_B\langle n_{ped}\rangle\langle T_{ped}\rangle V_{plasma}$ is the pedestal plasma energy, k_B is Boltzmann's constant, $\langle n_{ped}\rangle$ and $\langle T_{ped}\rangle$ are the pedestal density and temperature averaged over the ELM cycle, and V_{plasma} is the plasma volume) and the pedestal plasma collisionality shown in Fig. 41 (Ref. 20). This empirical correlation provides an adequate first-order description of the observations from type I ELMy H-modes with good energy confinement for the present divertor tokamaks, as shown by the latest results from JT-60U (Ref. 162) and MAST (Ref. 163). Although no theory/model developed so far for the ELM energy loss is able to reproduce the observed scaling with pedestal collisionality, such dependence is consistent with the change of the nature of the ELM triggering mechanism according to the peeling-ballooning model from a more peeling-like (at low collisionalities and large bootstrap currents) to a more ballooning-like (at high collisionalities and small bootstrap currents) ELM trigger,[164] as discussed in Sec. VI.

V.B.2. Role of Transport Mechanisms and Pedestal Plasma Parameters in the Determination of ELM Energy and Particle Losses

Detailed studies of the physics processes that lead to the observed collisionality dependence have been carried out at JET. It has been found that the decrease of ΔW_{ELM} with pedestal collisionality in type I ELMy H-modes is mainly due to a decrease of the bulk plasma energy losses by plasma conduction during the ELM (Refs. 150 and 159), which is in agreement with results from DIII-D (Ref. 165), and *is not* caused by the reduction of the volume of the plasma affected by the ELM, in contrast with the initial picture from DIII-D (Ref. 165), later reconciled with the JET observations.[166]

The change of plasma energy caused by the ELM can be expressed as

$$\Delta W_{\mathrm{ELM}} = (3k_B \langle n_{ped} \rangle \Delta T_{ped,\mathrm{ELM}}$$

$$+ 3k_B \langle T_{ped} \rangle \Delta n_{ped,\mathrm{ELM}}) V_{\mathrm{ELM}} \ , \qquad (3)$$

where V_{ELM} is the volume of plasma affected by the ELM, n_{ped} and T_{ped} are the plasma density and temperature (in units of energy, as usual in fusion physics) at the pedestal, and $\Delta T_{ped,\mathrm{ELM}}$ and $\Delta n_{ped,\mathrm{ELM}}$ are the temperature (in units of energy, as usual in fusion physics) and density drops at the pedestal caused by the ELMs. The decrease of plasma energy by ELMs is, thus, the result of two loss mechanisms: conductive losses (related to the decrease of $\Delta T_{ped,\mathrm{ELM}}$) and convective losses (related to the decrease of $\Delta n_{ped,\mathrm{ELM}}$). Normalizing ΔW_{ELM} to the pedestal plasma energy leads to the expression

$$\frac{\Delta W_{\mathrm{ELM}}}{W_{ped}} = \left(\frac{\Delta T_{ped,\mathrm{ELM}}}{\langle T_{ped} \rangle} + \frac{\Delta n_{ped,\mathrm{ELM}}}{\langle n_{ped} \rangle} \right) \frac{V_{\mathrm{ELM}}}{V_{plasma}} \ . \qquad (4)$$

A quantitative comparison among the parameters on both sides of Eqs. (3) and (4) requires measurements of density and temperature profiles with high spatial (and ideally in both the poloidal and radial directions) and time resolution. This allows the evaluation of the average values of density and temperature in the ELM-affected volume and their changes by ELMs, which are not available in JET. However, an estimation of the relative contribution of convection and conduction to the total ELM energy loss can be obtained by evaluating the ELM-affected volume from the electron temperature profile (measured by an ECE radiometer) before and after the ELM and by measurements of the relative changes of the electron temperature at the top of the pedestal during the ELM (measured by an ECE radiometer) and of the electron pedestal density (measured by an interferometer line crossing the pedestal region), as shown in Figs. 42 and 43, respectively.[150] The changes in the electron temperature profile (in Fig. 42a) show that the volume of plasma that ELMs affect at JET corresponds typically to the outer 20% of the plasma radius. The plasma volume affected by ELMs depends on the magnetic configuration of the discharge (smaller for high-triangularity conditions) but is weakly dependent on pedestal plasma density or collisionality for type I ELMy H-modes in JET (see Ref. 159 and Fig. 42b). Normalizing the ELM perturbation of the electron temperature profile to the value of the pedestal temperature before the ELM ($T_{e,ped}$), as shown in Fig. 42b, demonstrates that the volume of plasma affected by the type I ELMs remains unchanged even when the ELM energy loss changes by a factor of ~3 when the pedestal plasma density/collisionality is increased in a gas scan. A noticeable change of the ELM-affected plasma volume takes place only when the ELM regime changes from type I to type III at the highest fueling rates. This observation is not consistent with the simple picture of the ELM losses being caused by a shrinking of the ELM-affected area with increasing plasma

(a)

(b)
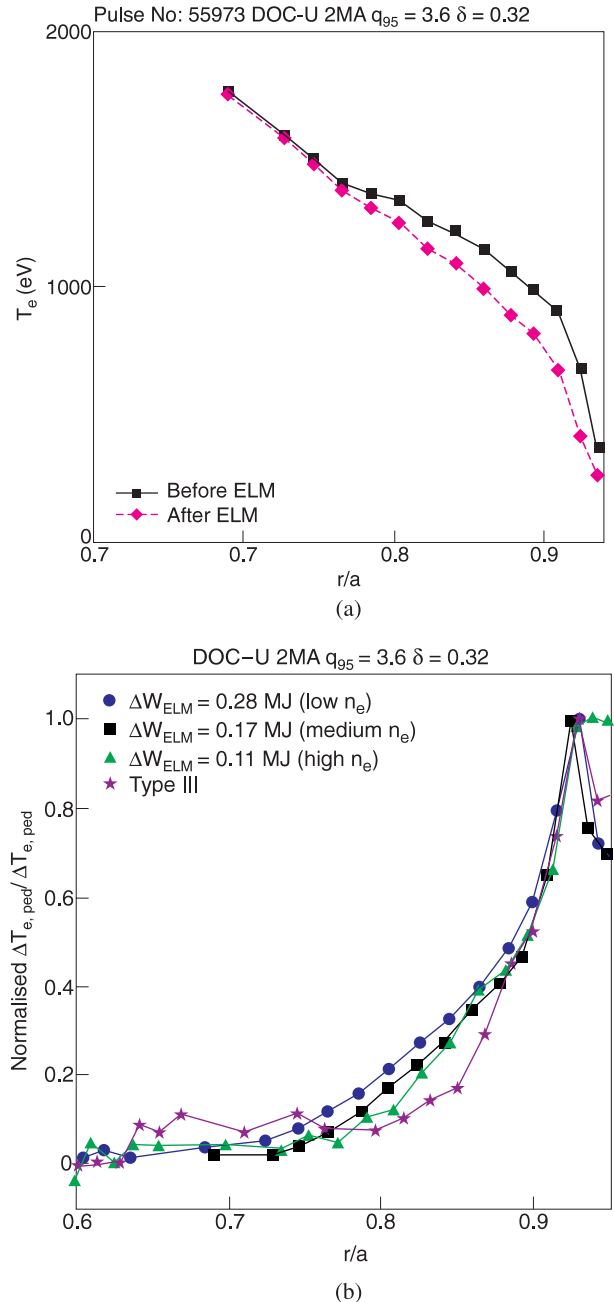
Fig. 42. (a) Measurements of the plasma electron temperature by ECE before and after an ELM. (b) Normalized electron temperature perturbation caused by the ELMs versus normalized radius for three type I ELMy H-modes and one type III ELMy H-mode, showing that the perturbation changes shape only when the ELM type changes and not with decreasing type I ELM size. (From Ref. 150.)

collisionality, which is expected from the narrower eigenmode of the ELM trigger at higher collisionalities, as discussed in Sec. VI. On the other hand, the normalized changes of pedestal density and temperature shown in

Fig. 43. Normalized ELM temperature and density drop in JET type I and type III ELMs versus pedestal plasma collisionality, showing the large decrease of the temperature drop with increasing collisionality. (From Ref. 150.)

Fig. 43 demonstrate that with increasing pedestal density/ collisionality, the magnitude of the normalized ELM perturbation to pedestal density and temperature decreases. The magnitude of this decrease, however, is very different for density and temperature, and although 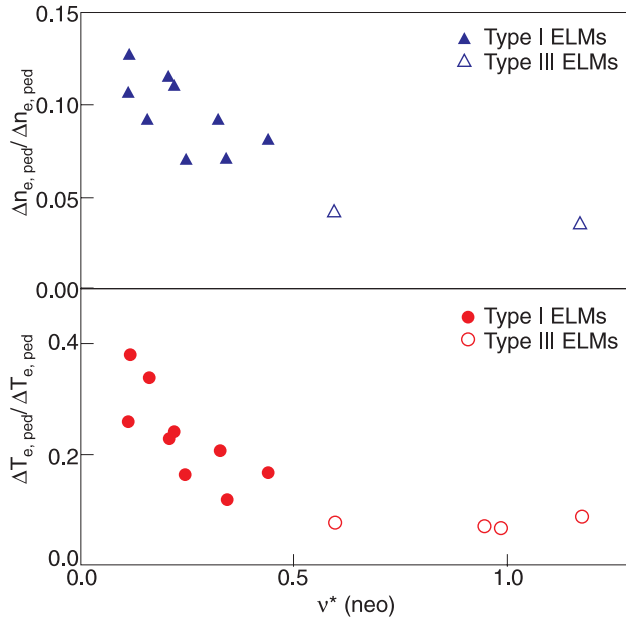the pedestal density perturbation decreases by a factor of 1.3 to 1.8 within the range of collisionalities accessible for type I ELMy H-modes for these conditions, the normalized ELM temperature perturbation decreases by a factor of 1.6 to 3.2. Thus, the decrease of $\Delta W_{\mathrm{ELM}}/W_{ped}$ with increasing plasma density/collisionality in this scan is mainly due to the decrease of $\Delta T_{e,\mathrm{ELM}}/\langle T_{ped}\rangle$, i.e., the reduction of ELM conductive losses, highlighting the fact that transport mechanisms (probably related to the nonlinear MHD phase of the ELM) play an important role in determining the magnitude of the ELM energy loss. It is also important to note that the transition from type I to type III is accompanied by a marked decrease (by a factor of 1.5 to 2.0) of both $\Delta T_{ped,\mathrm{ELM}}/T_{ped}$ and $\Delta n_{ped,\mathrm{ELM}}/n_{ped}$, as well as the reduction of ELM-affected plasma volume shown in Fig. 42b. Other factors that can affect the decrease of $\Delta W_{\mathrm{ELM}}/W_{ped}$ with collisionality are the change of T_i in the pedestal region during ELMs, usually not measured (assumed to be similar to T_e) and differences in the behavior of electron temperature and density in the pedestal region in terms of both time evolution and ELM-affected volume. Given the lack of sufficient measurements to compare profile and global measurements of the change of plasma particle content and energy during ELMs, edge

plasma models have been applied to simulate the available experimental data by assuming that ELMs lead to a large increase of edge plasma transport during a short period of time, which has produced a reasonable match to the measurements of ELM characteristics available at JET (Ref. 167).

Further analysis of ELM measurements from JET experiments, besides the collisionality scans described so far, has shown that the dominance of ELM conductive losses in the determination of the total ELM energy loss and its change with pedestal plasma conditions is an intrinsic feature of type I ELMs (Refs. 133, 150, 168, and 169). Indeed, the direct correlation between $\Delta W_{\mathrm{ped,ELM}}/W_{ped}$ and $\Delta T_{ped,\mathrm{ELM}}/T_{ped}$ is seen to be valid not only for JET experiments in which the ELM losses are seen to deviate from the collisionality scaling in Fig. 45, which will be described in detail below, but also more generally to results from other divertor experiments,[168,169] as shown in Fig. 44. Thus, the access to small ELMs (i.e., $\Delta W_{ped,\mathrm{ELM}}/W_{ped} < 0.05$) and high confinement, as required for ITER, is directly linked with the achievement of type I ELMs with $\Delta T_{ped,\mathrm{ELM}}/T_{ped} < 0.1$ in these conditions. Given the small perturbation caused to the plasma temperature by such ELMs, they are called "type I convective ELMs" at JET (Ref. 150).

As mentioned, the flexibility of JET to operate in a large range of plasma current, toroidal field, plasma shaping, and toroidal field direction has been instrumental in identifying the key parameters and physics mechanisms that determine the magnitude of the ELM energy and particle losses and their dependence on pedestal plasma parameters (in particular, pedestal collisionality). But beyond this, this flexibility has allowed the identification of plasma conditions that deviate from the collisionality scaling shown in Fig. 41 and so has opened a new line of research. This should eventually lead to the development of a complete physics picture for the processes that determine the loss of energy by ELMs, which would allow its prediction for ITER to be made on a firmer physics base than from the empirical scaling in Fig. 41. Experiments at JET have demonstrated that type I ELMy H-mode discharges with $\Delta W_{\mathrm{ELM}}/W_{ped} \sim 0.05$ can indeed be obtained for pedestal collisionalities similar to those expected in ITER, as shown in Fig. 45 (Refs. 168 and 169). This figure shows more recent measurements of ELM losses at JET superimposed with the previous database from Fig. 41 (in grey). The low-collisionality convective type I ELMs have been achieved at JET in two regimes, discharges with high triangularity ($\delta > 0.4$) and high q_{95} ($q_{95} > 4.2$ to 4.5; Ref. 150) and discharges with medium triangularity ($\delta \sim 0.25$ to 0.3 and $q_{95} = 3.6$) and reversed toroidal field direction (i.e., ion ∇B direction away from the X-point; Ref. 133). Apart from the small ELM energy loss, these ELMs behave like and have overall characteristics similar to those of other type I ELMs, such as in the relation between $\Delta W_{\mathrm{ELM}}/W_{ped}$ and
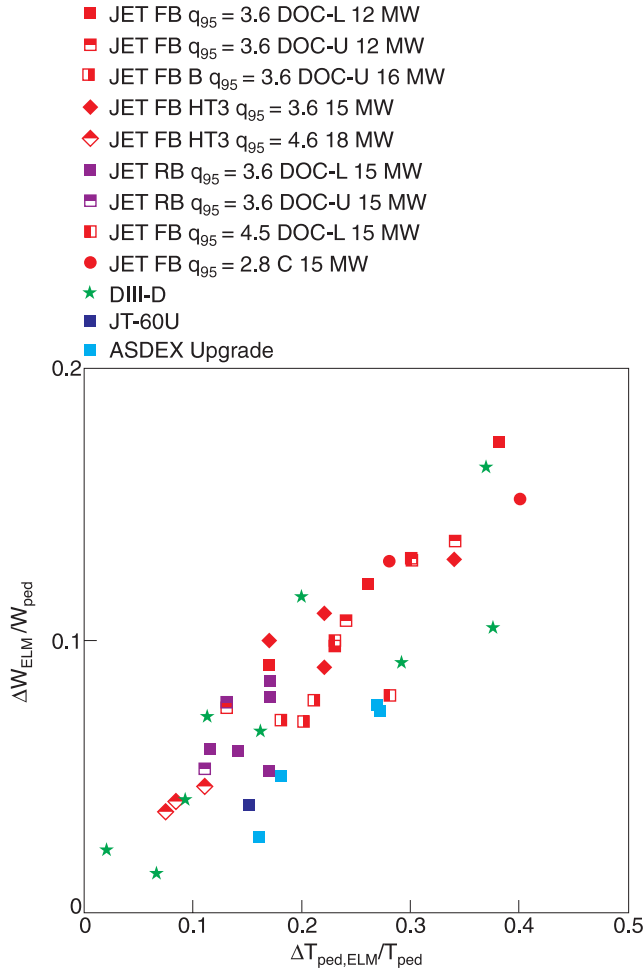
Fig. 44. Normalized ELM energy drop versus normalized ELM temperature drop for a range of JET (low/high triangularity, q_{95} = 2.8 to 4.5, and forward and reversed field), DIII-D, JT-60U, and ASDEX-Upgrade type I ELMy H-modes, showing the correlation between small ELM energy losses and convective ELMs (small temperature drop). (From Refs. 168 and 169.)

Fig. 45. Normalized ELM energy loss ($\Delta W_{\mathrm{ELM}}/W_{ped}$) versus pedestal collisionality (ν^*) for type I ELMy H-mode plasmas (gray online) in Fig. 41 and later newer results from JET. The JET data include a range of I_p plasma shapes and q_{95} and two directions of B_ϕ. Low-ν^* convective ELMs for JET are shown in red online. (From Ref. 168.)

$\Delta T_{ped,\mathrm{ELM}}/T_{ped}$, already mentioned in the discussion of Fig. 44 and in the ELM-affected volume, as shown in Fig. 46 (Refs. 133 and 150) for low-collisionality convective type I ELMs in the two regimes described. It is important to note that the main plasma conditions for which these low-collisionality convective type I ELMs are obtained are not compatible with the requirements for Q_{DT} =10 operation in ITER (Refs. 151 and 153). For the high-δ discharges, the required $q_{95} \sim 4.5$ would correspond to a $Q_{DT} \sim 3$ in ITER, if assumptions regarding the normalized energy confinement and operating density similar to those for the $Q_{DT} = 10/q_{95} \sim 3.0$ regime are used (namely, $H_{98(y,2)} = 1$ and $\langle n_e \rangle/n_{\mathrm{Gr}} = 0.85$; Ref. 138). However, scenarios similar to these may be suited to the ITER hybrid scenario (see Chap. 4
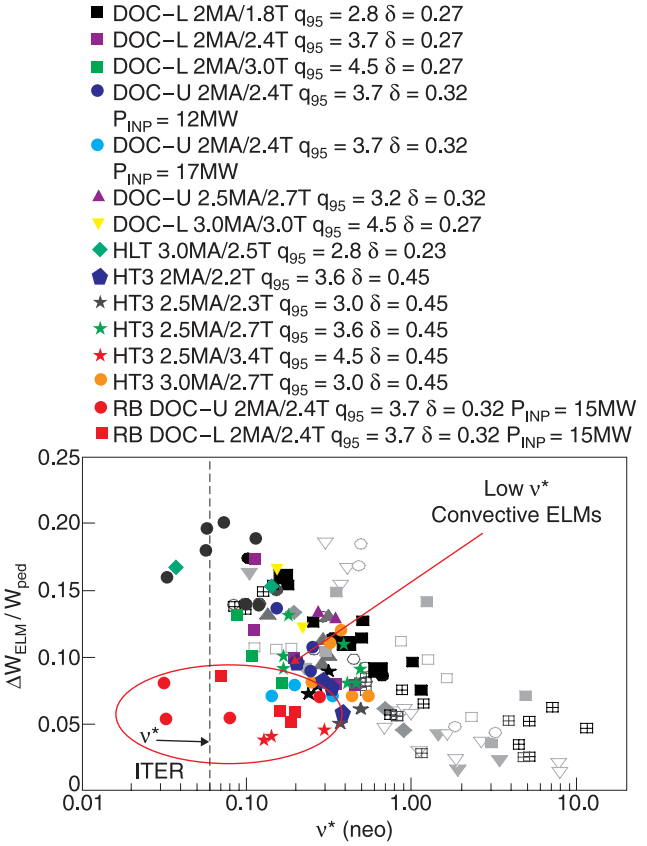
of this issue[76]). For the reversed field discharges at medium δ, the maximum plasma density reached in type I ELMy H-mode is only $\langle n_e \rangle/n_{\mathrm{Gr}} = 0.70$, at which value the energy confinement has already deteriorated to $H_{98(y,2)} \sim 0.8$ (Ref. 133). If a similar normalized confinement and density were observed on ITER, this would lead to a predicted plasma performance similar to those of the high-δ/high-q_{95} discharges above. Despite this incompatibility with the required performance in ITER, which prevents the direct extrapolation of these regimes to ITER, these JET results are very important for understanding ELM physics. The access to low-collisionality type I ELMs at JET has demonstrated that although collisionality is a parameter that influences the ELM energy loss for a large range of conditions, it is not the only parameter that controls it and will determine it eventually in ITER. It remains to be understood which pedestal characteristics are different in the low-collisionality convective type I ELMy H-mode regimes at JET (mainly because of the difficulties in the pedestal gradient
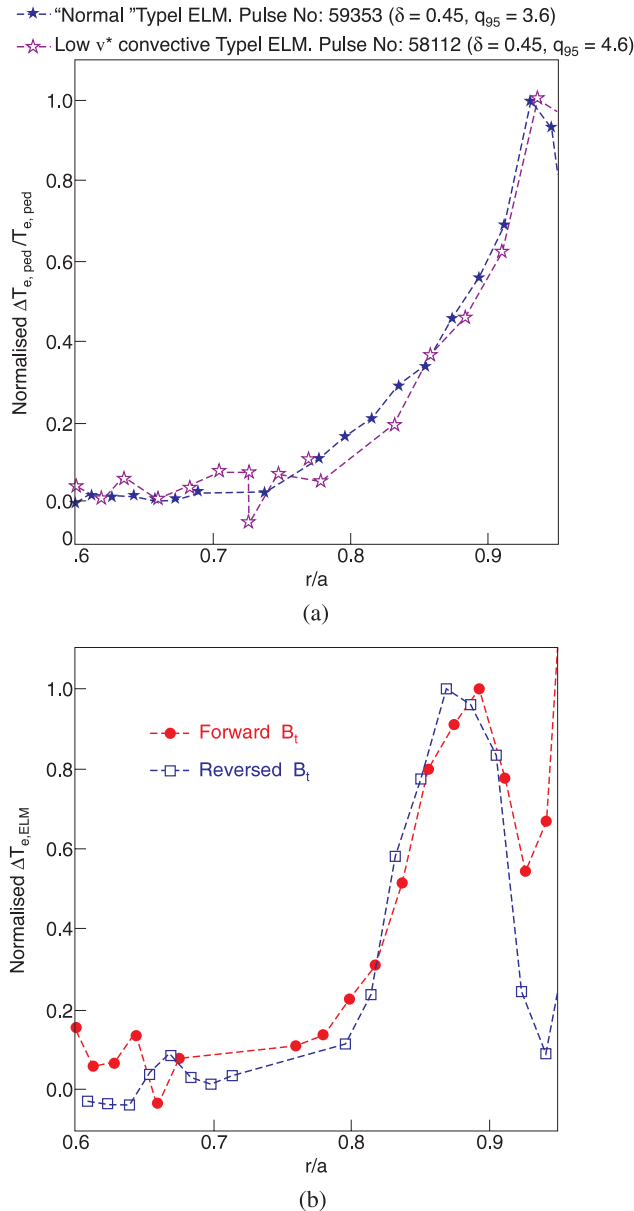
Fig. 46. (a) Normalized electron temperature perturbation caused by the ELMs versus normalized radius for a "normal" type I ELM in a high-δ type I ELMy H-mode compared to that of a low-collisionality type I ELM in a high-δ/q_{95} type I ELMy H-mode. (b) Normalized electron temperature perturbation caused by the ELMs versus normalized radius for a "normal" type I ELM in a medium δ type I ELMy H-mode with forward toroidal field compared to that of a low-collisionality type I ELM in a medium-δ type I ELMy H-mode with reversed toroidal field. (From Ref. 133.)

diagnostics) and whether these will be similar in ITER. This will determine whether such ELMs will be accessible in ITER for the required plasma densities and energy confinement for $Q_{DT} = 10$ operation in this device.

Finally, it is important to note that even for steady-state global plasma conditions, there is a significant ELM-to-ELM variability in some of the changes associated with ELMs. This is true not only for JET experiments but also in all other devices. Characterizing and understanding the reasons behind this variability have very important implications for the determination of the compatibility of ELM loads with divertor lifetime in ITER. So far, only JET experimental results have been analyzed in this respect for a series of type I ELMy H-mode experiments covering a wide range of plasma current ($I_p = 1$ to 3 MA), triangularities ($\delta = 0.25$ to 0.45), and fueling rates (0 to 7×10^{22} s^{-1}), as shown in Fig. 47 (Ref. 150). From the histograms in Fig. 47, it is clear that although the triggering of ELMs occurs at very reproducible values of the pedestal density and temperature for steady-state global plasma conditions (plasma shape, input power, and fueling rate), the changes induced in them (and the associated ELM energy loss) are much more variable. On the basis of this analysis, it can be concluded that in order to guarantee that 95% of the ELMs cause an energy loss smaller than a given value ΔW_{ELM}^{max} (maximum value compatible with an acceptable divertor target lifetime in ITER), the average ELM energy loss for steady-state conditions should fulfill the condition

$$\langle \Delta W_{ELM} \rangle \leq 0.67 \Delta W_{ELM}^{max} \ . \tag{5}$$

This condition imposes severe restrictions on the maximum size of the average ELM load in ITER, which would then be restricted to $\langle \Delta W_{ELM} \rangle_{allow\text{-}ITER} < 2.7$ MJ (2.5 to 3.0% of W_{ped}), even assuming ideal material behavior[152] and symmetry of the ELM power fluxes at the divertor.

V.C. ELM Power and Particle Fluxes to PFCs in Type I ELMy H-Modes

V.C.1. Plasma Interaction with the Divertor Target During Type I ELMs

The initial observations of ELM interaction with the divertor target at JET already identified some of the critical physics involved in this process. The interaction of the plasma with the divertor, as measured with Langmuir probes, was found to start with a sudden change of the measured plasma temperature and floating voltages, which was then followed by the increase of the ion flux to the target few 100 μs later,[155,170] as illustrated with the data from more recent experiments in Fig. 48 (Ref. 171; $t = 0$ is the reference time for the coherent average of the measurements for various ELMs as determined by the maximum ion saturation current during the ELM). This showed for the first time that different timescales are involved in the flow of electrons and ions to the divertor during ELMs. In fact, it was observed that during the ELMs, hot electrons with energies similar to those of the pedestal plasma impact on the divertor target for a few 100 μs, producing an intense X-ray emission by bremsstrahlung as they
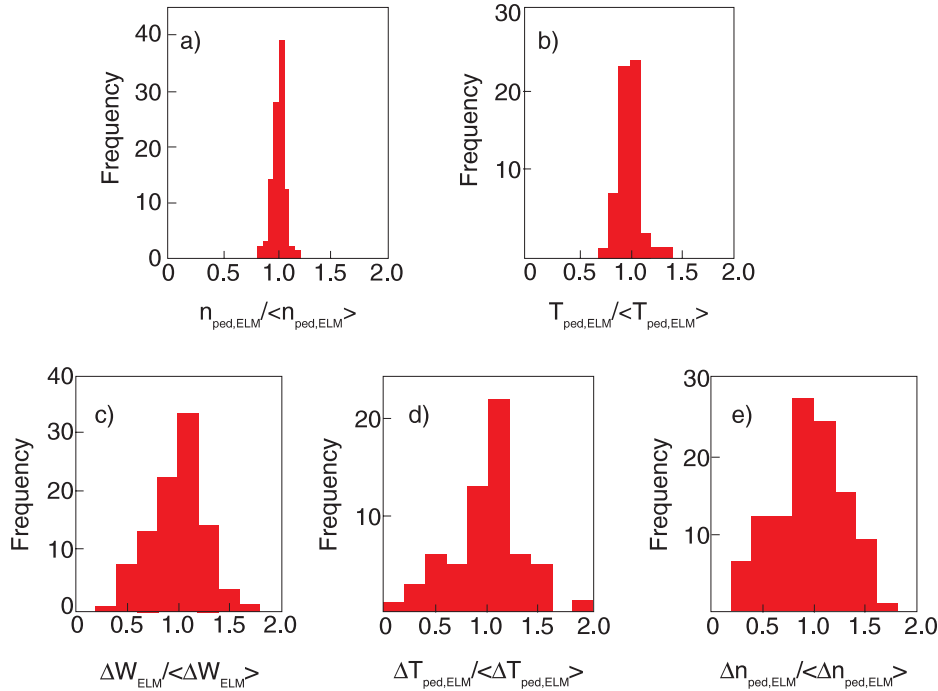
Fig. 47. Histograms for ELM-related parameters for a series of type I ELMs in JET experiments covering a wide range of plasma current ($I_p = 1$ to 3 MA), triangularities ($\delta = 0.25$ to 0.45), and fueling rates (0 to 7×10^{22} s^{-1}): (a) Pedestal density before the ELM, (b) pedestal temperature before the ELM, (c) ELM energy loss, (d) ELM pedestal temperature drop, and (e) ELM pedestal density drop. Note the narrow width of the histograms in (a) and (b) compared to those in (c) through (e). (From Ref. 159.)

decelerate into the divertor target, as shown in Fig. 49 (Ref. 172). The duration of the power flux to the divertor, as determined by the rise time of the surface temperature of the divertor target, was 100 μs or shorter.[157] Significant deviations could be found between the locations for power deposition between ELMs and those at the ELMs (Refs. 155 and 170), indicating that the strike point could shift significantly during ELMs. Some of these observations were indeed seminal and have later been explored in detail with improved diagnostics at JET. This has allowed the development of a reasonably mature (although not yet fully complete) understanding of the energy and particle fluxes to PFCs, for which the experimental results from JET have been crucial. Other of these initial observations, such as the short ELM power deposition duration and the large movement of the strike points during ELMs, are not general for all type I ELMs at JET but are associated with the regime of large-ΔW_{ELM}, high-I_p (typically >3.5 MA), low-pedestal collisionality for which the measurements were obtained. Further detailed exploration of the strike point movement behavior during ELMs indicates that it is correlated with the changes in the edge current associated with large ELMs, which leads to a change in the plasma equilibrium during this phase.[173]

Detailed studies of power and particle fluxes during ELMs were carried out in JET starting with the MkIIGB

divertor and continued in all its subvariants with improved diagnostics and in a wider operation space than that described for the MkI and MkIIA divertors. Analysis of these measurements revealed that the deposition of ELM energy at the divertor takes place in timescales correlated with the transport of particles (ions) from the pedestal to the divertor target, whereas the ELM electron energy flux is correlated with the duration of the ELM MHD event, as shown in Figs. 50 and 51 (Refs. 150 and 174). This is consistent with kinetic modeling of ELM energy fluxes during ELMs (Refs. 175, 176, and 177). The separation between electron and ion fluxes, which is key to understanding the physics of ELM power fluxes in the kinetic picture, has been experimentally demonstrated for the first time at JET by comparing measurements of ion fluxes with Langmuir probes and D_α emission from the divertor and of electron fluxes from soft X-ray emission.[159] Although the increase of both ion and electron fluxes caused by the ELM is simultaneous at low plasma densities (corresponding to short ion transit times $\tau_\parallel^{ELM}$), these are well separated at high densities (long $\tau_\parallel^{ELM}$), particularly at the inner divertor,[150] as shown in Fig. 52a. A delay between the arrival of the ion flux to the inner divertor and the electron flux was identified for the first time at JET (Ref. 159) and is of magnitude similar to the delay between the arrival of the ion
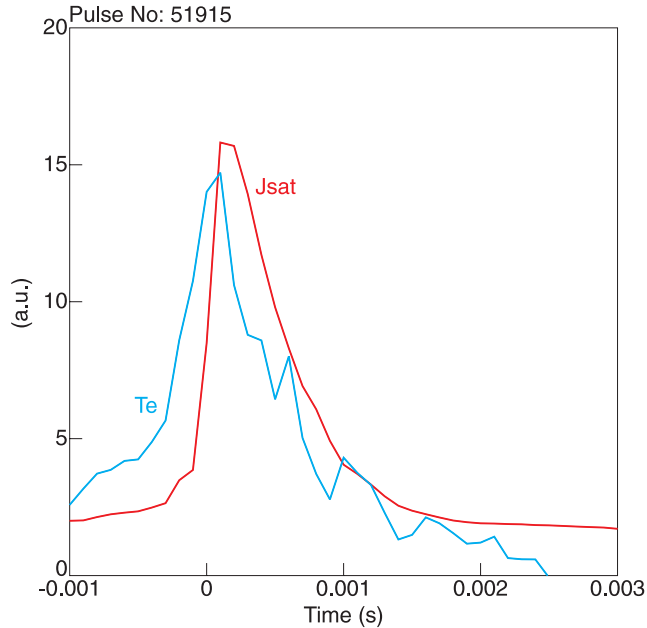
Fig. 48. Measurements of plasma parameters at the divertor target during a type I ELM with Langmuir probes at JET: Ion saturation current and electron temperature of average ELM versus time ($t = 0$ is taken as a reference by the time of maximum ion saturation current during the ELM). It is important to note that the electron temperature increases before the ion saturation current reaches its maximum during the ELM pulse. (From Ref. 171.)
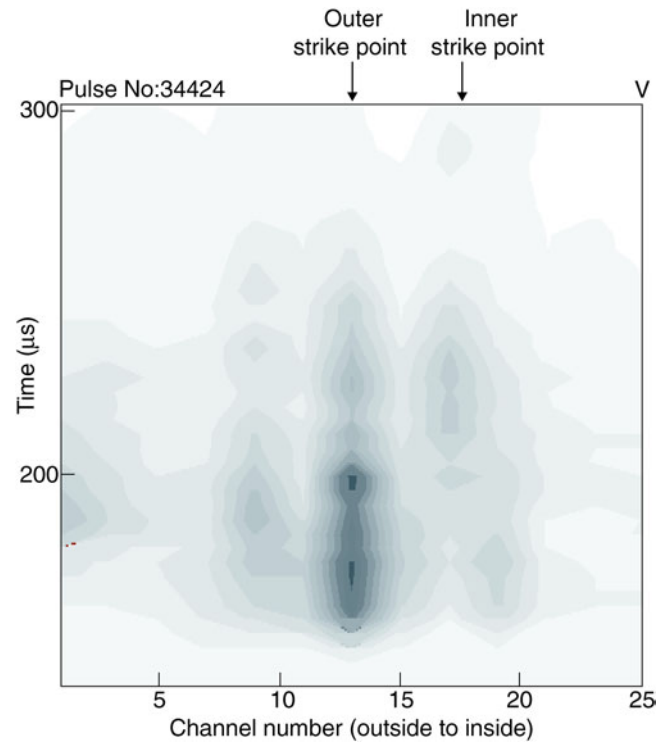

Fig. 49. Contour plots of X-ray intensities observed by a camera looking at the JET divertor target from the top. The data show the changes of this emission from the JET divertor target area during the ELM since the emission profiles just before the ELM have been subtracted. (From Ref. 172.)

flux between the outer and inner divertors. This time delay between the ion flux at both divertors is found to scale with the ion transit time $\tau_\parallel^{\mathrm{ELM}}$ (as shown in Fig. 52b). This later was found in ASDEX Upgrade experiments[178] and other tokamaks as well.[20] The existence of this divertor ion flux in-out delay and its scaling with the scrape-off layer (SOL) ion transit time itself is consistent with the above kinetic picture and with the origin of the ELMs being located in the outboard side of the plasma, which is consistent with evidence from other tokamaks[179] and JET itself.[180]

Other more quantitative results of models developed to describe the flux of energy to the divertor and main wall during ELMs (Ref. 181) and more sophisticated kinetic modeling results of power fluxes during ELMs at JET (Refs. 175, 176, and 177) have been compared in detail with experimental data from JET. This is the first time in which a quantitative comparison of modeling predictions for ELM divertor power fluxes has been attempted. Measurements of the time evolution of the divertor ELM power flux with infrared cameras show that only a small fraction (typically less that 30%) of the total energy deposited at the divertor by the ELMs actually reaches the divertor within the rise phase of the power flux at the divertor (which is taken to characterize the

ELM power flux duration; see Fig. 50), as shown in Fig. 53 (Refs. 150 and 174). This is in excellent agreement with results from the model in Ref. 181 and kinetic modeling of ELM fluxes for JET (Refs. 175, 176, and 177). The temporal waveform for the divertor ELM power flux derived from this model is[181]

$$q_{div,\mathrm{ELM}}(t) = q_{div,\mathrm{ELM}}^{\max} \left[1 + \left(\frac{\tau}{t} \right)^2 \right] \left(\frac{\tau}{t} \right)^2 \exp \left[- \left(\frac{\tau}{t} \right)^2 \right] .$$

(6)

This temporal waveform for the divertor ELM power flux is in excellent agreement with experimental measurements not only from JET but also from ASDEX Upgrade,[182] as shown in Fig. 54.

Infrared measurements of divertor ELM power fluxes obtained at JET (Refs. 174 and 183) for a large range of plasma conditions in the type I ELMy H-mode[150] have provided a unique and key contribution to the understanding of the role of energy transport across and along the field onto PFCs during ELMs. These JET measurements have demonstrated that a significant part of the energy
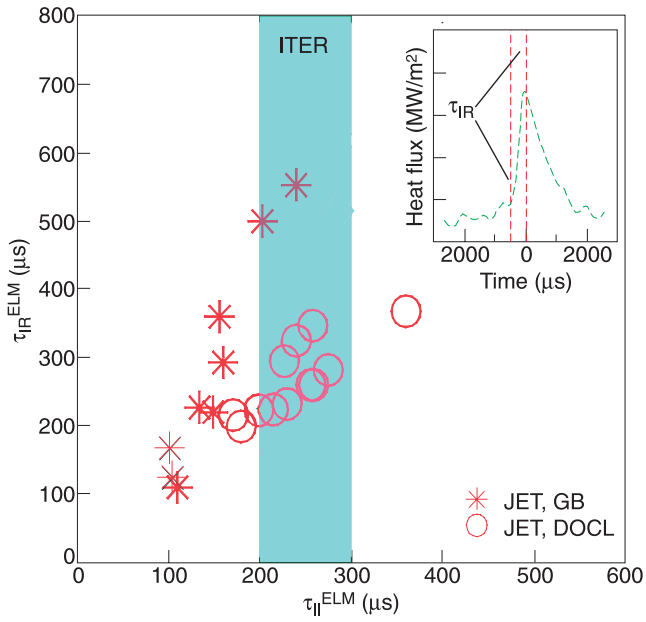
Fig. 50. Characteristic timescale of the type I ELM divertor power deposition rise τ_{IR} on the (outer) divertor target (definition shown in insert, in which $t = 0$ is taken as a reference by the time of maximum power flow during the ELM) versus SOL ion time, $\tau_{\parallel}^{ELM}$ ($= L/c_s$) calculated with pre-ELM pedestal plasma temperature covering a range of JET experiments including $I_p = 1.2$ to 3 MA and various fueling levels. (From Ref. 174.)

(a)

(b)
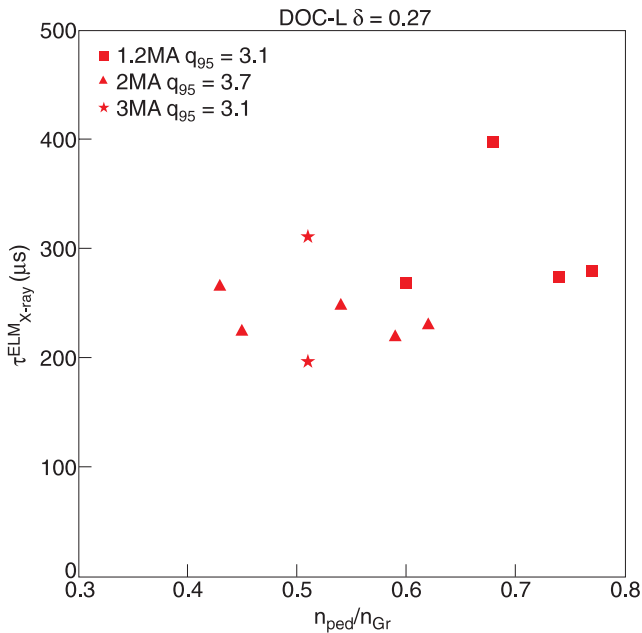
Fig. 51. Duration of the electron flux pulse at the JET divertor determined by soft X-ray emission for a large range of JET type I ELMy H-mode plasmas. (From Ref. 150.)
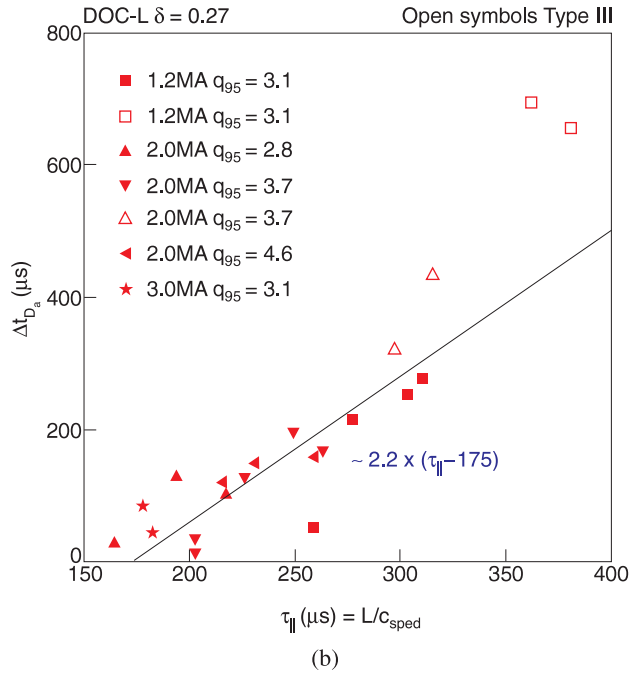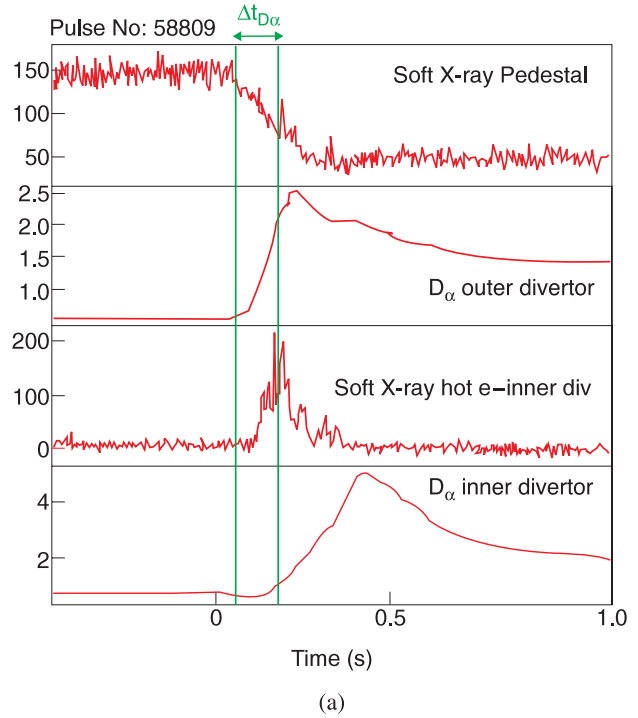
Fig. 52. (a) Measurements with high time resolution ($\sim 4\ \mu s$) of the soft X-ray emission pedestal collapse, outer divertor D_α emission, inner divertor X-ray bremsstrahlung (from hot electron impact), and inner divertor D_α emission during a type I ELM in JET, showing the delay between the rise of the D_α emission at both divertors ($\Delta t_{D\alpha}$). (b) Delay of the D_α rise at the inner divertor with respect to the outer one versus parallel ion transit time calculated with pedestal plasma parameters for a large range of H-modes in JET. (From Ref. 150.)
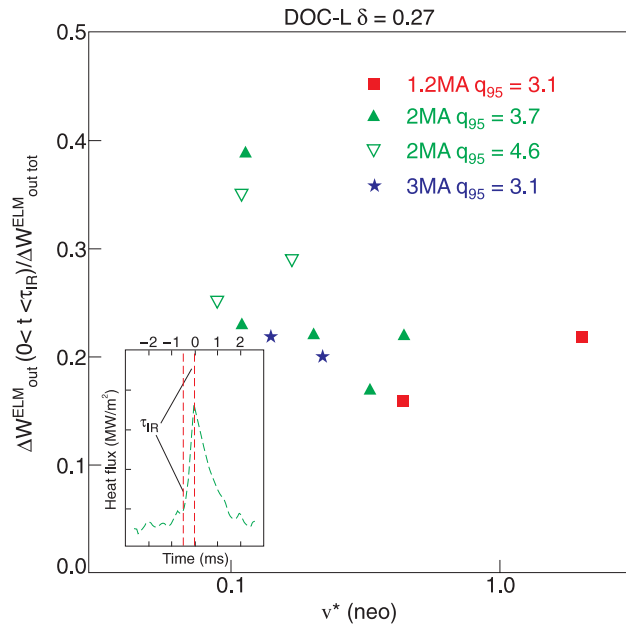
Fig. 53. Proportion of the ELM energy arriving at the divertor in the time interval $[0, \tau_{IR}]$ (i.e., ELM start to the time of maximum power flux, as shown in the inset) with respect to the total ELM divertor energy versus pedestal collisionality for a range of type I ELMy H-modes at JET. (From Refs. 150 and 174.)
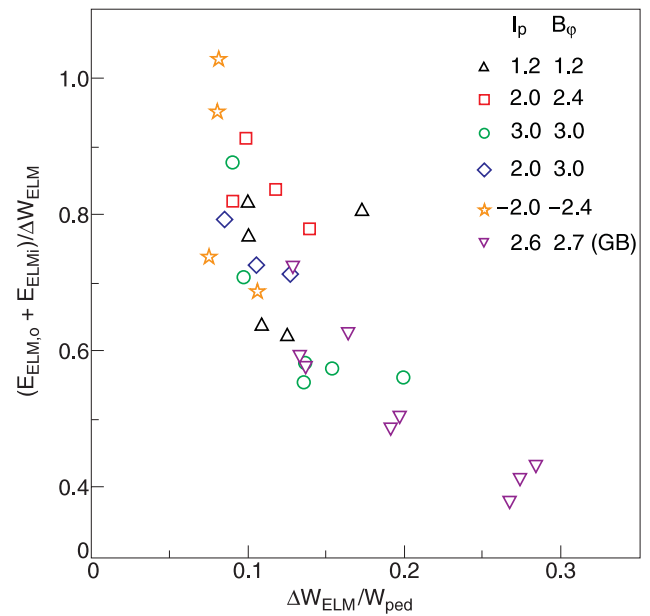
Fig. 55. Proportion of the ELM energy arriving at the divertor with respect to the ELM energy lost from the main plasma ELM energy loss (normalized to the pedestal plasma energy) for a range of type I ELMy H-modes at JET. (From Refs. 174, 175, and 183.)
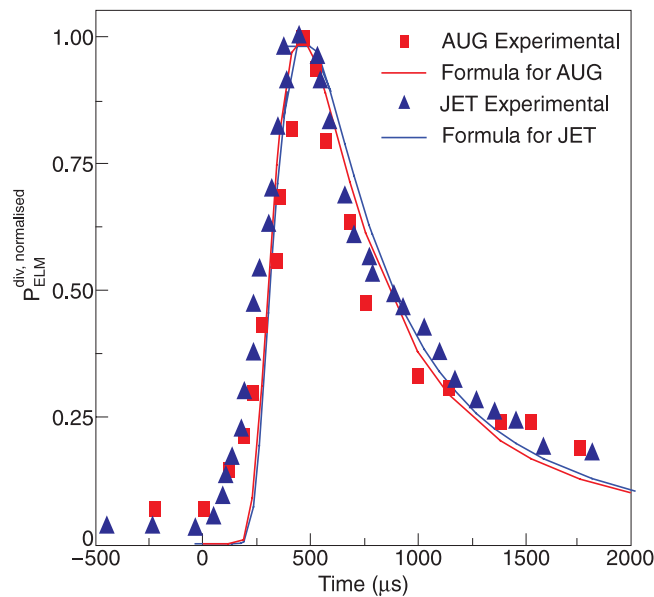
Fig. 54. Time evolution of the ELM power flux to the divertor target as measured by infrared cameras for type I ELMs at JET and ASDEX Upgrade (symbols) versus results from Eq. (6) (lines). (From Ref. 182.)

lost by the main plasma during ELMs does not reach the divertor target. In fact, the proportion of ELM energy reaching the divertor target decreases with increasing ELM energy loss, as shown in Fig. 55 (Refs. 174, 175, and 183), indicating that larger ELMs lead to larger energy deposition outside the divertor target. This has been confirmed by a series of dedicated experiments and measurements and has led to the development of a model[181] that can successfully describe many of the experimental findings in the JET experiments, which are described below.

V.C.2. Plasma Interaction with the Main Wall During Type I ELMs

The first evidence for strong interaction of the plasma with the main wall at JET was determined by soft X-ray measurements[172] during experiments with the MkI divertor. Contrary to the observations of soft X-ray emission of electrons impacting the divertor target discussed previously and shown in Figs. 49 and 52, soft X-ray emission measurements during ELMs in the main chamber showed that this emission had not originated from the direct impact of electrons on the main chamber PFCs. The soft X-ray emission had originated inside the confined plasma and was poloidally localized near the PFCs closest to the plasma separatrix (poloidal limiters), as shown in Fig. 56. This X-ray emission was associated

Fig. 56. Tomographic reconstruction of background-subtracted X-ray signals near the upper tip of the outer limiter during a type I ELM at JET. The region of intense emission from within the plasma stands out clearly. (From Ref. 172.)

Fig. 57. Measurements of the ion flux (j_{sat}), electron temperature (T_e), and radial propagation velocity for ELM filaments generated in a JET type I ELMy H-mode (I_p = 2.0 MA and B_T = 2.45 T with NBI additional heating P_{NBI} = 13 MW). The filaments were measured at a distance of 4 cm from the separatrix (mapped to the outer midplane). (From Ref. 185.)

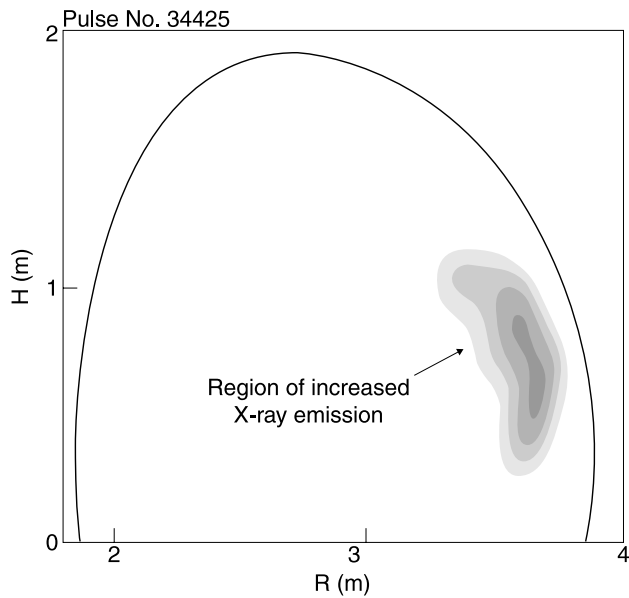with the ionization of deuterons with $\sim$ keV energies, which were assumed to originate from the neutralization of ions with energies similar to those of the pedestal plasma that would recycle locally at the limiter during the ELM event.[172] More detailed analysis of the emission pattern in visible light produced by the interaction of ELM with main chamber PFCs at JET revealed that this interaction is concentrated on the low-field side of the chamber and localized poloidally in regions that correspond to the interaction of a plasma that balloons out, with a toroidal mode number of $n = 12$ and a poloidal mode number of $m = 50$ (Ref. 180), which is similar to expectations for the ballooning-peeling model for the linear phase of ELMs (Ref. 164).

Improved diagnostics and more systematic experiments have confirmed in detail these initial observations. Measurements of radial plasma fluxes during ELMs with Langmuir probes and retarding field analyzers have shown that these fluxes are produced by filamentary structures that rotate toroidally/poloidally as they propagate across the SOL, with typical radial velocities of 400 to 2000 m/s (Refs. 184 and 185), in qualitative agreement with observations from other devices.[186] As these plasma filaments propagate radially, they lose energy along the field lines to the divertor target. A model has been developed at JET to describe this process, one of whose main predictions is that the dominant component of the radial energy flux during the ELM is the convection of ion energy[181]; this is caused by the larger efficiency for electrons to lose their energy by transport along the field

line. The key, and to date one of the few (if not the only) existing experimental demonstration of this physics picture, was obtained at JET by measurements of Langmuir probes[185] and retarding field analyzers[187] in the SOL, as shown in Figs. 57 and 58. Measurements with Langmuir probes during ELMs demonstrate that the SOL electron temperature (measured 3 to 5 cm from the separatrix, mapped to the midplane) is typically several tens of eV (Fig. 57). This is a factor of 10 to 20 times lower than the pedestal plasma temperature for the discharges in which these measurements were taken, demonstrating that the electrons in the plasma expelled by ELMs cool dramatically as they travel across the SOL. The pedestal plasma temperature is taken as representative of the temperature of the plasma expelled by ELMs on the basis of the ECE observations described in Sec. V.B.2 and the soft X-ray measurements described in Sec. V.C.1. On the other hand, measurements with a retarding field analyzer indicate that there is a significant flux of ions with energies of 400 eV and larger, even at distances of $\sim$4 to 5 cm from the separatrix (mapped to the midplane), for type I ELMy H-modes whose pedestal ion and electron temperatures are $\sim$400 eV (Ref. 188), as shown in Fig. 58. This demonstrates that ions with energies typical of the pedestal plasma can reach the main wall PFCs, thus explaining the deficit of divertor ELM energy discussed in Sec. V.C.1. In fact, the measurements with the retarding field analyzer

Fig. 58. Measurements of the ion flux (j_{sat}) reaching a retarding field analyzer and the ion current measured for ions that are able to overcome a retarding potential of 400 V during a type I ELM at JET (j_{coll}). The gray shaded areas correspond to the values predicted by the ELM transport model in Ref. 181 for these experimental conditions. (From Ref. 187.)

have been compared in detail with the predictions of the model in Ref. 181, and it was found that the model is able to reproduce the total ion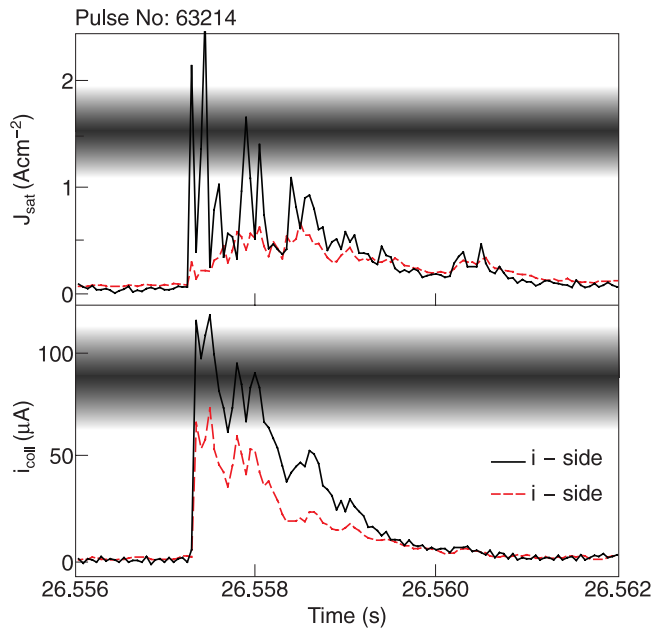 flux and the flux of ions with energies larger than the applied retarding voltage of 400 eV with assumptions that are compatible with experimental measurements at JET (Ref. 187). The model predictions are shown as gray bands in Fig. 58.

The major outstanding issues for a complete understanding of the dynamics of plasma energy flow during ELMs concern the formation and movement of the plasma in the filaments created by the ELMs and how they are related with main properties of the pedestal plasma and the ELMs themselves (total ELM energy loss, convective/conductive nature of the ELMs, characteristics of the ELM trigger, etc.). While the research in this field is ongoing, JET experiments have already provided measurements of the radial propagation velocity, which are in the range of several $100 \, \text{ms}^{-1}$ to several kms^{-1} (Refs. 184, 185, and 188), and proposed scalings of this velocity with ELM energy loss, which can be used to reproduce the deficit of the ELM energy at the divertor target.[187,189] Detailed analysis of experimental measurements obtained in the last operation period and new experiments in the near future will certainly shed more light on this issue of key importance for ITER.

Despite these remaining outstanding issues, the state of validation of the models developed at JET is sufficient

for their application to the evaluation of the expected ELM fluxes to divertor target and main wall components in ITER. This initial application along these lines has been carried out in Ref. 168 by taking into account the key results from the models developed at JET (Refs. 175, 176, 177, 181, and 187).

V.D. Summary and Conclusions

The JET data have been instrumental in establishing the empirical correlation between ELM energy loss and pedestal collisionality as well as establishing the dominance of conductive losses in determining the total ELM energy loss. This is particularly important since JET is the only existing device that has the capability of accessing pedestal collisionalities in the range of those expected in ITER in the type I ELMy H-mode, with values of the pedestal densities and temperatures similar to those expected in ITER, which can have a deep influence on edge ionization, plasma resistivity, and the like expected to play a role on the ELM behavior. Similarly, the experiments at JET identified for the first time in a systematic way which operating conditions allow the breaking of the correlation of $\Delta W_{\text{ELM}}/W_{ped}$ with ν_{ped}^* that opens the access to small convective ELMs at ITER-like collisionalities. Although these conditions are not yet extrapolatable to the requirements for the ITER, $Q_{\text{DT}} = 10$ regime, they provide a very challenging test for the validation of models that need to be developed to predict the expected ELM energy losses in ITER.

Measurements at JET have demonstrated the validity of the kinetic picture for the description of the ELM energy fluxes to the divertor by determining the following:

1. the dependence of the ELM power flux rise timescale with the ion transit time in the SOL

2. the separation in time between the electron flux (measured with soft X-rays) and the ion flux (measured by Langmuir probes and D_α emission) at the divertor target

3. the in-out delays between the ELM ion fluxes at the inner and outer divertors

4. the detailed temporal dependence of the ELM divertor power flux waveform.

Similarly, measurements of plasma parameters in the SOL, following the radial propagation of the ELM-produced filaments and of plasma interaction with the main wall, have demonstrated that the dominant mechanism for radial energy transport during ELMs is convective ion transport. These measurements, together with those of the deficit of the ELM energy balance from divertor infrared measurements, have led to the development of models that can now describe the processes leading to the observed ELM fluxes at the divertor and main wall in ITER with reasonable accuracy.

VI. UNDERSTANDING OF MHD OF ELMs

VI.A. Early H-Mode MHD Studies

The first H-mode plasmas in JET were obtained in 1986 (Refs. 7 and 190). These early H-mode phases were mostly ELM free, with a continuous density rise up to a termination event. As a consequence, the first MHD studies[191,192] of the H-mode plasmas concentrate on the fluctuations observed at the L-H and H-L transitions. The fluctuations at the transitions are most likely to be type III ELMs. The rise time of these "spikes" is $\sim$50 to 100 μs; the magnetic perturbation shows a dominant $n = 0$ component, with the largest perturbation at the X-points. The localization obtained from soft X-ray (SXR) and reflectometer data is within the outer 10 cm of the plasma.

The first MHD stability analysis of the profiles in the JET H-mode plasmas was presented in Ref. 193. The $n = \infty$ ballooning stability boundary was calculated as a function of the edge pressure gradient and the edge current density. In these early calculations, the edge pressure gradient appears to cross the first ballooning stability limit. The edge current density is smaller than that required to access the second stable regime. In a more detailed study of the ballooning stability (including the bootstrap current from TRANSP analysis and the radial dependence of the stability limits) in JET H-modes,[194] the pressure gradient close to the edge becomes comparable to the first stability boundary. The edge current density is large enough to allow access to the second stable region. Given the radial resolution of the lidar of 9 cm, the values for the pressure gradient and the current densities correspond to lower limits. At the same time, ELM precursors and postcursors have been analyzed.[195] The precursors start about 0.5 ms before the ELM; postcursors can last up to 1 ms. The modes have a toroidal mode number $n = 1$ and rotate in the opposite sense to the neutral beam direction in the electron diamagnetic drift direction with a frequency of 6 to 8 kHz. Poloidal mode numbers are estimated to be between $m = 5$ and $m = 10$. The rotation direction leads to the interpretation of the precursors as being tearing modes.

High-frequency, $f \sim 50$ to 100 kHz, precursors to the ELMs were reported in Ref. 196. The precursors are localized in the outer 10% of the plasma and have an estimated mode number $n \geq 8$. Often the mode amplitude saturates before the ELM, although in some cases the precursor shows a rapid growth. At the ELM, the coherent mode develops into broadband turbulence. Ballooning stability analysis of type III ELMs shows the pressure gradient (from lidar) to be well below the first ballooning stability limit but close to the resistive ballooning stability for $n > 10$ (Ref. 197). During the large "singular" ELMs observed in high–poloidal beta discharges, the pressure gradient is close to the ideal limit.[198] Stability calculations of low-n resistive external kink modes showed the destabilizing effect of the current buildup during the H-mode.

VI.B. Hot-Ion H-Modes

With the emphasis of JET on high–fusion performance discharges, the MHD in so-called hot-ion H-mode discharges was studied in detail. Less attention was given to the stationary ELMy H-mode discharges. The hot-ion H-mode is obtained by strong heating of a low-density, low-recycling discharge. This yields a long ELM-free period with very good confinement properties and the largest neutron production rates in JET. These plasmas are characterized by a strong edge pedestal and, due to the low collisionality, a large edge bootstrap current.

The ballooning stability analysis[28,199] showed that the edge current is large enough to allow access to the second stable region for ballooning modes. The pressure gradients, as obtained from the reflectometer and the ECE radiometer, significantly exceed the first stability limit. This raised the question of whether the current required to access the second stable regime is small enough not to be unstable to an external kink. In Ref. 200 it was shown that this required current depends on the plasma shaping. The $n = 1$ kink mode was found to be stabilized by the edge pressure gradient (due to the favorable average curvature) to allow second stable access.

With the divertor installed in JET, the long ELM-free period that was common before was difficult to obtain. It was shown that plasma shaping, in particular triangularity (related to the shear at the plasma boundary), has a strong influence on the ELM-free period[201] and consequently the maximum fusion performance. The observed pressure gradient was found to scale with, but be below, the calculated (first) ballooning stability limit.[202] However, it remained unclear whether the ballooning modes would just limit the maximum gradient or actually cause the ELM.

The combined stability limits of the $n = \infty$ ballooning modes and the low-n external kink stability limits were studied as a function of the edge pressure gradient and the edge current density.[203] The low-n kink modes, destabilized by the edge current density, are stabilized by the edge pressure gradient up to values close to the first stability limit. At higher pressure gradients, the external kink modes are destabilized by the pressure gradients, first for the medium-n modes. The resulting edge stability diagrams indicate that whether the plasma runs into the ballooning or the kink limit depends on the ratio of the pressure gradient and the bootstrap current (determined by the collisionality). Stable access to the second stable regime (i.e., also stable to the external kink mode) depends on the plasma shaping and poloidal beta.

The high-performance phase of the hot-ion H-mode is limited by three different MHD events[204]: a giant ELM, a sawtooth, and a so-called slow "roll-over" mode, later better known as the "outer" mode.[205,206] The outer mode

is localized in the outer part (20%) of the plasma. The outer mode can cause a large reduction of the neutron rate and a loss of the hot-ion regime.[207,208] With the optimization of the hot-ion H-mode scenario, by operating at larger q_{95} ($q_{95} > 4$) and having better density control, the influence of the outer mode could be reduced to cause a slow saturation of the fusion performance. The mode is characterized by a low-n (mostly $n = 1$) toroidal mode number at a frequency of about 10 kHz and causes a displacement of the plasma of about 1 cm on the outboard midplane. The D_α radiation shows a small increase when the mode is present. An initial interpretation[206] identified the outer mode as a nonlinearly saturated external kink mode. This was later confirmed[209,210] by detailed comparisons of the SXR measurements and the predicted SXR perturbations based on the $n = 1$ ideal MHD external kink mode. Also, MHD stability calculations with the MISHKA code [developed at JET (Ref. 207)] showed that the edge bootstrap current can be large enough to destabilize the $n = 1$ external kink mode. The absolute amplitude of the plasma displacement was of the order of 1 cm at the outboard midplane and 10 cm at the X-point (due to the flux expansion). This indicates that an external kink mode by itself is not likely to cause giant ELMs but instead saturates at a relatively low level.

The detailed understanding of the underlying instability of the outer mode motivated experiments to reduce the driving force of the instability, the edge current density. The application of a current rampdown (200 to 400 kA/s) can stabilize or at least delay the onset of the outer mode in the high-performance phase of the hot-ion

H-mode discharges.[208,211] This technique became part of the standard hot-ion H-mode scenario and as such was also applied during the JET D-T discharges with the highest fusion power produced. The current rampdown was successful in stabilizing the outer mode, but it does cause the giant ELM to occur earlier in the discharge. This is consistent with the reduced ballooning stability limit due to the reduced total current. This is illustrated in Fig. 59, where two discharges are compared, one with and one without a current rampdown phase.

In the hot-ion H-mode discharges, the maximum pressure at the top of the pedestal was found to scale linearly with the total plasma current and the edge shear.[212] This scaling is consistent with a ballooning limit provided the width of the edge pedestal scales like a poloidal Larmor radius.

The lithium beam diagnostic for measurement of the edge density profile combined with the ECE electron temperature showed a continuously increasing edge electron pressure up to half (i.e., electron pressure only) the first ballooning stability limit.[213,214] However, the limited time resolution of 200 ms does not allow conclusions to be drawn as to whether there is a saturation of the edge pressure gradient before the ELM or not.

VI.C. ELMy H-Mode Studies

More evidence for the limit to the edge pressure gradient due to a ballooning-like mode comes from the observed scaling of the pressure at the top of the pedestal. The observed scaling of the pedestal pressure is linear in
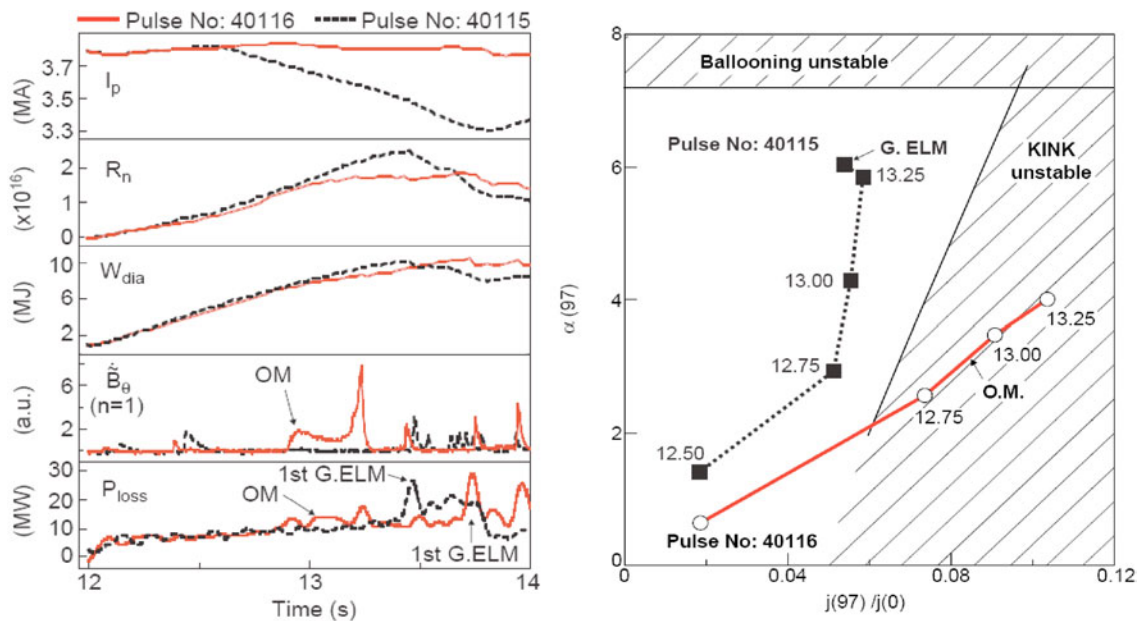

Fig. 59. Stabilization of the outer mode by a current rampdown. Comparison of two discharges with (40115) and without (40116) a current ramp (left) and the corresponding trajectories in the edge stability diagram (right). (From Ref. 208.)

the total current, the square root of the ion mass, and temperature and quadratic in the edge shear.[16] A linear dependence of the pedestal pressure on the plasma current was also observed in hot-ion H-mode discharges.[208,212] The stability limit due to a ballooning mode should give a quadratic dependence on the total plasma current for the critical pressure gradient (assuming the edge q-profile scales inversely with the total current). The width of the edge pedestal has been observed to scale as the poloidal Larmor radius, i.e., $\Delta \sim I^{-1}\sqrt{(m_i T)}$ (Ref. 16). Combining these results yields a scaling for the pressure at the pedestal top that is consistent with the observations. The quadratic dependence of the shear is not in agreement with the simple ballooning criterion. This discrepancy may be due to neglecting the edge bootstrap current in evaluating the edge shear.

A detailed study of ELM precursors in JET (precursors defined as modes observed in between and before ELMs) is described in Ref. 215. Using a combination of spectral and mode number analysis of the Mirnov data of several toroidally separated coils, coherent precursors with low- to medium-n mode numbers ($n = 1$ to ~ 13) have been observed. These modes are present, although not necessarily growing, before most type I ELMs. The modes are characterized by a frequency of 5 to 25 kHz with a lifetime varying from 0.2 ms to several tens of milliseconds. The modes are localized within a few centimeters inside the separatrix and have a displacement from 0.1 to 1.5 cm. No phase change has been found as a function of the radius (excluding tearing-like modes). At low n these precursors are identical to the so-called outer modes described previously. A clear correlation was identified between the toroidal mode number and the edge collisionality. At low collisionality (and consequently a large bootstrap current), the precursors have a low toroidal mode number $n = 1$ to 3, whereas at high collisionality the mode number goes up to $n = 10$ to 13 (see Fig. 60). This is consistent with low-n kink/peeling modes dominantly driven by the edge bootstrap current at low collisionality and medium-n ballooning (or peeling/ballooning) modes driven mostly by the edge pressure gradient at high collisionality.

A new MHD instability, named "washboard" mode due to its typical signature in the Mirnov data, was first identified by Ref. 216. The modes are present in most H-mode plasmas and appear in frequency bands between 10 and 100 kHz. Their frequency increases with the edge pedestal temperature. The amplitude of the mode fluctuates continuously, with a period of about 250 kHz with a typical displacement of the order of 1 mm. No radial phase changes have been observed. A detailed study of washboard modes has been presented in Ref. 137. The toroidal mode numbers vary from $n = 1$ to $n = 8$. The modes rotate in the electron diamagnetic direction, i.e., in the direction opposite to the ELM precursors described in the previous paragraph and opposite to the bulk plasma rotation direction. The identification in terms
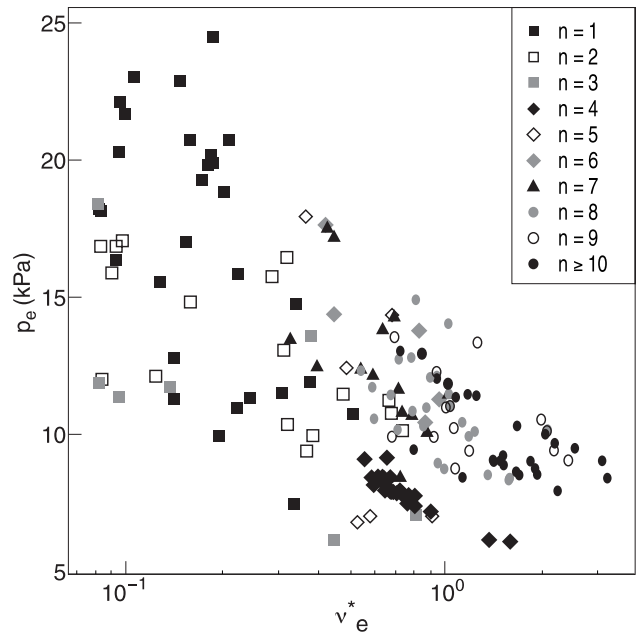
Fig. 60. The toroidal mode number of the type I ELM precursors as a function of collisionality and edge pedestal pressure. (From Ref. 215.)

of which MHD instability is responsible for the washboard modes is still an open question. Some form of a resistive ballooning mode has been proposed.[216]

The relevance of the washboard modes comes from the fact that these modes enhance the inter-ELM transport in the H-mode edge pedestal. The reheating of the (electron) temperature is slowed in the presence of the washboard modes, leading to a reduction of the ELM frequency. Interestingly, the amplitude of the washboard modes is reduced by the presence of the ELM precursors. The reduced amplitude leads to an increase in the reheating of the temperature and a reduction of the ELM period. The transport caused by the washboard modes can be large enough to cause a saturation of the edge temperature. However, the edge density continues to rise, eventually leading to an ELM when a critical pressure gradient is reached.

The washboard modes play an important role in the regime with mixed type I and type II ELMs (Refs. 18, 22, and 217). In this regime the frequency of the type I ELMs is reduced without an increase in energy losses per ELM. The increased inter-ELM losses are caused by the washboard modes. At low triangularity, gas puffing leads to a reduction in the washboard mode amplitude. In contrast, at high triangularity gas puffing leads to an increase in the washboard mode amplitude and the mixed type I-II ELM regime.

The actual ELMs (type I) show up as a burst of broadband activity in fast diagnostics such as the Mirnov coils. The duration of this activity is typically 150 to

300 μs. Due to the lack of coherence between the coil signals, it is difficult to establish toroidal mode numbers during the ELM. At high density, the ELM perturbation is observed to be toroidally localized.[218] The perturbation is found to rotate in the electron diamagnetic direction, opposite to the direction of the plasma flow. This has also been observed on the ELM-induced signals in the ICRH antennas,[219] showing a propagation speed of the order of 200 km/s.

VI.D. ELMy H-Mode: MHD Stability of the Edge Pedestal

In the early MHD stability analysis of JET discharges, the $n = \infty$ ballooning limit and the low-n external kink limit were taken into account to establish an edge stability diagram. More recently, the edge stability diagrams have been extended to include the medium-n (typically 5 to 20) MHD stability limits. These medium-n modes are the limiting instabilities in the so-called second stable regime for $n = \infty$ ballooning modes. In this region, at large edge pressure gradients and large edge current densities, the instability shows features of both the external kink (or peeling) mode and of the ballooning mode. These modes are therefore called peeling-ballooning modes.[220]

The MHD stability analysis of the edge pedestal, using the MISHKA-1 code to evaluate the stability of $n = 1$ to $n \sim 15$ to 20 or the ELITE code for the medium- to high-n modes, has become a standard tool[93,218,221–224] for the analysis of type I ELMs. Generally, the edge pressure gradient before the type I ELM is found to be in the second stable regime. The edge current density is large enough to stabilize the $n = \infty$ ballooning modes but not too large to destabilize the low-n kink modes. In this case the limiting instabilities are the medium-n (10 to 15) ballooning or peeling-ballooning modes. The stability limits strongly depend on the shaping of the plasma, notably the triangularity. A high triangularity stabilizes both the low-n current-driven external kink (peeling) modes and also the medium-n ballooning modes. Increasing the triangularity from $\delta = 0.23$ to $\delta = 0.47$ can increase the pressure gradient limit by as much as 50%.

An example using the best diagnostic information of the edge pressure profile available at JET is shown in Fig. 61 (Ref. 224). Here, the shape of the plasma has been chosen to optimize the radial resolution. The experimental point of the measured pressure gradient and the resulting calculated bootstrap current (i.e., the shear in Fig. 61b) before a type I ELM, given by the filled circle, is marginally unstable to $n = 10$ modes. After the ELM the pressure gradient drops to a value close to the stability limit for $n = \infty$ ballooning modes. The $n = 3$ modes at low shear (high edge current density) indicate the limit due to the current-driven kink modes. In this case the plasma edge is not close to the kink limit and the role of the current density is to facilitate the access to the second stable regime.
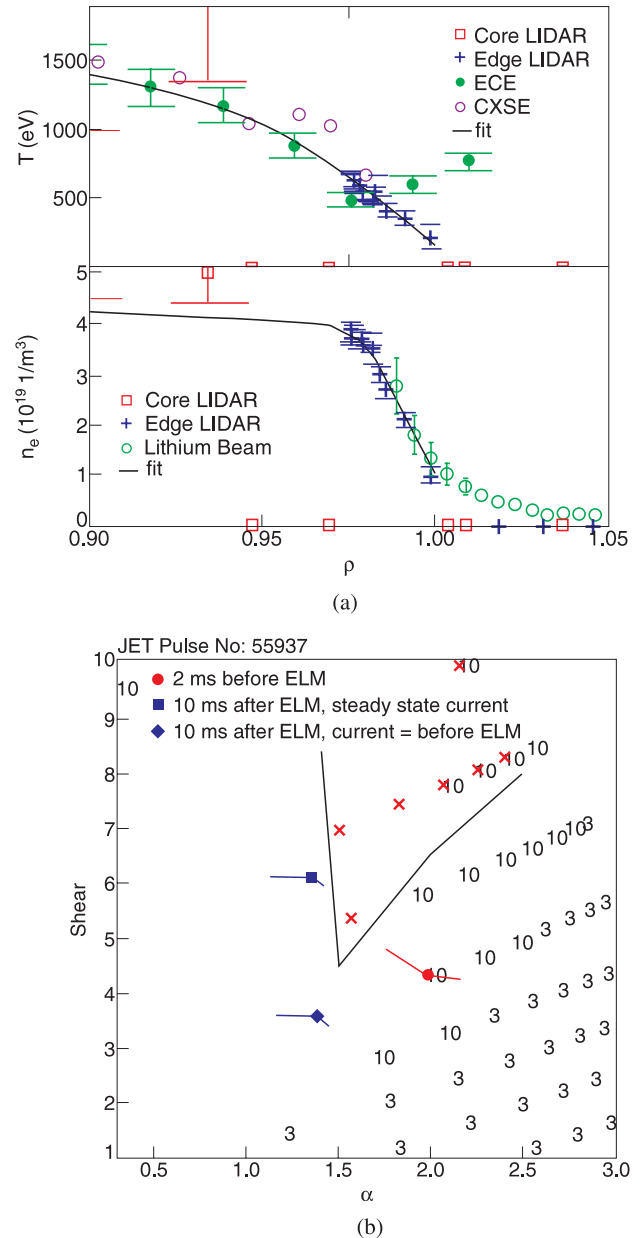
Fig. 61. (a) Profiles of the edge electron temperature and density as a function of radius in the edge pedestal from all relevant JET diagnostics in a plasma configuration optimized for the radial resolution. (b) MHD stability limits for the mode numbers $n = 1$ to $n = 10$ and the $n = \infty$ ballooning limit (full curve) as a function of the edge pressure gradient (α) and the edge shear (i.e., the inverse of the edge current density). The numbers indicate the mode number of the most unstable mode at that point in the s-α space. (From Ref. 224.)

The MHD stability limit to the edge pressure gradient is now well established. The importance of the edge current density also has been confirmed in experiments in which the edge current is increased using current

ramps.[225] Although very sensitive to the details of the current ramp, the increased edge current can, temporarily, avoid the deleterious type I ELMs in plasma with an ITB. More generally, the increased edge current in ITB plasmas, which typically have a very low internal inductance, has been proposed as a possible cause for the increased power threshold for the transition from type III to type I ELMs (Refs. 145 and 226).

Further progress in the MHD stability analysis requires routinely available high-resolution pressure gradient measurements, i.e., the temperature and density profiles, which are expected to be provided by the recently installed high-resolution Thomson scattering diagnostic.[131] The first analyses[227] for the small type II ELMs using this system show a considerable improvement in edge stability against peeling-ballooning modes in double-null configuration from that of the single-null plasma. The stability limit of the pure ballooning mode is much less affected.

Considering their possible importance in establishing a type II, i.e., small, ELM regime, the interpretation of the washboard modes is another important open issue. The (MHD?) instability causing the washboard is still unidentified. The kinetic ballooning mode has been proposed as a possible candidate, but this needs confirmation.

At the moment, the analysis of the ELMs is performed in terms of linear ideal MHD stability limits. However, to be able to answer the question as to what causes the size of an ELM in the different regimes, such as the change from type I ELMs to small grassy ELMs at high poloidal beta,[22] nonlinear MHD models and simulations are required.

VII. ELM MITIGATION

The type I ELMy H-mode is foreseen as the ITER baseline scenario for $Q = 10$ inductive operation[3] and all scalings are derived mainly for this scenario. However, the energy load to the divertor target plates and other wall components due to the unmitigated type I ELMs will most likely be too high to be acceptable for the lifetime of the PFCs (Ref. 152). An acceptable energy load is 40 MJ m^{-2} s$^{-1/2}$, which corresponds to about 6% of the pedestal stored energy in ITER. As discussed in Sec. V, the energy loads from type I ELMs might exceed this limit by a factor of 4 on the basis of current scalings, which assume that ELM size is related to edge collisionality. If the ELM size in ITER is not determined by the edge collisionality, but rather by the parallel transport time in the SOL, type I ELMy H-modes might be just acceptable for ITER. In addition, part of the ELM energy lost from the pedestal ΔW_{ELM} is not deposited in the divertor but instead to the other wall components. This fraction can be significant for large type I ELMs ($\approx 40\%$ of ΔW_{ELM}). This causes additional problems, and the scal-

ings of the power fluxes to the wall are not established yet. However, with large gaps to the walls, one can minimize the impact of the ELM power load on the limiters. But reducing the minor radius would limit the plasma volume and with this the fusion power of ITER in the worst case.

A further problem that already arises in present tokamaks is that the coupling of rf heating power to the plasma becomes poor in the presence of large type I ELMs. It is therefore mandatory to mitigate the type I ELMs or find alternative operating regimes with smaller ELMs or, even better, no ELMs.

Possible active ELM mitigation techniques are as follows: ELM pacemaking by frequent pellet injection, ELM mitigation by impurity radiation, and ELM mitigation by perturbed magnetic fields. Proposed alternatives to the type I ELMy H-mode, so-called passive ELM mitigation techniques, are the grassy ELM regime, type II ELM regime, type III ELM regime, QH-mode regime, and EDA regime.

VII.A. Type I ELM Mitigation

VII.A.1. ELM Mitigation by Impurity Radiation

ELM mitigation by impurity radiation is thought to be one of the most promising techniques, although it is generally found to be associated with a reduction in the energy confinement. At JET experiments were carried out by seeding argon and nitrogen in type I and type III ELMy H-modes. Argon and nitrogen were injected in type I ELMy H-modes up to radiative power fractions of 65% to avoid a transition into type III ELMy H-mode or accumulation of argon in the plasma core. By injecting the impurity into the plasma, the transient heat flux to the divertor target is reduced, but so also is the ELM energy lost at the pedestal. Hence, a reduction in the transient power loads to the divertor by increasing radiation does not necessarily mean that the ELM energy lost at the pedestal is dissipated by radiation in the SOL and/or divertor since the ELM energy loss ΔW_{ELM} is reduced as well.

A series of experiments have been carried out in which nitrogen and argon were seeded into type I ELMy H-modes with a low-triangularity magnetic configuration. The divertor power load due to ELMs was measured by infrared thermography. Injecting an impurity decreases the pedestal temperature and hence increases the pedestal collisionality. The pedestal lost energy ΔW_{ELM} is decreased consistently with the empirical scaling for unseeded plasmas.[228] Typically, the confinement enhancement factor is decreased from $H_{98(y,2)} = 1.0$ to $H_{98(y,2)} \sim 0.87$ to 0.97 (Ref. 229), depending on the radiative power fraction and the plasma density. As a consequence the energy to the divertor target is then decreased. Figure 62 shows ELM energy deposited on the divertor target versus the ELM energy lost from the plasma for non–argon
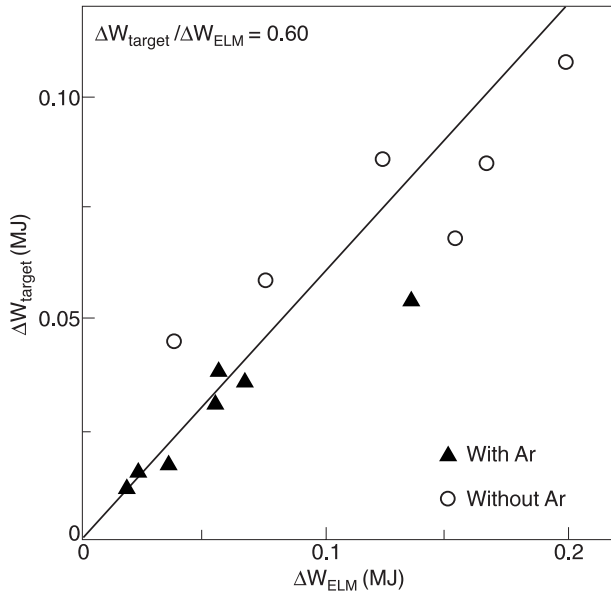
Fig. 62. Target energy load due to ELMs, ΔW_{target}, versus energy lost from plasma due to ELMs, ΔW. (From Ref. 230.)

a further unacceptable problem of the transient heat loads due to type I ELMs (Ref. 188). However, type III ELMs seem to deposit their whole power in the divertor. No significant difference in the ratio of ΔW_{target} to ΔW_{ELM} can be observed for nonseeded and argon-seeded discharges, indicating that radiative dissipation of the ELM energy from argon radiation is insignificant. However, detailed investigations in type I ELMy H-modes with nitrogen seeding show a slight difference. Figure 63 compares the ELM energy lost at the pedestal with ELM energy deposited on the outer and inner divertor targets for nitrogen-seeded type I ELMy H-modes. This reveals that the reduction of ELM energy due to radiative dissipation is about 20% on the outer divertor target and about 25% on the inner divertor target. Only very small ELMs (<25 kJ) can be dissipated to a significant extent by radiation. In strongly radiating type III ELMy H-modes, a reduction of more than 50% was observed[23] at a radiative power fraction of more than 85% (Fig. 64). This is consistent with EDGE2D/EIRENE modeling, which shows that the resilient nitrogen in the divertor region gets ionized to less effective radiating higher-ionization stages. Only for small ELM energies (<10 kJ) is a radiative dissipation effect noticeable. The modeling shows that in those cases of radiative dissipation, the electron temperature in front of the divertor target does not exceed 20 eV. This is consistent with Langmuir probe measurements, which show that during a small type III ELM at high radiative power fractions, the temperature T_e in front of the divertor target remains below 20 eV (Fig. 64;

seeded and argon-seeded plasmas. Only 60% of the energy lost from the plasma due to ELMs arrives on the divertor target. Most of the missing ELM energy is deposited on other first-wall elements and limiters. This is
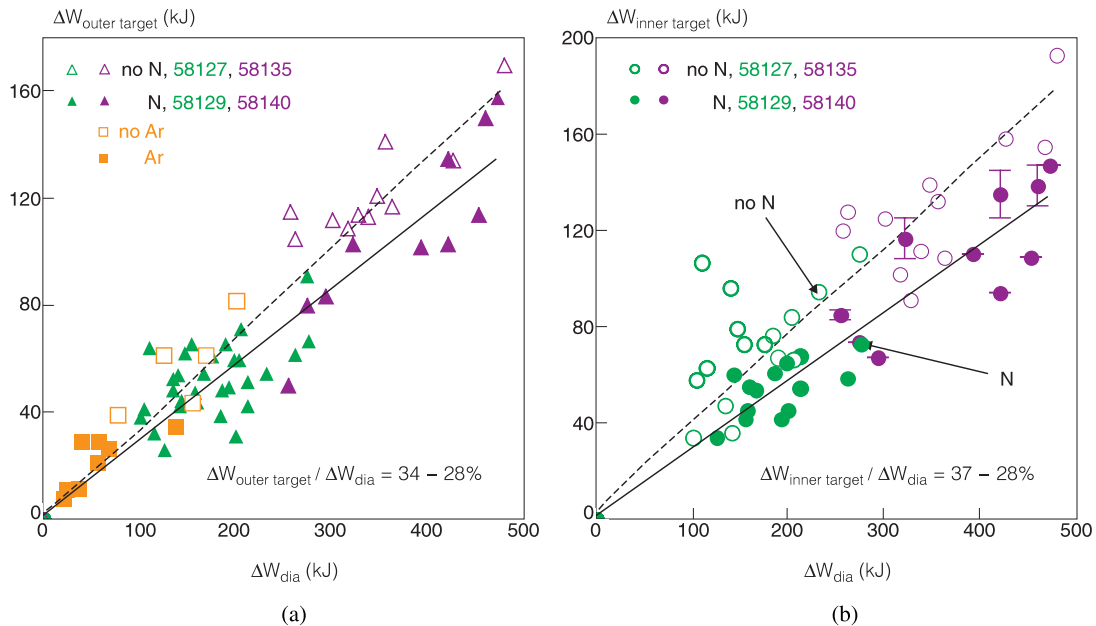

(a)

(b)

Fig. 63. Energy increase on the (a) outer and (b) inner divertor targets versus plasma energy lost during a type I ELM. Open symbols: without impurity fueling. Closed symbols refer to data from discharges with a radiative power fraction of ~55% through N or Ar seeding. (From Ref. 229.)
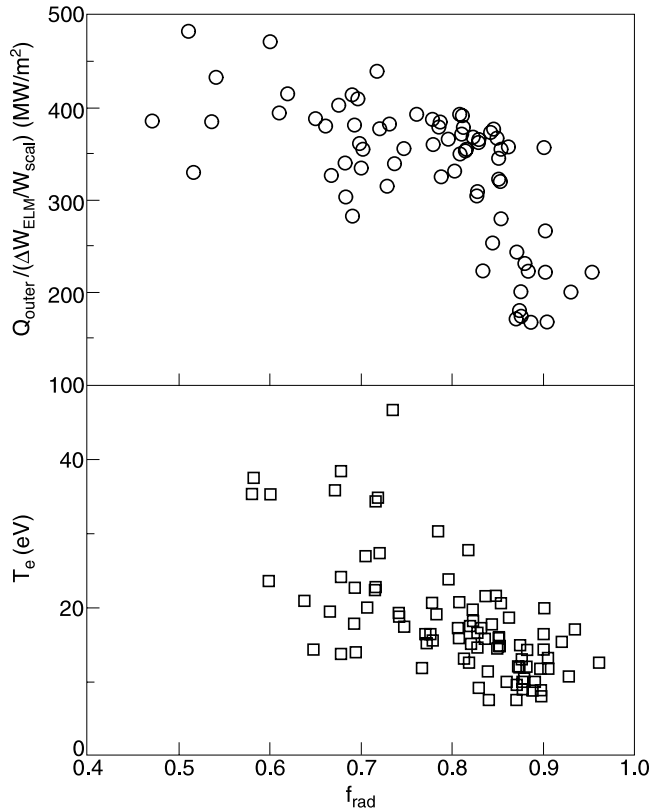
Fig. 64. For discharge 53318, the ratio of the heat flux density to the outer divertor target Q_{outer} to the predicted normalized energy loss scaling, $(\Delta W_{ELM}/W)_{scal} = (P/14P_{in})[1 - \exp(14/f_{ELM})]$ (see Ref. 58), and the electron temperature T_e in front of the target during the ELM peak (as measured by Langmuir probes versus the radiative power fraction). (From Ref. 230.)

Ref. 230). More recent modeling with SOLPS5.0/B2-EIRENE indicates that the ELM transport time might be an important factor in the ELM mitigation process.[229] Whereas for a short ELM time, the experimental results of negligible radiative dissipation are confirmed, long ELM transport times could lead to significant radiative dissipation of the ELM energy. In summary, for ITER, significant radiative dissipation of ELM energy is unlikely, based on modeling by B2-EIRENE (Ref. 161). Only for very small ELMs ($\Delta W_{ELM} < 0.6$ MJ) is ELM mitigation by radiation expected for ITER. However, the effect of the ELM transport time has not been taken into account in those ITER predictions. Also, it should be noted that all of these results from modeling are considered optimistic, since the fluid codes B2 and EDGE2D do not cover kinetic effects, which should be included in ELM modeling activities. Hence, ELM mitigation by radiation is limited to small ELM regimes and is addressed below.

There are some "side effects" of impurity seeding, which can also reduce the transient heat loads. The radiative boundary has an effect on the pedestal itself. Depending on the Z of the impurity, an impurity radiates more or less in the main plasma. In JET ELMy H-modes, argon radiates a nonnegligible part in the main plasma, thus reducing the power flux across the pedestal. This can reduce the ELM frequency of the plasma.[231] But this does not necessarily reduce the energy lost at the pedestal ΔW_{ELM}. This mainly depends on fueling and recycling of gas (deuterium and impurity gas). In so-called after-puff experiments (described in detail in Sec. VIII), the fueling of the impurity seeding is minimized, which leads to a lower ELM frequency and only slightly reduced pedestal temperatures, with the consequence that the ΔW_{ELM} is also not reduced significantly. The normalized ELM energy loss in those after-puff experiments shows a behavior similar to that of the nonseeded type I ELMy H-modes.

The reduced number of ELMs has very little effect on the divertor lifetime. Only if the pedestal temperature is reduced, and hence $\Delta W_{ELM}/W$ is smaller by a factor of 2 to 3, together with a reduced ELM frequency could the divertor lifetime be just acceptable. But for this, radiative power fractions significantly higher than 75% need to be realized. The application of this scenario depends on the accessibility of the type I ELMy H-modes and the operational domain of the type III ELMy H-mode.

VII.A.2. ELM Mitigation by Perturbed Magnetic Fields

The effect of perturbing magnetic fields on the stability of ELMs has been investigated on several tokamaks.[232,233] Successful suppression of type I ELMs has been demonstrated on DIII-D with resonant magnetic fields[234] ($n = 3$). However, the results from DIII-D have shown that with $n = 3$ perturbation fields, the edge safety factor was a crucial quantity and complete ELM suppression was achieved only within a narrow range.[234] On the other hand, all of these experiments were carried out with perturbation fields created by in-vessel magnetic coils. At ITER the installation of in-vessel magnetic coils is unlikely, due to technical difficulties mainly related to the required coil cooling. Therefore, solutions that make use of external coils are much more favorable. At JET, experiments with ex-vessel magnetic perturbation coils have been carried out. JET has a set of four error field correction coils (EFCCs) mounted at equally spaced toroidal positions and attached to the transformer yokes. Depending on the wiring of the EFCCs, $n = 1$ or $n = 2$ external magnetic perturbation fields can be created. Recently, ELM mitigation experiments using the $n = 1$ configuration were carried out successfully.[235] Figure 65 shows an overview of an ELM mitigation pulse. The $n = 1$ perturbation field created by the EFCCs has a half–sine shaped waveform for 1.2 s, which is a factor of ≈ 5 longer than the energy confinement time. As soon as the perturbation field reaches a critical amplitude
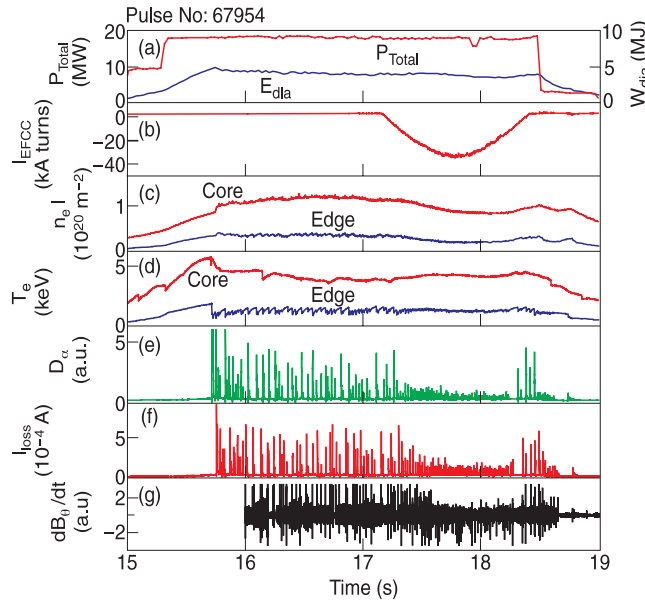
Fig. 65. Time traces of an ELM mitigation experiment with magnetic perturbation fields created by EFCCs: diamagnetic energy E_{dia}, current through the EFCC I_{EFCC}, line average density n_{el}, fast ion loss I_{loss}, and change in poloidal magnetic field dB_θ/dt. (From Ref. 235.)
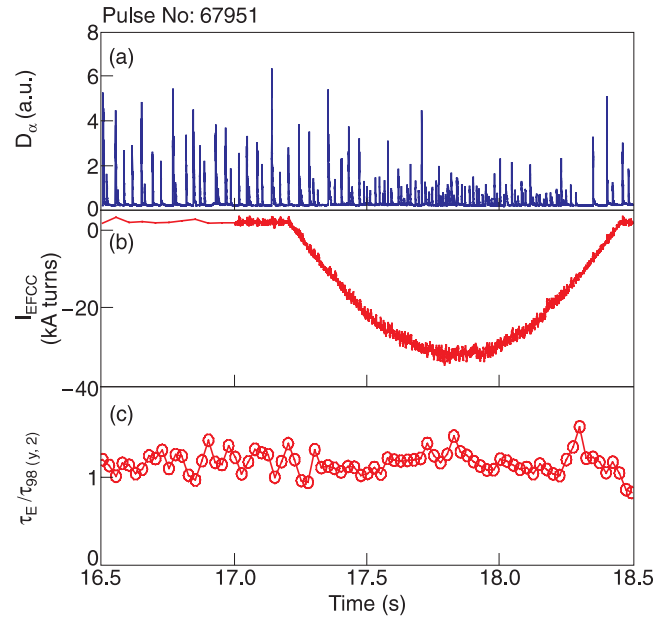

Fig. 66. The global thermal energy confinement time from TRANSP modeling (and hence derived from the kinetic energy) normalized to the IPB98(y,2) value shows almost no decrease, although the pedestal energy is reduced with the magnetic field perturbation. This is due to the positive density dependence of the IPB98(y,2) scaling and the increased core temperatures in this example. (From Ref. 235.)

($I_{EFCC} \sim 10$ kA turns) a density pump-out at the pedestal occurs, which is a typical signature for the ergodization of the edge plasma. Simultaneously, a strong reduction of the divertor D_α light (representative of the D fluxes) is observed. The ELM frequency is increased from 30 to 120 Hz and the ELM energy loss $\Delta W_{ELM}/W$ is decreased from 7% to less than 2%.

The $n = 1$ perturbation field results in a strong braking of the plasma rotation as observed in the toroidal rotation profile or from the frequency of core-localized MHD modes. For ELM mitigation the amplitude of the external perturbation field has been kept below the threshold for the excitation of a locked mode. Transport analysis using the TRANSP code shows that the thermal energy confinement time drops because of the density pump-out, which leads to increased convective losses. However, when normalized to the $\tau_{98(y,2)}$ scaling, almost no effect is seen (see Fig. 66), since the scaled energy confinement time $T_{98(y,2)}$ has a positive density dependence ($\tau_{98(y,2)}$ is proportional to $n^{0.4}$). Experimentally, this is also seen in the increased temperatures (T_e and T_i) in the plasma core during the density pump-out.

Further expanding the operation domain to more ITER-relevant parameters has been started.[25] Similar encouraging results have been obtained in a wide operation regime on JET with the upper triangularity up to 0.45, plasma current up to 2.0 MA, and q_{95} varied between 3.0 and 4.8. In the JET experiments, the minimum amplitude of the $n = 1$ perturbation field above which the ELMs

were mitigated increased as q_{95} was decreased but always remained below the $n = 1$ locked mode threshold. ELM mitigation was also found in high-beta pulses ($\beta_N = 3.0$) without degradation of the H-factor. This is a demonstration that the operational domain of ELM mitigation by $n = 1$ perturbation fields is very wide. However, a confident scaling to ITER needs further investigations on the extension of the operational domain, in particular to high edge density and ITER collisionality.

VII.A.3. ELM Mitigation by Pellet Injection

Shallow pellet injection is thought to be a tool to increase the type I ELM frequency (ELM pacemaking) and consequentially reduce the power load per ELM on the divertor target. This method was developed and has been investigated at ASDEX Upgrade[236] and is considered a potential tool for ITER. The centrifuge-based pellet system operated at JET in the period from 1995 through 2003 was designed for fueling studies with pellet sizes of $(4 \text{ mm})^3$ (about 4×10^{21} D atoms) and injection velocities of 150 to 300 m/s, which is not consistent with the design requirements of an ELM pacemaking injection system, which call for smaller pellets. Too large pellets might change the ELM regime temporarily or even trigger L-mode phases. Nevertheless, the principal

ELM-triggering mechanism was studied at JET (Ref. 24). It was found that despite the fueling effects of the large pellets, ELMs are triggered at any time in the ELM cycle (see Fig. 67). Only a minor amount of a fueling-sized pellet mass is ablated during the penetration of the plasma up to the pedestal top, triggering the ELM. The pellet-triggered ELM appears not to be different from an intrinsically occurring one in terms of energy loss. A pellet size of 4×10^{19} D atoms (only 1% of the pellet) is estimated to be sufficient for triggering the ELM in the scenario studied. However, a reduced pellet mass is expected to cause a reduced ablation rate. A reduction in pellet mass by a factor of 100 might lead to reduction of the ablation rate by a factor of 10, as simulations and a multimachine scaling for pellet ablation suggests. Hence, a lower radial velocity of the pellet might be required to increase the perturbation at the pedestal, if the ablation rate of the small pellets becomes too low. A reduced pellet radial velocity can be achieved by a reduced launch velocity and a change in the inclination angle of the trajectory. This requires dedicated ELM pacemaking experiments. A new pellet injection system is being built for this purpose.[237] This new system should enable the injection of small pellets at large frequencies with adaptable injection velocities. In addition to the question of pellet penetration, ELM triggering, and simultaneous fueling of the main plasma, the question of the confinement degradation due to this ELM mitigation technique has to be assessed. An increased ELM frequency from fueling usually leads to a confinement degradation at JET (Ref. 58). At ASDEX Upgrade it has been found that the confinement due to ELM pacemaking by pellet injection is degraded but less than in comparable discharges with gas fueling. However, too strong a fueling by the pellets could lead to unwanted density perturbations. Eventually, with this new system the important questions with respect to the confinement degradation at ITER-relevant densities close to the Greenwald density will be answered.

VII.B. Passive ELM Mitigation: Alternative H-Mode Operation Regimes

VII.B.1. Radiative Type III ELMy H-Mode

The type III ELMy H-mode is a robust operation regime, which has been demonstrated on many tokamaks.[116,134] Type III ELMs are characterized by a small amplitude and have a repetition rate of ~ 100 to 1000 Hz at JET. They occur at low heating powers, below the type I ELMy H-mode power threshold, or in H-modes that are heavily fueled by the main fuel and/or impurity gases. The ELM energy loss at the pedestal is small (at JET usually below the detection limit) and acceptable when projected to ITER. Usually they are accompanied by a degradation of confinement ($H_{98(y,2)} \approx 0.75$), which disqualifies this regime for the standard ITER operation at 15 MA. However, at 17 MA and 5.3 T ($q_{95} = 2.6$), ITER

has an operation window for $H_{98(y,2)}$ factors of 0.75. Such an integrated ITER scenario with small type III ELMs, high radiation, and acceptable confinement at low safety factors has been demonstrated at JET (Ref. 230), although the challenges of avoiding neoclassical tearing modes with these plasmas are greater. Nitrogen was seeded as an impurity, creating a radiative divertor plasma with a radiative power fraction of $f_{rad} \sim 0.8$ at the Greenwald density. An example of such a discharge is shown in Fig. 68. Almost all dimensionless parameters, such as $H_{98(y,2)} = 0.73$, $f_{Gr} = 1.05$, $f_{rad} = 0.8$, and $\beta_N = 1.7$, are within the ITER operation domain for $Q = 10$, except for the nondimensional quantities ν^* and ρ^*. Most important, the power fluxes to the divertor target are significantly reduced compared to those of type I ELMy H-modes in similar conditions. Typically, the $\Delta W_{ELM}/W$ is smaller than 1.5% and the steady state power fluxes to the divertor are reduced to 2 to 5 MW/m^2. The transient power flux due to type III ELMs is in the range of 2 to 7 MW/m^2, which has to be compared to ~ 15 MW/m^2 for similar type I ELMy H-modes. The divertor plasma is completely detached in between ELMs and attaches during the ELM heat pulse. Radiation feedback control of those type III ELMy H-modes has been demonstrated.[238]

The extrapolation of this integrated operation scenario to ITER has been advanced but is still ongoing. Assuming even the most pessimistic scaling,[228] the ELM energy losses are estimated to be acceptable even for the lowest collisionalities. Nonseeded type III ELMy H-modes show a $\Delta W_{ELM}/W_{ped}$ of about 11% $\pm$ 4%. This is consistent with predictions for ITER, which requires a $\Delta W_{ELM}/W_{ped}$ of about 3 to 7% for the standard 15-MA inductive scenario and about 7 to 11% for the 17-MA inductive scenario with a type III ELMy edge.

The extrapolation of the fuel dilution due to the seeded impurity is more difficult. Z_{eff} is not a scaled quantity, although some attempts have been made to develop a multimachine Z_{eff} scaling.[239] The most influential parameter in the empirical Z_{eff} scaling is the plasma density: $Z_{eff} = 1 + 7P_{rad}/(Sn_e^2)$, where S is the plasma surface area. But it was also thought that the closure of the divertor has a large impact on the detachment behavior and the impurity retention. Therefore, the JET divertor was made more closed by replacing the very open MkI divertor and MkIIA divertor with the gas box divertor MkIIGB. But it turned out that the divertor geometry had no significant impact on this regime. The closure of the divertor resulted only in a negligible difference in the onset of detachment with respect to the plasma density. However, for closed divertors a complete detachment of the divertor plasma is achieved at lower radiative power fractions.[230] The removal of the septum in the MkIIGB had no influence at all on the regime.[238] High radiative power fractions were obtained with all JET divertors. This is also reflected in the invariance of Z_{eff} with the divertor geometry in those impurity-seeded discharges. This becomes apparent if one looks closely at the radiation

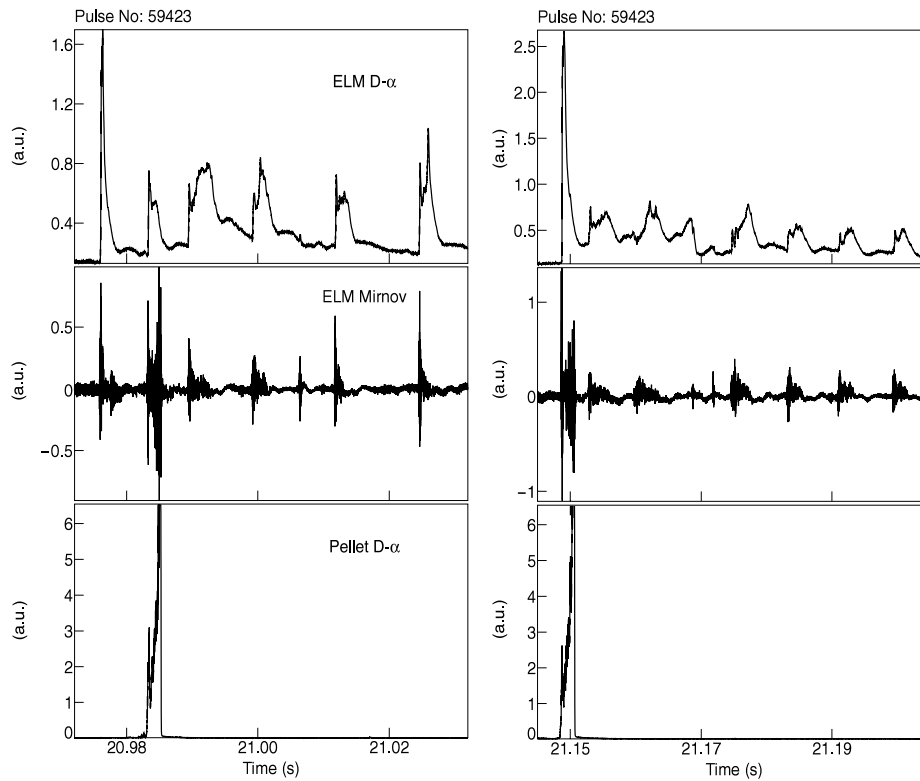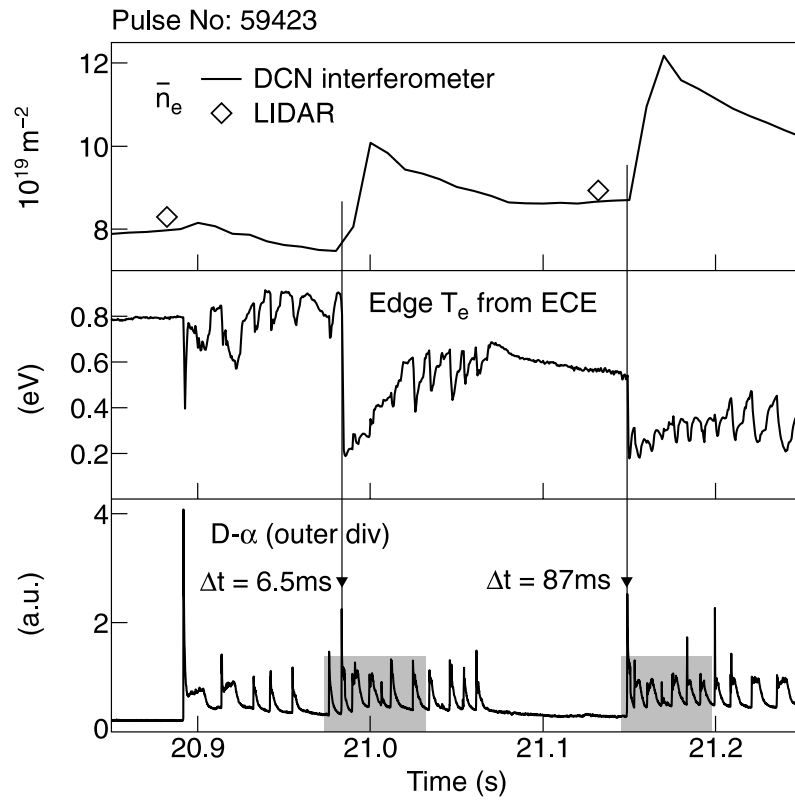Fig. 67. Time traces for pellet-triggered ELMs at arbitrary times in the ELM cycle. Line average density, central density (pellet induced changes qualitatively only!), and outer divertor D_α ELM monitor. Both pellets trigger an ELM despite a different elapsed time with respect to the previous event. Pellet-induced ELMs consist of a fast and a slower component; the latter is thought to be fueling induced. (From Ref. 24.)
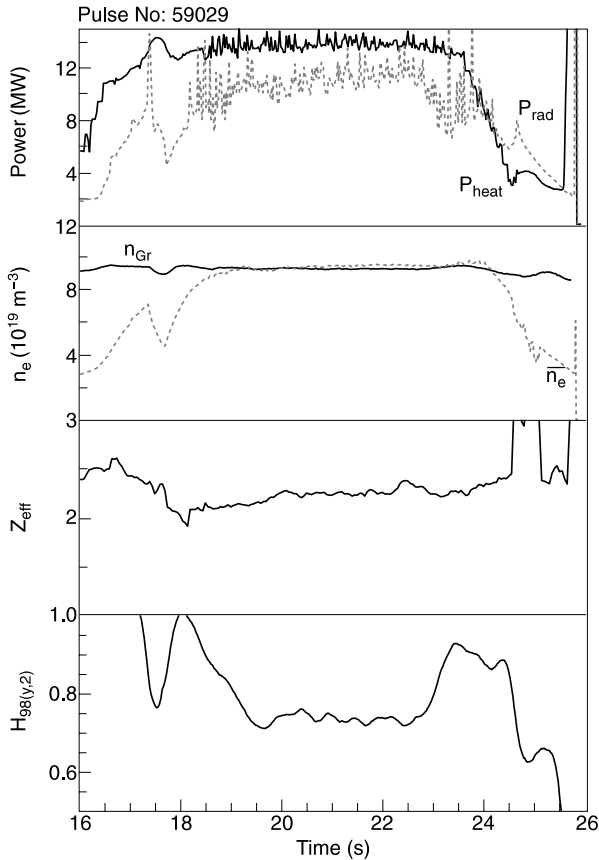
Pulse No: 59029

Fig. 68. Time traces of nitrogen-seeded type III ELMy H-mode 59029, 2.5 MA and 2.0 T. (From Ref. 230.)

profiles obtained by tomographic reconstruction of bolometer data. At the high radiative power fractions in nitrogen-seeded discharges, most of the plasma radiation originates from the X-point region, within the last closed flux surface, and is not located deep in the divertor. The detached divertor radiation leads also to a strong reduction of the carbon fluxes in the divertor, which is derived from CII radiation.[238] The seeded impurity is the dominant impurity.

Hence, it would appear that the only way to reduce Z_{eff} is by increasing plasma density. Recent experiments have shown that the fuel dilution from the seeded impurity can be limited at high-density operation, leading to Z_{eff} values of 1.5 to 1.7 (Ref. 240).

The extrapolation of the confinement is even more difficult. Detailed investigations of nitrogen-seeded discharges with respect to dimensionless scaling of ρ^* and ν^* (Ref. 239) demonstrated the difficulties related to impurity-seeded discharges. Predictions of the confinement scaling (Bohm-like transport or gyro-Bohm-like transport) depend strongly on the collisionality dependence. Unfortunately, the collisionality cannot be kept constant in those dimensionless ρ^* experiments with radiative plasmas. Comparing the highly radiative plasmas

to the ELM-free H-mode scaling of H_{93} (Ref. 241) would suggest that the transport is Bohm-like. However, the ELMy H-mode scaling $H_{98(y,2)}$ of ν^* is close to zero ($\nu^{*-0.01}$). In this case, both the global confinement scaling and the local transport analysis of the core appear consistent with gyro-Bohm, if one takes into account differences in the pedestal and the heating profile for the low-current 1 MA, 1 T discharges. Recent experiments confirm the weak collisionality dependence of the confinement enhancement factor $H_{98(y,2)}$. This makes the gyro-Bohm scaling more likely. Demonstration of these modes at even lower collisionality will clarify this further and will also determine whether impurity-seeded type III ELMy H-mode operation is possible at the ν^* range of ITER.

Radiative type III ELMy hybrid discharges have been demonstrated at a q_{95} of 3 (Ref. 242). The characteristics of these discharges were quite similar to those of the standard radiative type III ELMy H-mode with a low edge safety factor of 2.6. Nevertheless, it demonstrated the ability of this regime to go to high beta operation, with β_N of 2.6.

VII.B.2. Type II ELMy H-Mode

H-modes with good confinement and small ELMs with the characteristics of type II ELMs have been observed on many tokamaks.[134,135] Type II ELM H-modes were found at JET and are discussed further in Secs. IV.C and IV.D. Type II ELMs are characterized by a significantly reduced ELM energy loss $\Delta W_{ELM}/W$ without any impact on the plasma confinement. At JET type II ELMs mostly occur in a mixture with type I ELMs. Pure type II ELMs are found in QDN discharges, although it remains to be seen whether they can be produced at sufficiently low safety factors and collisionalities to be ITER relevant.

VII.B.3. Grassy ELMs

The grassy ELMs discussed here appear when the pressure is increased above a critical level, as first observed at JT-60U (Ref. 148). This small-ELM regime is characterized by good confinement in high-β_p, high-l_i, high-δ, high-q_{95} discharges. The grassy ELMs appear when the pressure is increased above a critical level. Grassy ELMs have been observed in JET and are discussed further in Sec. IV.F. Grassy ELMs show a pedestal pressure similar to that of type I ELMs. The difference from the type I ELMs is that the radial extend of the pedestal temperature perturbation due to the grassy ELM is very narrow, so the ELM size becomes smaller than that of a type I ELM. Another difference from the type II ELM is that there are no inter-ELM losses. The ELM energy loss itself is smaller than the detection limit of the diamagnetic loop and therefore cannot be quantified. Experiments at higher current and lower q_{95} are required to qualify this regime as an ITER-relevant scenario.

VII.B.4. Other Regimes

Other regimes such as the "quiescent" H-mode (QH-mode) have shown good confinement with a complete absence of ELMs. They were first reported from DIII-D (Ref. 243). At JET QH-mode experiments were carried out in a dedicated reversed B_T and reversed I_p experimental campaign with countercurrent neutral beam heating.[29] The magnetic configuration in those experiments was chosen to have a large wall clearance (>15 cm) and good particle exhaust, by positioning the divertor strike points close to the entry to the divertor cryopump. Low recycling was achieved by the time-consuming method of He glow discharge cleaning, cryopumping, and Be evaporation. Discharges of different currents (1.5 to 2.5 MA) and q_{95} (3.3 to 4.9) were performed leading to "quiescent" (ELM-free) phases of $\sim$1.5 s. Those ELM-free phases are stationary and do not experience a strong density ($f_{Gr} < 0.4$) or radiation increase, as is usually seen in ELM-free phases. The confinement is similar to that of type I ELMy H-modes; however, the Z_{eff} is increased to values of 4 to 5. These high values of Z_{eff}, which are typical for QH-modes, are the main drawback of this regime. The loss mechanism in this regime is attributed to MHD activity. The ELM-free phases are accompanied by so-called edge harmonic oscillations. Although the observed ELM-free phases show many of the features of the QH-mode, it has not been able to extend those short "quiescent" phases for more than 1.5 s. Also, the pulses have not been reproducible at JET. The best conditions are obtained after fresh vessel conditioning. There are also doubts as to whether the operation domain of this regime can be expanded to higher densities (up to the Greenwald density).

The EDA regime is another ELM-free regime, which was first observed on Alcator C-MOD (Ref. 244) and gets its name from the characteristic high D_α radiation. On JET, however, experiments to reproduce this regime were unsuccessful.

VII.C. Conclusions

Active and passive ELM mitigation has been studied at JET. Promising results were obtained with the active control of type I ELMs by $n = 1$ magnetic perturbation fields. Parameter scans in q_{95}, shaping (δ), and collisionality indicate that the operation domain of this ELM mitigation technique is wide. However, the density pump-out associated with the edge perturbations needs to be compensated.

The feasibility of ELM mitigation by frequent pellet injection was also studied. Type I ELMs can be triggered prematurely by pellets. However, ELM pacemaking was not demonstrated due to the technical capabilities of the JET pellet injection system. A new pellet injection system is being built, dedicated to ELM mitigation studies.

Impurity injection experiments revealed that ELM mitigation by radiative dissipation of large type I ELMs is not possible. Only small ELMs can be buffered by the radiative divertor, which was demonstrated in radiative type III ELMy H-modes.

Many alternative H-mode scenarios with small ELMs have been studied at JET. All of these regimes comprise small ELMs for acceptable divertor heat loads. But from among all the passive ELM mitigation schemes, only the type III ELMy H-mode has an operation domain consistent with a $Q = 10$ ITER operation scenario. Most of the other regimes are limited to high q_{95} or high collisionality or specific plasma shapes (QDN configuration). The search for robust scenarios that extrapolate to the $Q = 10$, 15-MA ITER scenario with tolerable ELMs continues.

VIII. EXPERIMENTS WITH RADIATIVE MANTLE PLASMAS

This section summarizes results obtained in L-mode and ELMy H-mode in JET using the noble gases Ne and Ar as seeding impurities. High confinement and high levels of edge radiation could be simultaneously realized in these discharges, using a careful seeding of both Ar and D_2. A dual-feedback control for simultaneous seeding of Ar and puffing of D_2 was developed and successfully demonstrated. Influence of impurity seeding on the character of the ELMs and on the first-wall power loads is discussed.

VIII.A. Introduction

One possible route to optimize the lifetime of the first wall of ITER and future fusion power reactors is to add controlled quantities of impurities in the plasma edge, resulting in the creation of a radiative mantle in the boundary. This aims at offering a solution for two major issues of a fusion reactor:

1. to distribute the heat load uniformly over the first wall as a means to avoid local overheating

2. to reduce the temperature in the plasma edge, thereby lowering the energy of escaping plasma particles in order to reduce sputtering and erosion of the PFCs (Refs. 245 and 246).

Externally seeded impurities will be unavoidable in future fusion reactors with metallic walls, where radiation of intrinsic impurities will be small.

Extensive experiments with seeding of impurities in tokamak plasmas were done on ISX-B in the 1980s, leading to the discovery of the Z-mode.[247,248] Succeeding experiments with radiating mantles were performed in TEXTOR in the 1990s, confirming the validity of the concept.[249,250] In later experiments, a significant improvement in confinement was additionally observed (RI-mode), initially using neon and silicon (or combinations)[251–255] and later also argon as a radiating impurity.[256,257] First modeling of the discharges was reported in Ref. 258, and further investigations revealed that the

confinement improvement in TEXTOR can be attributed to the stabilization of ion temperature gradient (ITG) modes[259–261] predominantly by the density gradient. The experiments on TEXTOR were followed on several other tokamaks,[262–265] including JET (Ref. 266). Several experimental campaigns have been devoted to this work at JET (Refs. 17, 267, 268, and 269), and it is the purpose of this section to summarize the results obtained so far on this machine. The results obtained on JET have shown that it is possible to create a radiating zone in the edge of various plasma types[270] and that under certain conditions, confinement can be improved or kept at a high level. To this end, gas-puffing schemes were first preprogrammed ("puff/afterpuff" scheme) and later followed by feedback control of both the Ar and D_2 inputs to increase the stationarity of the plasma. In addition to the radiating edge and confinement changes, the ELM type in H-mode plasmas can be influenced by impurity seeding, and depending on the discharge type, infrequent type I ELMs can be transformed into frequent type III or irregular ELMs with high frequency and reduced amplitude, as discussed in Sec. VII.

Here we discuss only JET experiments using seeding with noble gases. Seeding with other impurities, such as nitrogen,[230] are dealt with elsewhere in this issue since the general characteristics of such discharges are much different, due to the very different recycling properties of nitrogen.

VIII.B. Main Characteristics of Discharges with a Radiative Mantle on TEXTOR

TEXTOR is a medium-size limiter tokamak ($R = 1.75$ m and $a = 0.46$ m; Ref. 271) equipped with a toroidal pumped limiter ALT-II (Advanced Limiter Test-II) (Ref. 272). Discharges on TEXTOR with a radiating mantle and exhibiting enhanced confinement [called RI-mode on TEXTOR (Ref. 251)] are obtained with the following:

1. NBI coheating and/or NBI counterheating and/or ICRH

2. feedback-controlled seeding of impurities (Ne, Ar) in a boronized machine

3. sputtering of Si in a siliconized machine, possibly further enhanced by feedback-controlled Ne seeding.

Confinement in the RI-mode depends linearly on the plasma density, $\tau_{RI} = K\overline{n_e}P_{tot}^{-0.66}$ (where $K = 0.18$ if the confinement time τ_{RI} is expressed in seconds, the central line average electron density $\overline{n_e}$ in 10^{20} m^{-3}, and the total heating power P_{tot} in MW),[273] and highest confinement is reached in the absence of gas puffing. The linear density dependence is limited by the experimental ceiling $\beta_N \sim 2$. Strong deuterium puffing reduces confinement.[274] However, this property of gas fueling was used

to advantage in TEXTOR by applying a well-chosen moderate level of gas puffing in the discharge, reducing the high confinement of the RI-mode at the highest densities to levels avoiding β limitations. The net result is that densities above the empirical Greenwald limit[6] n_{Gr} up to $\overline{n_e}/n_{Gr} = 1.4$ together with ELM-free confinement quality could be reached.[275] In addition, this high-density regime is favorable for helium removal and results in figures of merit $\tau_{P,He}^*/\tau_E \approx 10$ to 15, relevant for a future fusion power reactor. This regime has been demonstrated on TEXTOR for quasi-stationary periods of several seconds, equivalent to more than 160 energy confinement times or several skin times.[276]

VIII.C. Early Experiments with Radiative Mantles in Ne-Seeded H-Mode Plasmas on JET

In the first radiative mantle experiments at JET attempting to replicate the RI regime of TEXTOR, two divertor configurations were used:

1. a corner configuration (with the strike points at the location of the cryopump port) to maximize the divertor's impurity pumping capability

2. a septum configuration (Fig. 69) in which the X-point was lowered onto or just inside the material barrier (called the septum or dome), dividing the inboard and outboard sides of the divertor.
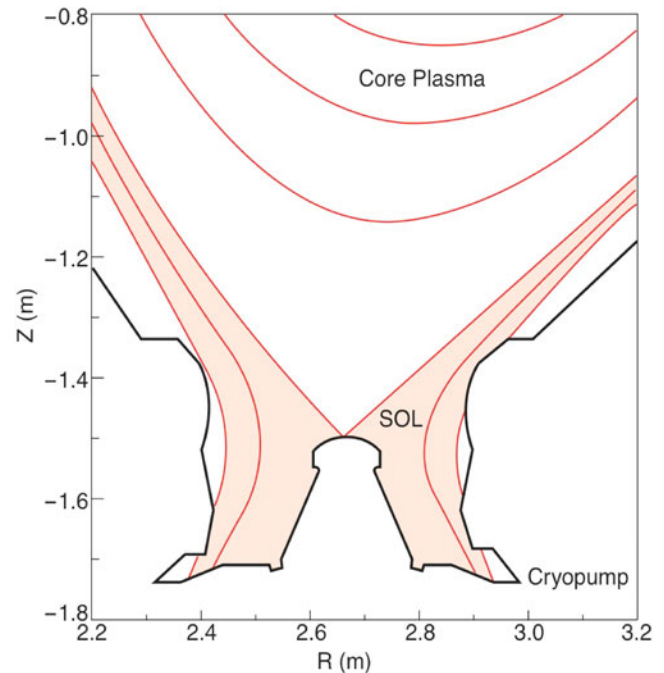

Fig. 69. Septum configuration in which the X-point is embedded in the top of the dome in the JET divertor (MkIIGB).

The idea behind this second configuration was twofold:

1. It showed a reduction by a factor of 2 in the L-H threshold power,[113] beneficial to keeping the H-mode during impurity-seeding experiments with high levels of edge radiation.

2. It allowed us to use the top of the dome as a toroidal limiter, thereby mimicking the function of the belt limiter of TEXTOR.

This configuration thus approached a combination of a divertor and a pumped-limiter configuration.

JET discharges (ELMy H-modes, 2.5 MA and 2.7 T) heated by 12-MW neutral beams with argon or neon radiating mantles were executed.[266] Argon produced more mantle radiation than neon, and both impurities led to about the same X-point radiation. Both plasmas were at 85% of the Greenwald density limit, with similar beam-heating power densities. The width (in absolute terms) of the JET edge radiating mantle was about half the TEXTOR neon width and a quarter of the TEXTOR argon width. Argon and neon in TEXTOR each caused a 30% increase in the global confinement. By contrast, JET experienced a 15% decrease in confinement in these early radiative mantle plasma scenarios at the same density as discharges without Ne seeding.

VIII.D. Radiative Mantle Plasmas with High Confinement in JET

To overcome the confinement degradation, a modification of the preprogrammed D-puff timing was implemented, based on the TEXTOR experience that highest confinement was reached in the absence of gas puffing. This was necessary for the low-triangularity configurations with the X-point on top of the dome. An example is shown in Fig. 70a. After the start of the additional heating, a strong gas puff was applied in order to increase the density. Confinement was correspondingly reduced in this phase, as also observed on TEXTOR. The strong confinement degradation is clearly shown in the reduction of the enhancement factor $H_{98(y,2)}$ with respect to the
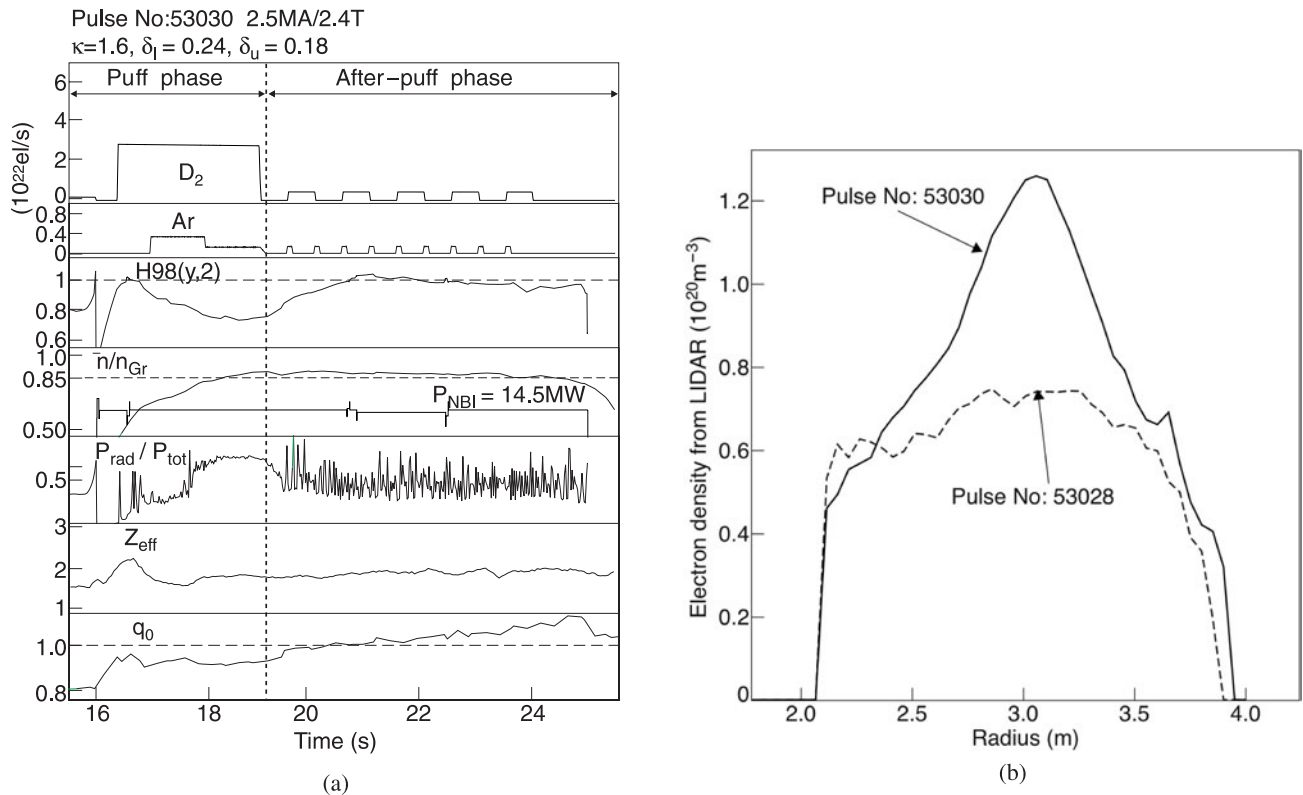

Fig. 70. (a) Illustration of the use of puff and afterpuff for the D_2 fueling in an Ar-seeded H-Mode discharge in JET. Shown as a function of time, from top to bottom, are detailed timing of the D_2 puff, detailed timing of the Ar puffing, values for the enhancement factor with respect to the H98(y,2) scaling, density values reached compared to n_{Gr}, radiative power fraction P_{rad}/P_{tot}, Z_{eff} values, and the value for the safety factor on axis. (From Ref. 267.) (b) Illustration of the density peaking observed with Ar seeding in low-triangularity discharges. Density profile for the discharge of (a) taken at 22.9 s (full line) compared to a density profile taken at the same time (dashed line) from a reference discharge without Ar seeding but with the same operational parameters otherwise. (From Ref. 267.)

IPB98(y,2) confinement scaling,[13] decreasing from 1.13 to 0.76. During the D_2-puffing phase, simultaneous Ar seeding led to an increase in the radiative power level and in the plasma density, as a result of an increase in the particle confinement time during impurity seeding, as observed on TEXTOR. After the closure of the D_2 gas-fueling valve, the density did not decrease, but confinement was restored, accompanied by density peaking[277] as in the RI-mode of TEXTOR (Fig. 70b), and in this way outstanding values for the product $H_{98(y,2)} \times \overline{n_e}/n_{Gr} \sim 1.0$ at $\overline{n_e}/n_{Gr} \sim 0.9$ and radiation fractions $\gamma = P_{rad}/P_{tot}$ up to 60% were reached. These values could last for three to four confinement times. This phase is called the "after-puff" phase in what follows. During this afterpuff phase, careful Ar and D_2 puffing was applied to keep the radiation level and the plasma density as constant as possible. For the discharges under consideration, most of the radiation was localized in the edge and not in the divertor and/or X-point, typically $P_{divertor}/P_{tot} \sim 15$ to 20% for impurity-seeded ELMy H-mode shots in the septum configuration. Ar seeding is more adapted to the JET plasma parameters than Ne, since the latter leads to a higher Z_{eff} for a given radiation level. However, for large values of Ar seeding, we observe central radiation and large degradation of confinement. This coincides with disappearing sawteeth as $q(0)$ evolves above unity. Central ICRH was therefore used to maintain $q(0) < 1$, maintaining sawtooth activity, avoiding central accumulation, and leading to stationary conditions for up 10 confinement times,[269] although with a mild ($\sim$10%) reduction in confinement. This procedure is now routinely used in JET for control of central impurity and density peaking in ELMy H-modes.

For the high-triangularity configurations, the situation is different. From previous experiments on JET it was known that confinement degrades when raising density toward n_{Gr} but also that this degradation occurs at a higher density when the triangularity is increased: In this case, large continuous D_2-fueling rates are less detrimental for confinement. Therefore, a puff/afterpuff scheme was not really necessary in these configurations. An example of such a scenario is shown in Fig. 71. Small amounts of Ar were seeded in these discharges with large heating power (with respect to the L-H power threshold) and in combination with continuous large D_2 fueling. The X-point here was well above the septum, and the strike points lay at different heights on the vertical target plates. These plasmas were obtained at $I_p = 2.3$ MA, $B_T = 2.4$ T, $q_{95} \approx 3.05$, $P_{NBI} \approx 14$ MW, and $P_{ICRH} \approx 2$ MW. In this case, seeding of Ar (starting at 20 s) enhanced the particle confinement time and led to a continuous rise of the density to even higher values. Z_{eff} was slightly increased ($\Delta Z_{eff} = 0.2$), and there was a slight confinement penalty ($\Delta H_{98(y,2)} \sim 5\%$) with $H_{98(y,2)}$ nevertheless remaining close to unity. Simulation of Ar transport in these discharges with a 1-D model[278] shows that the Ar concentration remains low in the center and peaks at the edge, thus establishing a radiative mantle.[268] The
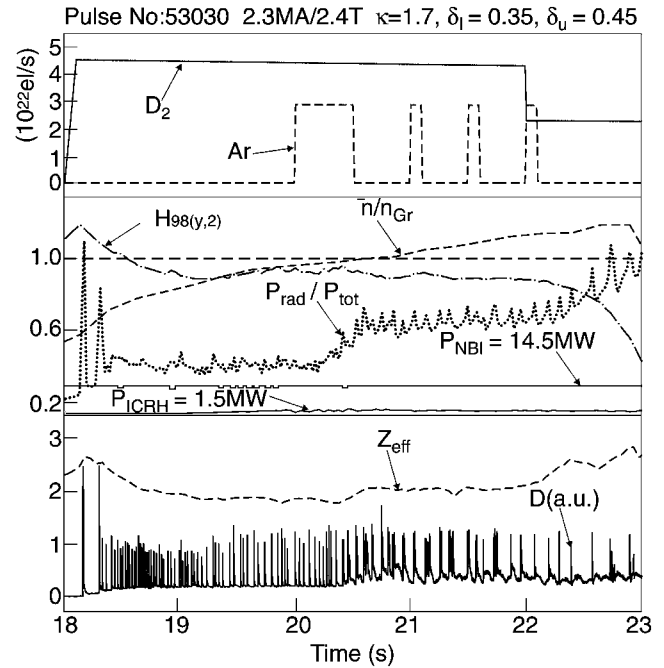

Fig. 71. Illustration of impurity seeding in high-triangularity discharges. The puff/afterpuff scheme for D_2 fueling is no longer applied. Shown as a function of time are (from top to bottom) the D_2 and Ar puffing scheme; $H_{98(y,2)}$, n/n_{Gr}, and P_{rad}/P_{tot} values obtained, together with the applied ICRH and NBI power; and Z_{eff} values reached and intensity of the D_α line. (From Ref. 267.)

contribution of Ar to the increase of the total plasma density, as deduced from the Ar concentration profile (from charge-exchange measurements), was less than 2%. Peak values simultaneously obtained in these discharges were $H_{98(y,2)} = 0.9$, $\beta_N = 2.1$, and $\overline{n_e} = 1n_{Gr}$ at a radiated power fraction of up to 70%.

VIII.E. Feedback Control of D and Ar Puffs

The experiments discussed above demonstrated the potential benefits of Ar seeding as an integrated scenario. A major concern in those scenarios, however, was the stationarity of the discharge: Main plasma parameters were indeed very sensitive not only to the Ar-seeding rate but also to the D_2-fueling rate. Indeed, increasing the D_2 refueling helped to slow down the decrease of density but at the expense of a degradation of $H_{98(y,2)}$. Furthermore, Ar and D puffs were not totally independent as actuators: Ar puffing increased the particle confinement time (as discussed above) and thus also helped to raise the density. This sensitivity of the confinement to Ar and D_2 puffing made it difficult to predict the necessary main and impurity gas rates and pointed to the need for a feedback system for their control.
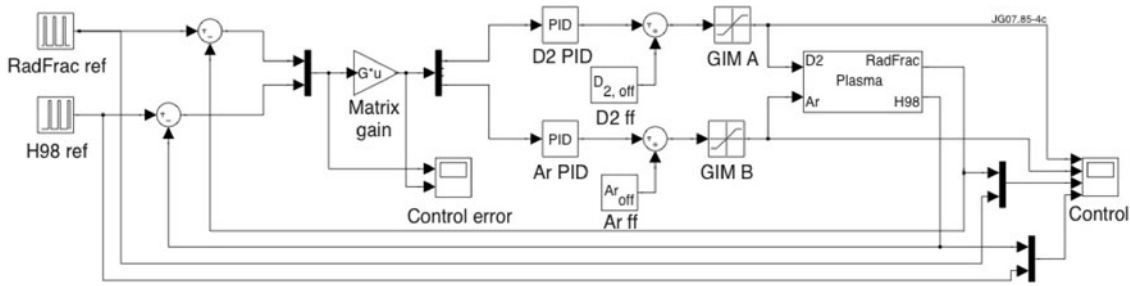
Fig. 72. Principle of the dual-feedback control. Confinement and radiated power fraction are estimated in real time and compared to the requested values. The error signals are treated by a 2 × 2 matrix and the outputs are the control voltages for the differential gas injection modules (GIMs). PIDs are used to adapt the dynamics of the response. An offset corresponding to the operating point values is added together with minimum and maximum values that are allowed for the GIM voltages controlling the GIM valve opening. (From Ref. 279.)

A dual-feedback system was developed to control both the values of $H_{98(y,2)}$ and $\gamma = P_{rad}/P_{tot}$, with the D_2-fueling rate and the Ar-seeding rate as actuators.[279] Confinement and radiation were chosen as control parameters. The technique also allows the D_2-fueling rate to be maximized for a given confinement and radiation. The feedback scheme uses a 2 × 2 control matrix, which is established from open-loop experiments with step changes in the actuators around a given operational point. The system is thus valid around this chosen operational point. The plasma model—essentially described by this matrix—is then tested on several discharges from the existing database. If the plasma model is found to be satisfactory, it is implemented in the feedback loop (Fig. 72) to test the stability of the scheme and optimize the loop. Once the open-loop system has been tested fully, the feedback loop can be closed and used in real situations.

VIII.F. Impurity Seeding in ELMy H-Mode Discharges with Trace T Using the Dual-Feedback Control Scheme

The dual-feedback control scheme was applied to high-triangularity discharges during the trace tritium campaign.[279] Figure 73 shows an example of two discharges with and without Ar seeding (and with a T puff at 20 s). In the Ar-seeded discharge, dual feedback on $H_{98(y,2)}$ and γ was used. In the reference discharge, a single feedback on $H_{98(y,2)}$ with the D_2-fueling rate as actuator was used. Both discharges had the same operational parameters otherwise. Performance of the Ar-seeded discharge was as follows: $H_{98(y,2)} \approx 1$, $f_{Gr} \approx 1$, $\beta_N \approx 2$, and $P_{rad}/P_{tot} \approx 0.65$. The neutron yield was lower for the Ar-seeded discharge because its higher density led to both a larger off-axis beam absorption and a reduction in the electron temperature, which in turn led to a reduced beam-thermal component in the neutron yield. There was no increase in Z_{eff}. Note that discharges with similar density and confinement performance could also be achieved without Ar

seeding.[257] The advantage of impurity seeding in this case is that it allows one to increase additionally the edge radiation without detrimental effects on confinement.

Transport analysis of T using its temporal evolution as measured along different viewing lines of the vertical and horizontal neutron cameras in JET (Ref. 280) combined with TRANSP calculations[281] shows a reduction of T diffusion coefficient in the central part of the plasma ($\rho < 0.5$) from $D_T \sim 0.65$ m²/s in the reference case to $D_T \sim 0.25$ m²/s in the Ar-seeded discharge, which is very close to the neoclassical value.[281] The plasma density increased by 20% with the same D source when Ar was injected. Values for χ_{eff} are reduced from 2 to 3 m²/s for the discharge without Ar seeding to 1 m²/s with Ar seeding in the gradient zone ($0.45 < \rho < 0.6$) due to reduced ion thermal diffusivity. As can be seen from Fig. 73, the total radiated power fraction was not significantly larger with Ar seeding. This was due to the high intrinsic radiation inherent to the HT3 configuration[138] used with the MkIISRP divertor (in contrast to the EHT configuration[18] used with the MkIIGB divertor discussed above). In this case the extrinsic radiation partly replaced the intrinsic radiation and the total radiation was not changed much. This led to the choice of another control parameter in subsequent experiments: the partial radiated power fraction $\gamma_u = P_{rad,u}/P_{tot}$, where $P_{rad,u}$ is an estimate of the radiated power in the main chamber, i.e., not taking into account X-point nor divertor radiation. This feedback scheme was successfully tested with steps in the requested values around the operating point.

VIII.G. Influence of Impurity Seeding on ELMs

The presence of the impurity not only increases radiation but can also change the character of the ELMs. Indeed, a difference has been observed in the effect of the impurity on the character of the ELMs if applied during the D_2-puffing phase or during the afterpuff. Ar or Ne seeding applied during the main D_2-puffing phase could
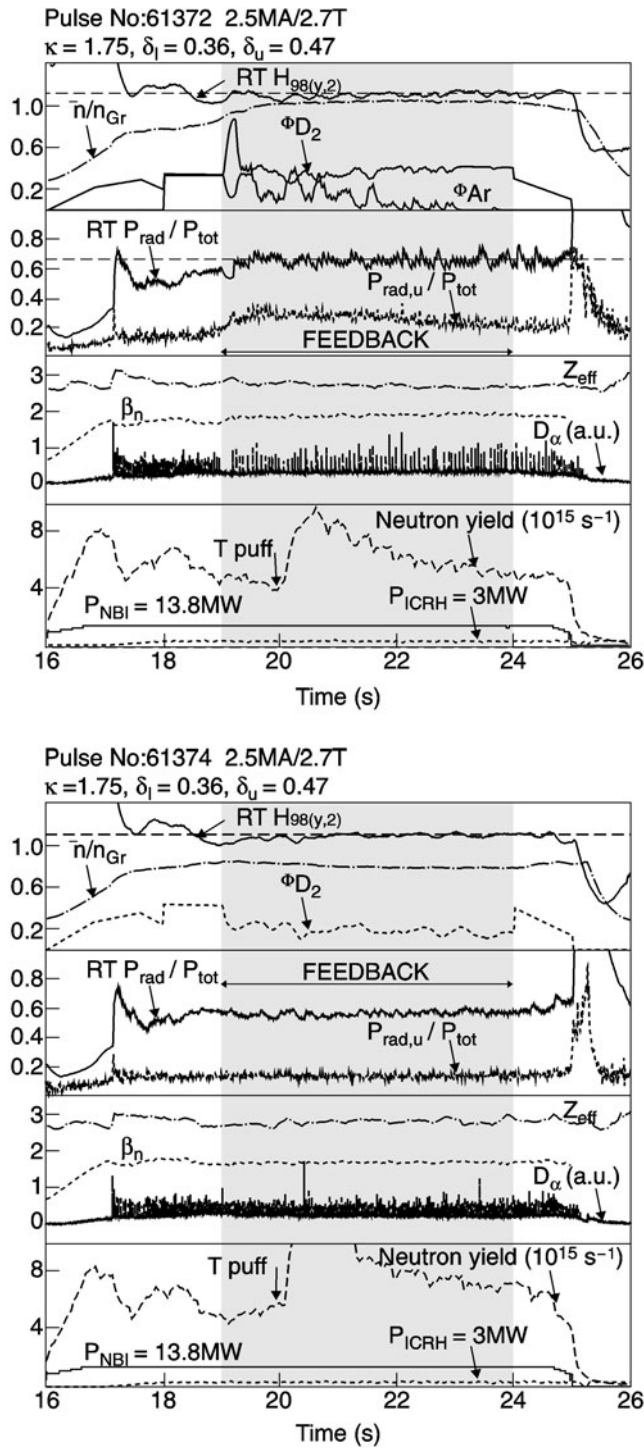
Fig. 73. Time traces of global plasma parameters in discharges with T puff. Ar-seeded discharge with dual-feedback control of D_2 and Ar (top) and reference discharge without Ar with single-feedback control for D_2 only (bottom). RT $H_{(98y,2)}$ and RT P_{rad}/P_{tot} are the real-time signals used in the feedback control. Requested values for the feedback control $H_{98(y,2)} = 1.1$ and $P_{rad}/P_{tot} = 0.65$ are indicated by the dashed horizontal lines. Time during which the feedback control is active is indicated by the shaded area. (From Ref. 279.)

change the ELMs from type I to more benign high-frequency type III ELMs. Surprisingly, impurity seeding applied in the afterpuff gave rise to opposite effects, reducing the frequency of type I ELMs, and could, with sufficient Ar seeding, lead to intermittent ELM-free phases. In those pulses we did see an impurity accumulation in the center but no clear correlation with ELM frequency or size.[269] However, as mentioned earlier, this impurity accumulation can be counteracted using central heating of the plasma by, for example, ICRH (Refs. 269 and 282). Analysis of the ELM energy losses in type I ELMy H-modes from several divertor tokamaks shows that with increasing plasma collisionality in the edge, the relative ELM size ($\Delta W_{ELM}/W_{ped}$) decreases.[158] Adding impurities in the edge offers a means to change the edge collisionality. Impurity seeding in this way could be an additional knob to change the behavior of ELMs, opening the way to optimizing the properties of the H-mode.[283]

VIII.H. Effect of Impurity Seeding on the Temperature of the Divertor Target Plate

Figure 74a compares in the low-triangularity DOC-L configuration (optimized for infrared measurement) a series of vertical temperature profiles on the inner and outer target plates "during" and "in between" ELMs for discharges with and without Ar seeding.[267,284] This series consists of 15 consecutive ELMs extracted from infrared measurements during the afterpuff phase (21 to 22 s). A significant reduction of the temperature of the target plates during ELMs is observed with Ar. Furthermore, between ELMs the temperature of the target plates at the strike point is lowered due to the increase of γ, as shown in Fig. 74b. A first decrease of the base temperature of the outer target plates is observed in the puff phase (with degraded confinement), where γ is the highest. In the afterpuff phase, the slope of the temperature rise on the outer tile is lower with Ar seeding, corresponding to a reduced power flux to the tile. This decrease of the base temperature of the target plates and of its excursion due to the ELMs with enhanced radiation contributes to reducing the erosion of the target plates.

VIII.I. Impurity Seeding in L-Mode Plasmas in JET

The temporal evolution of a neon-seeded L-mode discharge is shown in Fig. 75 (Refs. 285 and 286). Neon seeding was applied during the current ramp and q_{95} reached ~ 4.1 at current flattop (Fig. 75e). Remarkably, a doubling of the core ion temperature (Fig. 76a) compared to reference (no neon) discharges was seen, the radiated power fraction increased to 0.5 or more after the neon pulse (Fig. 75b), and confinement was at or above the H97y ELMing H-mode value (Fig. 75c). Even though Z_{eff} was higher with neon seeding, the measured neutron rate increased nevertheless (Fig. 75d). Thermal neutrons, calculated by the TRANSP code, showed a
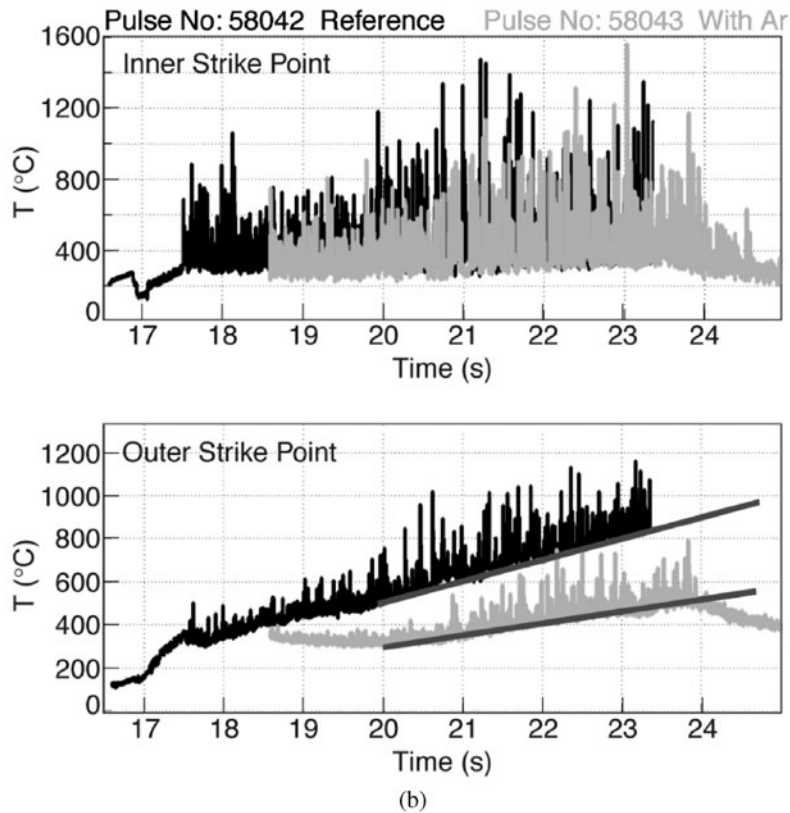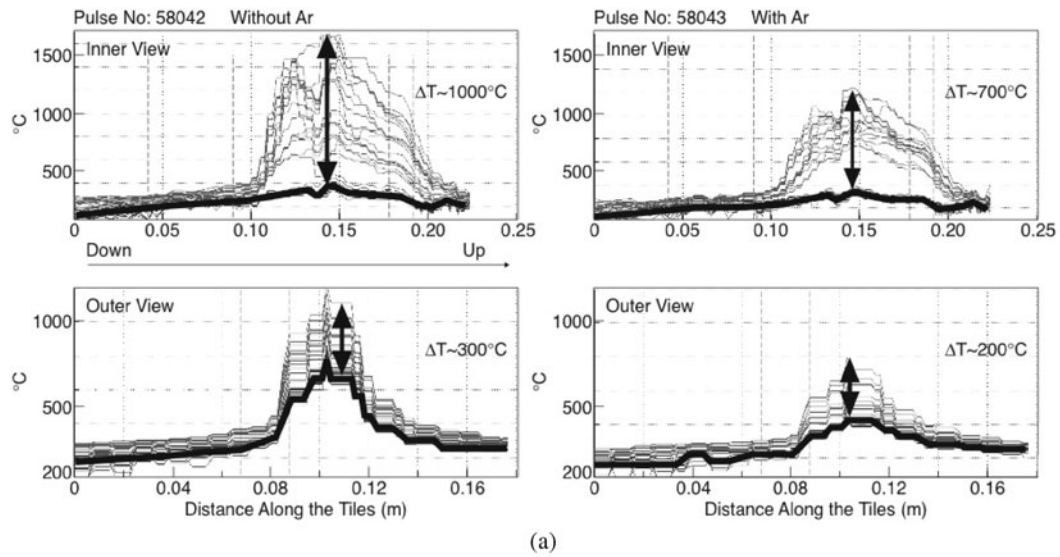
Fig. 74. (a) Vertical temperature profiles measured by infrared thermography on inner (top) and outer (bottom) target plates in an unseeded reference discharge (58042, left) and an Ar-seeded discharge (58043, right). Series of 15 consecutive ELMs during the afterpuff phase (21 to 22 s). Values measured in between ELMs are indicated by the thick black line, values during ELMs in gray. (b) Temperature at inner (top) and outer (bottom) strike points in an unseeded reference discharge (58042, black) and in an Ar-seeded discharge (58043, gray). (From Ref. 284.)

dramatic increase (up to a factor of 3) compared to a reference discharge. Profiles of the discharges in Fig. 75 are shown in Fig. 76 during times when effects of neon seeding were well established (at 44.8 s). These dis-

charges show an increase in the ITG, $-dT_i/d\rho$, at $\rho \sim 0.35$ (JET). Thermal diffusivities, calculated by the TRANSP code, show within the region of higher temperature gradient a clear decrease, and the plasma
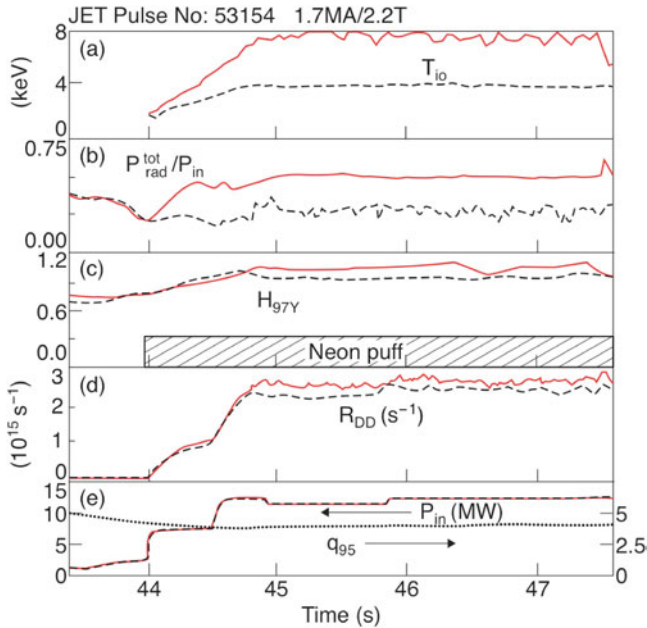
Fig. 75. Temporal evolution of JET neon-seeded discharge (53154, solid lines) together with a reference discharge (53156, dotted lines). Plotted are: (a) $T_i(0)$, (b) radiated power fraction, (c) H_{97y} confinement enhancement factor, (d) total measured neutron rate, and (e) additional heating power. Safety factor q_{95} is also shown in (e) as a dotted line. (From Ref. 285.)
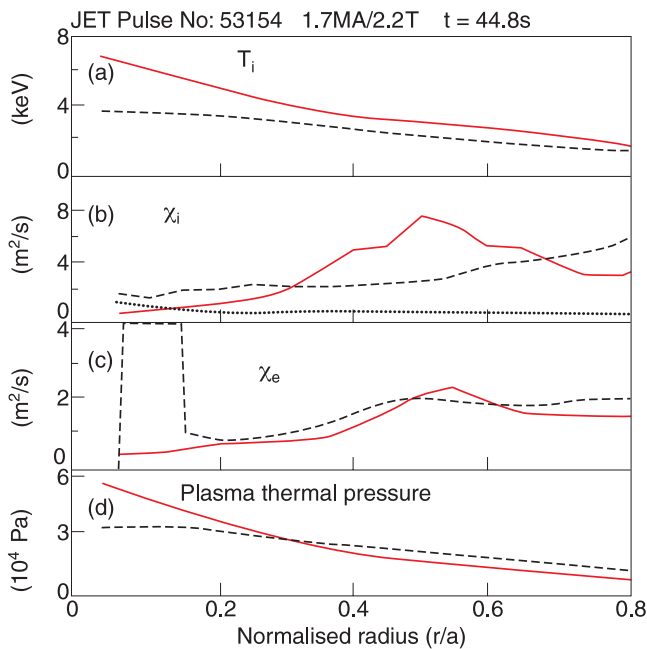

Fig. 76. Profiles of (a) T_i, (b) χ_i, (c) χ_e, and (d) plasma thermal pressure for the discharge of Fig. 75 at 44.8 s. Ion neoclassical diffusivity is shown as a dotted line in (b). The reference discharge (no neon) is shown by the dashed lines. (From Ref. 285.)

thermal pressure (Fig. 76d) is generally higher than that of the reference discharge, consistent with the lower transport in the neon-seeded cases.

Recently, first observations of improved confinement have been made in advanced-mode plasmas, at high additional heating powers up to 30 MW, showing changes in ion temperature, neutron production, and plasma beta very similar to those of the L-mode discharges discussed above. The reasons for the confinement changes are under investigation.

VIII.J. Conclusions

An integrated scenario, combining good confinement and providing a substitute for the intrinsic radiation in tokamaks with a C wall, will be needed for ITER and future fusion power reactors with a metallic wall. Therefore, experiments have been undertaken at JET (and various other tokamaks around the globe) to study the properties of plasmas with impurity seeding by noble gases.

In JET, ELMy H-mode and L-mode discharges have been studied with impurity seeding by Ne or Ar. In these discharges we have been able to create a radiative mantle keeping good confinement $H_{98(y,2)}$ at high values of P_{rad}/P_{tot}, β_N, and f_{Gr}. This was possible in both low- and high-triangularity configurations by applying careful puffing of main and impurity gases. Generally, we observe improved particle confinement, allowing us to access higher densities without loss of energy confinement for high-triangularity H-mode plasmas with Ar and L-mode with Ne. This is possible thanks to a reduction of ion heat transport by a partial suppression of the ITG modes.[277,287] Simulations of these discharges with the Jülich RITM model[288] and the Chalmers model[289,290] show good agreement with the measured particle energies and densities.[291] Confinement changes observed by seeding of Ar in low-triangularity septum discharges came closest to RI-mode effects in TEXTOR, with density peaking and recovery of improved confinement. A summary plot showing peak values of $H_{98(y,2)}$ versus f_{Gr} is shown in Fig. 77. This figure shows that discharges obtained with Ar seeding can lead to further improvement in both density and confinement quality of the best-performing ELMy H-Mode discharges in JET (i.e., those with high triangularity). This clearly illustrates the potential of this scenario.

A feedback control system for seeding of the impurities has been developed in order to maintain stationary discharge conditions. Impurity seeding has led to reduced heat flows to the divertor, as observed by infrared, thermocouple, and Langmuir probe measurements.[161] Mitigation of the ELMs by impurity seeding is not observed,[228] but peak temperatures reached during the ELM can be reduced, however, by lowering of the temperature of the divertor targets owing to enhanced radiation. Impurity seeding in ELMing H-mode discharges often also
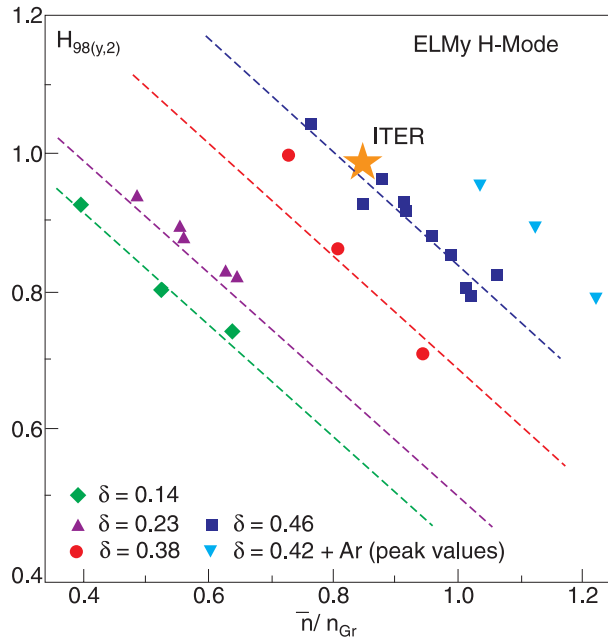
Fig. 77. Summary plot of JET unseeded ELMy H-mode discharges at various triangularities. The ITER value is indicated by the star. Inverted triangles indicate the peak values obtained during Ar-seeded ELMy H-mode discharges, showing the potential of this scenario. Electron density was taken from the interferometry diagnostic[42] both for n_e and in the calculation of $H_{98(y,2)}$. Many of the discharges in this plot are common to Fig. 5. Small differences in the values between these plots are due to the different density measures used. (From Ref. 267.)

leads to a change in ELM behavior, and type I ELMs can be transformed into type III or mixed type ELMs, with reduced amplitude, further contributing to a reduced heat flux to the divertor targets.

IX. CONCLUSIONS AND FUTURE WORK

JET experimental studies have made a major contribution to the physics basis for the ELMy H-mode scenario. Through it, they have influenced the choice of a high-triangularity, high-density, ELMy H-mode as the baseline scenario for ITER. Obtaining a stationary plasma that extrapolates to an ITER discharge with good confinement and tolerable ELMs has been identified as the most crucial issue. Planned upgrades and future experiments will focus on expanding this physics basis still further, both to increase the confidence in extrapolations to ITER and to develop new regimes of interest to ITER, particularly with regard to those with low ELM energy losses.

The key physics parameters on which the energy confinement time and L-H transition are dependent have been determined, and in conjunction with other machines, the energy confinement time and L-H power scalings with these parameters have been derived. However, several outstanding issues remain. The dependence of energy confinement time on ELM type is not well understood, and the scaling of energy confinement time with β_N, crucial for assessing the effectiveness of high-β_N operation on ITER, remains to be determined. Core confinement appears to be consistent with models based on electrostatic drift wave turbulent transport, but as yet no theory-based model can reliably predict the observed confinement. An empirical scaling or physics-based model that describes the dependence of the L-H power threshold on density at low density and on strike point configuration and triangularity remains to be found.

The global plasma energy has been found to be strongly correlated with the pedestal energy, indicating the importance of the pedestal conditions in determining the global properties of the ELMy H-mode. Pedestal studies have determined the scalings of the edge plasma pressure with local parameters for the observed ELM types on JET. For both type I and type III ELMy H-modes these have been found to be in broad agreement with physics models based on ELMs driven by edge-localized MHD modes. The characteristic MHD modes associated with ELMy H-modes on JET have also been identified as peeling-ballooning modes. Washboard modes, which were observed first on JET, are also particularly important since they are associated with enhanced inter-ELM transport in the low ELM loss, type II ELMy H-modes.

JET has provided a major contribution to the identification of the scaling of ELM particle and energy losses. The energy loss per ELM has been observed to correlate positively with the total plasma energy. The ratio of the energy loss per ELM to the total plasma energy is seen to correlate negatively with collisionality. Both of these dependencies are unfavorable for type I ELMy H-mode operation on ITER. A model describing the transport of the energy to the divertor and the main wall has also been developed and describes well the available data. Understanding the toroidal structure of ELM losses remains an outstanding issue.

Concerns over the particle and energy losses from type I ELMy H-modes have led to the investigation of ELM mitigation techniques. Several possible methods have been explored. Impurity-seeded H-modes have been produced that can be scaled to $Q \approx 10$ operation on ITER, although their performance is somewhat below that of a type I ELMy H-mode. Grassy and type II ELMy H-modes have both achieved normalized confinement times similar to those of type I ELMy H-modes. However, if they are to become possible scenarios for ITER, their operational space must be extended to more ITER-relevant conditions. ELMy H-modes with ELMs triggered by pellets and magnetic field perturbations have both shown promising results, but

further experimental work is required before they can be proposed as a reliable ITER scenario.

Planned upgrades on JET will enhance the NBI and ICRH auxiliary heating systems and increase the flexibility and control of magnetic configurations. These will increase the available operational space for the ELMy H-mode further toward the global and pedestal parameters required in ITER, not only in terms of the normalized parameters ρ^* and ν^* but also, and equally important, in absolute terms (i.e., density and temperature). This will provide better estimates for the scaling of confinement, pedestal, and ELM physics. In addition, by enabling access to higher values of β_N, it will improve predictions for ITER operation at high β_N. Enhancements to the EFCC and the pellet system will facilitate studies of active ELM control. Diagnostic upgrades will improve the diagnosis of the pedestal region, improving the determination of the local density gradient, temperature gradient, rotation, and electric fields.

Taking advantage of all of these upgrades, the future JET program will increase the validation of physics-based scalings and models in conditions that will be very close to those expected in ITER, thus reducing the uncertainty of the present extrapolations. Key to all of this will be the development of ELMy H-modes with good confinement and low ELM losses that will provide a robust scenario suitable for the ITER baseline.

REFERENCES

1. F. WAGNER et al., *Phys. Rev. Lett.*, **49**, 1408 (1982).

2. J. WESSON, *Tokamaks*, Oxford University Press, London, England (2004).

3. R. AYMAR et al. for THE ITER TEAM, *Plasma Phys. Control. Fusion*, **44**, 519 (2002).

4. P. MANTICA et al., *Fusion Sci. Technol.*, **53**, 1152 (2008).

5. R. J. BUTTERY et al., *Fusion Sci. Technol.*, **53**, 1080 (2008).

6. M. GREENWALD et al., *Nucl. Fusion*, **28**, 2199 (1988).

7. A. TANGA et al., *Proc. 11th Int. Conf. Plasma Physics and Controlled Nuclear Fusion Research*, Kyoto, Japan, IAEA-CN-47/K1-I-I (1986).

8. M. KEILHACKER et al., *Plasma Phys. Control. Fusion*, **29**, 1401 (1987).

9. P. J. LOMAS for THE JET TEAM, *Plasma Phys. Control. Fusion*, **31**, 1481 (1989).

10. B. J. D. TUBBING, *Nucl. Fusion*, **29**, 1953 (1989).

11. D. CAMPBELL et al., *Plasma Phys. Control. Fusion*, **38**, 1497 (1996).

12. L. HORTON et al., *Nucl. Fusion*, **39**, 1 (1999).

13. ITER PHYSICS BASIS EDITORS, *Nucl. Fusion*, **39**, 2175 (1999).

14. J. JACQUINOT et al., *Nucl. Fusion*, **39**, 235 (1999).

15. J. G. CORDEY et al., *Plasma Phys. Control. Fusion*, **44**, 1929 (2002).

16. G. SAIBENE et al., *Nucl. Fusion*, **39**, 1133 (1999).

17. J. ONGENA et al., *Plasma Phys. Control. Fusion*, **43**, A11 (2001).

18. G. SAIBENE et al., *Plasma Phys. Control. Fusion*, **44**, 1769 (2002).

19. D. C. McDONALD et al., *Plasma Phys. Control. Fusion*, **46**, A215 (2004).

20. A. LOARTE et al., *Plasma Phys. Control. Fusion*, **45**, 1549 (2003).

21. W. FUNDAMENSKI et al., *Fusion Sci. Technol.*, **53**, 1023 (2008).

22. G. SAIBENE et al., *Nucl. Fusion*, **45**, 297 (2005).

23. J. RAPP et al., *Plasma Phys. Control. Fusion*, **44**, 639 (2002).

24. P. LANG et al., *Nucl. Fusion*, **47**, 754 (2007).

25. Y. LIANG et al., *Plasma Phys. Control. Fusion* (to be submitted).

26. P. J. LOMAS for THE JET TEAM, "High Fusion Performance ELM Free H-Modes and the Approach to Steady Operation," *Fusion Energy 1996*, Montréal, Canada, Vol. 1, p. 239, IAEA, Vienna (1997).

27. C. C. CHALLIS et al., *Nucl. Fusion*, **33**, 1097 (1993).

28. N. DELIYANIKIS et al., *Plasma Phys. Control. Fusion*, **36**, 1159 (1994).

29. W. SUTTROP et al., *Nucl. Fusion*, **45**, 721 (2005).

30. R. J. BICKERTON et al., *Plasma Phys. Control. Fusion*, **26**, 1355 (1984).

31. R. J. BICKERTON et al., *Plasma Phys. Control. Fusion*, **28**, 55 (1986).

32. A. AINSWORTH et al., *Plasma Phys. Control. Fusion*, **28**, 1943 (1986).

33. J. WESSON, "The Science of JET," JET-R(99) 13 (1999).

34. R. J. GOLDSTON et al., *Plasma Phys. Control. Fusion*, **26**, 87 (1984).

35. P. H. REBUT et al., "The Critical Temperature Gradient Model of Plasma Transport: Applications to JET and Future Tokamaks," *Proc. 12th IAEA Conf. Fusion Energy*, Nice, France, IAEA-CN-50/D-IV-1 (1988).

36. J. G. CORDEY et al., *Nucl. Fusion*, **35**, 101 (1995).

37. J. G. CORDEY et al., *Nucl. Fusion*, **35**, 505 (1995).

38. B. B. KADOMTSEV, *Plasma Phys. Control. Fusion*, **34**, 1931 (1992).

39. X. GARBET, *Phys. Plasmas*, **3**, 1898 (1996).

40. V. NAULIN, *Phys. Plasmas*, **12**, 122306 (2005).

41. C. GORMEZANO et al., *Fusion Sci. Technol.*, **53**, 958 (2008).

42. G. BRAITHWAITE et al., *Rev. Sci. Instrum.*, **60**, 2825 (1989).

43. H. SALZMANN et al., *Rev. Sci. Instrum.*, **59**, 1451 (1988).

44. M. G. VON HELLERMAN et al., *Rev. Sci. Instrum.*, **61**, 3479 (1990).

45. P. D. MORGAN et al., *Rev. Sci. Instrum.*, **56**, 862 (1985).

46. P. BURATTI and M. ZERBINI, *Rev. Sci. Instrum.*, **66**, 4208 (1996).

47. D. V. BARTLETT et al., in *Electron Cyclotron Emission and Electron Cyclotron Resonance Heating*, Borrego Springs, California, Vol. EC-9, p. 511, World Scientific Publishing, Singapore (1995).

48. E. DE LA LUNA et al., *Rev. Sci. Instrum.*, **75**, 3831 (2004).

49. R. BARTIROMO et al., *Rev. Sci. Instrum.*, **60**, 237 (1989).

50. L.-G. ERIKSSON et al., *Plasma Phys. Control. Fusion*, **39**, 27 (1997).

51. L. C. INGESSON et al.*, J. Nucl. Mater.*, **313–316**, 1173 (2003).

52. P. VAN BELLE and G. J. SADLER, in *1986 Basic and Advanced Diagnostic Techniques for Fusion Plasmas*, Varenna, Italy, Vol. III, p. 767, EUR 10797 EN (1986).

53. D. P. O'BRIEN et al., *Nucl. Fusion*, **32**, 1351 (1992).

54. JET JOINT UNDERTAKING, Progress Report, Vol. 1, p. 76 (1994).

55. J. BLUM et al., *Nucl. Fusion*, **30**, 1475 (1990).

56. C. C. CHALLIS et al., *Nucl. Fusion*, **29**, 563 (1989).

57. L.-G. ERIKSSON et al., *Nucl. Fusion*, **33**, 1037 (1993).

58. G. M. FISHPOOL et al., *Nucl. Fusion*, **38**, 1373 (1998).

59. M. KEILHACKER for THE JET TEAM, *Plasma Phys. Control. Fusion*, **37A**, 3 (1995).

60. M. KEILHACKER for THE JET TEAM, *Nucl. Fusion*, **41**, 1925 (2001).

61. V. V. PARAIL et al., "Integrated Predictive Modeling of JET H-Mode Plasmas with Type I ELMs," *Proc. 27th EPS Conf. Controlled Fusion and Plasma Physics*, Budapest, Hungary (2000).

62. A. KALLENBACH et al., *Nucl. Fusion*, **42**, 1184 (2002).

63. P. J. LOMAS et al., *Plasma Phys. Control. Fusion*, **42**, B115 (2000).

64. A. TIBONE et al., *Nucl. Fusion*, **33**, 1319 (1993).

65. J. G. CORDEY for the ITER CONFINEMENT DATABASE AND MODELING GROUP, *Plasma Phys. Control. Fusion*, **39**, B115 (1997).

66. J. G. CORDEY et al., *Nucl. Fusion*, **39**, 301 (1999).

67. D. C. McDONALD et al., *Plasma Phys. Control. Fusion*, **46**, 519 (2004).

68. J. RAPP et al., *J. Nucl. Mater.*, **313–316**, 524 (2003).

69. R. A. PITTS et al., *J. Nucl. Mater.*, **313–316**, 777 (2003).

70. M. VALOVIČ et al., *Plasma Phys. Control. Fusion*, **44**, 1911 (2002).

71. L. HORTON et al., "Pellet Fuelling and ELMy H-Mode Physics in JET," *Fusion Energy 2000*, Sorrento, Italy, IAEA, Vienna, Austria (2001) (CD-ROM file EX2/1).

72. P. T. LANG et al., *Plasma Phys. Control. Fusion*, **44**, 1919 (2002).

73. P. T. LANG et al., *Nucl. Fusion*, **42**, 388 (2002).

74. F. RYTER et al., *Nucl. Fusion*, **41**, 537 (2001).

75. K. BORRASS et al., *Nucl. Fusion*, **44**, 752 (2004).

76. J.-M. NOTERDAEME et al., *Fusion Sci. Technol.*, **53**, 1103 (2008).

77. D. F. H. START et al., *Phys. Rev. Lett.*, **80**, 4681 (1998).

78. J. LINGERTAT et al., *J. Nucl. Mater.*, **266–269**, 124 (1999).

79. V. P. BHATNAGAR et al., *Nucl. Fusion*, **39**, 353 (1999).

80. F. RIMINI and G. SAIBENE for THE JET TEAM, *Nucl. Fusion*, **42**, 86 (2002).

81. E. ASP et al., *Plasma Phys. Control. Fusion*, **47**, 505 (2005).

82. P. R. THOMAS et al., *Phys. Rev. Lett.*, **80**, 5548 (1998).

83. B. B. KADOMSTEV, *Sov. J. Plasma Phys.*, **1**, 295 (1975).

84. D. C. McDONALD et al., *Nucl. Fusion*, **47**, 147 (2007).

85. J. W. CONNOR and J. B. TAYLOR, *Nucl. Fusion*, **17**, 1047 (1977).

86. J. G. CORDEY et al., *Plasma Phys. Control. Fusion*, **38**, A67 (1996).

87. T. C. LUCE et al., "Implications from Dimensionless Parameter Scaling Experiments," *Fusion Energy 1996*, Montréal, Canada, Vol. 1, p. 611, IAEA, Vienna, Austria (1997).

88. T. C. LUCE et al., *Nucl. Fusion*, **42**, 1193 (2002).

89. K. THOMSEN et al., "Confinement Identity Experiments in ASDEX Upgrade and JET," *Proc. 25th EPS Conf. Controlled Fusion and Plasma Physics*, Prague, Czech Republic, p. 468 (1998).

90. J. P. CHRISTIANSEN et al., "Experimental Tests of Confinement Scale Invariance on JET, DIII-D, ASDEX Upgrade and CMOD," *Fusion Energy 1998*, Yokohama, Japan, IAEA, Vienna (2001) (CD-ROM file EXP2/02).

91. C. C. PETTY et al., *Plasma Phys. Control. Fusion*, **46**, A207 (2004).

92. H. LEGGATE et al., "The Significance of the Dimensionless Collisionality and the Greenwald Fraction in the Scaling of Confinement," *Proc. 32nd EPS Conf. Controlled Fusion and Plasma Physics*, Tarragona, Spain (2005).

93. G. SAIBENE et al., *Plasma Phys. Control. Fusion*, **46**, A195 (2004).

94. G. SAIBENE et al., "Toroidal Field Ripple Effects on H-Modes in JET and Implications for ITER," *Proc. 34th EPS Conf. Controlled Fusion and Plasma Physics*, Warsaw, Poland (2007).

95. N. OYAMA et al., "Effect of Toroidal Field Ripple and Toroidal Rotation on H-Mode Performance and ELM Characteristics in JET/JT-60U Similarity Experiments," *Proc. 11th IAEA Technical Mtg. H-Mode Physics and Transport Barriers*, Tsukuba, Japan, P2-11 (2007).

96. C. C. PETTY et al., *Phys. Plasmas*, **2**, 2342 (1995).

97. J. G. CORDEY for THE JET TEAM, "Energy Confinement and H-Mode Power Threshold Scaling in JET with ITER Dimensionless Parameters," *Fusion Energy 1996*, Montréal, Canada, Vol. 1, p. 603, IAEA, Vienna (1997).

98. ITER H-MODE DATABASE WORKING GROUP, in *Proc. 20th EPS Conf. Controlled Fusion and Plasma Physics*, Lisbon, Portugal, Vol. 17C, Part I, p. 15, European Physical Society, Geneva, Switzerland (1993).

99. D. C. McDONALD et al., "Particle and Energy Transport in Dedicated Dimensionless Parameter Scans in JET ELMy H-Modes," *Plasma Phys. Control. Fusion* (in preparation).

100. C. C. PETTY et al., *Phys. Plasmas*, **11**, 2514 (2004).

101. J. P. CHRISTIANSEN and J. G. CORDEY, *Nucl. Fusion*, **38**, 1757 (1998).

102. C. C. PETTY et al., *Nucl. Fusion*, **38**, 1183 (1998).

103. H. URANO et al., *Nucl. Fusion*, **46**, 781 (2006).

104. L. VERMARE et al., *Nucl. Fusion*, **47**, 490 (2007).

105. C. C. PETTY et al., *Fusion Sci. Technol.*, **43**, 1 (2003).

106. J. G. CORDEY et al., *Plasma Phys. Control. Fusion*, **42**, A127 (2000).

107. J. A. SNIPES for THE ITPA CONFINEMENT AND H-MODE THRESHOLD DATABASE WORKING GROUP, "Multi-Machine Global Confinement and H-Mode Threshold Analysis," *Proc. 19th IAEA Fusion Energy Conf.*, Lyon, France, paper IAEA-ITERCT-P/04 (2002).

108. S. J. FIELDING et al., *Plasma Phys. Control. Fusion*, **38**, 1091 (1996).

109. S. J. FIELDING et al., *Plasma Phys. Control. Fusion*, **40**, 731 (1998).

110. T. FUKUDA et al., *Nucl. Fusion*, **37**, 543 (1997).

111. A. E. HUBBARD et al., *Plasma Phys. Control. Fusion*, **40**, 689 (1998).

112. T. N. CARLSTROM and R. J. GROEBNER, *Phys. Plasmas*, **3**, 1867 (1996).

113. F. RYTER for THE H-MODE THRESHOLD DATABASE GROUP, *Plasma Phys. Control. Fusion*, **44**, A415 (2002).

114. L. D. HORTON et al., "Dependence of the H-Mode Threshold on the JET Divertor Geometry," *Proc. 26th EPS Conf. Controlled Fusion and Plasma Physics*, Maastricht, The Netherlands, June 14–18, 1999, P1.021 (1999).

115. E. RIGHI et al., *Plasma Phys. Control. Fusion*, **42**, A199 (2000).

116. R. SARTORI et al., *Plasma Phys. Control. Fusion*, **46**, 723 (2004).

117. Y. ANDREW et al., *Plasma Phys. Control. Fusion*, **48**, 479 (2006).

118. YU. IGITKHANOV et al., "The L-H Transition in Low Density Regimes," *Proc. 27th EPS Conf. Controlled Fusion and Plasma Physics*, Budapest, Hungary, June 12–16, 2000, Vol. 24B, p. 1156, ECA (2000).

119. M. Z. TOKAR, *Plasma Phys. Control. Fusion*, **36**, 1819 (1994).

120. D. KALUPIN et al., "Influence of Convective Heat Losses on the H-Mode Power Threshold," *Proc. 33rd EPS Conf. Controlled Fusion and Plasma Physics*, Rome, Italy, June 19–23, 2006, EFDA-JET-CP(06)03-34 (2006).

121. L. D. HORTON, *Plasma Phys. Control. Fusion*, **42**, A37 (2000).

122. Y. ANDREW et al., *Plasma Phys. Control. Fusion*, **46**, A87 (2004).

123. S. TODA, S.-I. ITOH, M. YAGI, and Y. MIURA, *Plasma Phys. Control. Fusion*, **39**, 301 (1997).

124. Y. ANDREW et al., *Plasma Phys. Control. Fusion*, **46**, 337 (2004).

125. W. SUTTROP et al., *Plasma Phys. Control. Fusion*, **39**, 2051 (1997).

126. T. N. CARLSTROM et al., *Plasma Phys. Control. Fusion*, **40**, 669 (1998).

127. F. RYTER et al., *Plasma Phys. Control. Fusion*, **40**, 725 (1998).

128. J. W. HUGHES et al., *Fusion Sci. Technol.*, **51**, 317 (2007).

129. C. GOWERS et al., *J. Plasma Fusion Res.*, **76**, 874 (2000).

130. M. KEMPENAARS et al., "Edge Gradient and Pedestal Measurements of ELMy H-Mode Plasmas at JET," *Proc. 30th EPS Conf. Controlled Fusion and Plasma Physics*, St. Petersburg, Russia (2003).

131. R. PASQUALOTTO et al., *Rev. Sci. Instrum.*, **75**, 3891 (2004).

132. O. POGUTSE and E. I. YURCHENKO, *Rev. Plasma Phys.*, **2**, 65 (1986).

133. A. LOARTE et al., "Influence of Toroidal Field Direction and Plasma Rotation on Pedestal and ELM Characteristics in JET ELMy H-Modes," *Proc. 32nd EPS Conf. Controlled Fusion and Plasma Physics*, Tarragona, Spain (2005).

134. E. J. DOYLE et al., *Phys. Fluids B*, **3**, 2300 (1991).

135. J. STOBER et al., *Nucl. Fusion*, **41**, 1123 (2001).

136. Y. KAMADA and THE JT-60U TEAM, *Nucl. Fusion*, **41**, 1311 (2001).

137. C. P. PEREZ et al., *Plasma Phys. Control. Fusion*, **46**, 61 (2004).

138. R. SARTORI et al., "Scaling Study of ELMy H-Mode Global and Pedestal Confinement at High Triangularity in JET," *Fusion Energy 2004*, Vilamoura, Porgutal, IAEA, Vienna, Austria (2005) (CD-ROM file EX6/3).

139. J. STOBER et al., "Small ELM Regimes with Good Confinement on JET and Comparison to Those on ASDEX Upgrade, Alcator C-Mod, and JT-60U," *Fusion Energy 2004*, Vilamoura, Portugal, IAEA, Vienna, Austria (2005) (CD-ROM file EXP1/4).

140. H. ZOHM, *Plasma Phys. Control. Fusion*, **38**, 105 (1996).

141. R. SARTORI et al., "Confinement Loss in JET ELMy H-Modes," *Proc. 26th EPS Conf. Controlled Fusion and Plasma Physics*, Maastricht, The Netherlands, ECA Vol. 23J, p. 197 (1999).

142. O. POGUTSE et al., "A Possible Physical Explanation for Type III ELMs in Tokamaks," *Proc. 26th EPS Conf. Controlled Fusion and Plasma Physics*, Maastricht, The Netherlands, Vol. 23J, p. 249 (1999).

143. YU. IGITKHANOV and O. POGUTSE, *Contrib. Plasma Phys.*, **40**, 368 (2000).

144. A. CHANKIN and G. SAIBENE, *Plasma Phys. Control. Fusion*, **41**, 913 (1999).

145. Y. SARAZIN et al., *Plasma Phys. Control. Fusion*, **44**, 2445 (2002).

146. R. SARTORI et al., *Plasma Phys. Control. Fusion*, **40**, 757 (1998).

147. J. W. CONNOR et al., *Phys. Plasmas*, **5**, 2687 (1998).

148. Y. KAMADA et al., *Plasma Phys. Control. Fusion*, **42**, A247 (2000).

149. Y. KAMADA et al., *Plasma Phys. Control. Fusion*, **44**, 1311 (2002).

150. A. LOARTE et al., *Phys. Plasmas*, **11**, 2668 (2004).

151. ITER PHYSICS BASIS EDITORS, *Nucl. Fusion*, **39**, 2137 (1999).

152. G. FEDERICI et al., *Plasma Phys. Control. Fusion*, **45**, 1523 (2003).

153. PROGRESS IN ITER PHYSICS BASIS EDITORS, *Nucl. Fusion*, **47**, S203 (2007).

154. D. J. CAMPBELL et al., *Plasma Phys. Control. Fusion*, **36**, A255 (1994).

155. J. LINGERTAT et al., *J. Nucl. Mater.*, **241–243**, 402 (1997).

156. THE JET TEAM, *Plasma Phys. Control. Fusion*, **37**, A227 (1995).

157. S. CLEMENT et al., *J. Nucl. Mater.*, **266–269**, 285 (1999).

158. R. MOHANTI et al., *Proc. 24th European Conf. Controlled Fusion and Plasma Physics*, Berchtesgaden, Germany, Vol. 21A, Part I, p. 0101 (1997).

159. A. LOARTE et al., *Plasma Phys. Control. Fusion*, **44**, 1815 (2002).

160. A. HERRMANN, *Plasma Phys. Control. Fusion*, **44**, 883 (2002).

161. A. LOARTE et al., "Predicted ELM Energy Loss and Power Loading in ITER-FEAT," *Fusion Energy 2000*, Sorrento, Italy, IAEA, Vienna, Austria (2000) (CD-ROM file ITERP/11R; available on the Internet at http://www.iaea.org/programmes/ripc/physics/fec2000/html/node1.htm).

162. H. URANO et al., "Enhanced H-Mode Pedestal and Energy Confinement by Reduction of Toroidal Field Ripple in JT-60U," *Fusion Energy 2006*, Chengdu, China, paper EX5-1 (2006).

163. A. KIRK et al., "Evolution of the Pedestal on MAST and the Implications for ELM Power Loadings," *Fusion Energy 2006*, Chengdu, China, paper EX9-1 (2006).

164. J. W. CONNOR, *Plasma Phys. Control. Fusion*, **40**, 191 (1998).

165. A. W. LEONARD et al., *Plasma Phys. Control. Fusion*, **44**, 945 (2002).

166. A. W. LEONARD et al., *Phys. Plasmas*, **10**, 1765 (2003).

167. A. KALLENBACH et al., *Plasma Phys. Control. Fusion*, **46**, 431 (2004).

168. A. LOARTE et al., "ELMs and Disruptions in ITER: Expected Energy Fluxes on Plasma-Facing Components from Multi-Machine Experimental Extrapolations and Consequences for ITER Operation," *Fusion Energy 2006*, Chengdu, China, paper IT/P1-14 (2006).

169. A. LOARTE et al., *Phys. Scripta*, **T128**, 222 (2007).

170. J. LINGERTAT et al., *Proc. 23rd EPS Conf. Controlled Fusion and Plasma Physics*, Bournemouth, United Kingdom, Vol. 19C, Part III, p. 281 (1995).

171. S. JACHMICH et al., *Proc. 28th EPS Conf. Plasma Physics and Controlled Fusion*, Madiera, Portugal, Vol. 25A, P-4.079 (2002).

172. R. D. GILL et al., *Nucl. Fusion*, **38**, 1461 (1998).

173. E. SOLANO et al., "Current Loss and Strike Point Movement During ELMs in JET," *Proc. 30th EPS Conf. Plasma Physics and Controlled Fusion*, St. Petersburg, Russia, P1.106 (2003).

174. T. EICH et al., *J. Nucl. Mater.*, **337–339**, 669 (2005).

175. R. A. PITTS et al., "ELM Transport in the JET Scrape-Off Layer," *Fusion Energy 2006*, Chengdu, China, paper EX/3-1 (2006).

176. D. TSKHAKAYA et al., *Proc. PET 11 Workshop*, Takayama, Japan (2007) (submitted for publication in *Contrib. Plasma Phys.*).

177. D. TSKHAKAYA et al., *Proc. 34th EPS Conf. Plasma Physics and Controlled Fusion*, Warsaw, Poland (2007).

178. I. NUNES et al., *Nucl. Fusion*, **44**, 883 (2004).

179. T. W. PETRIE et al., *Nucl. Fusion*, **43**, 910 (2003).

180. PH. GHENDRIH et al., *J. Nucl. Mater.*, **313–316**, 914 (2003).

181. W. FUNDAMENSKI et al., *Plasma Phys. Control. Fusion*, **48**, 109 (2006).

182. T. EICH et al., *Europhysics Conference Abstracts: 34th Conf. Controlled Fusion and Plasma Physics*, Warsaw, Poland, July 2–6, 2007, Vol. 31F, paper P-2.017, European Physical Society (2007).

183. T. EICH et al., *Plasma Phys. Control. Fusion*, **49**, 573 (2007).

184. B. GONÇALVES et al., *Plasma Phys. Control. Fusion*, **45**, 1627 (2003).

185. C. SILVA et al., *J. Nucl. Mater.*, **337–339**, 722 (2005).

186. A. KIRK et al., *Plasma Phys. Control. Fusion*, **47**, 995 (2005).

187. R. A. PITTS et al., *Nucl. Fusion*, **46**, 82 (2006).

188. W. FUNDAMENSKI et al., *Plasma Phys. Control. Fusion*, **46**, 233 (2004).

189. W. FUNDAMENSKI and R. A. PITTS, *J. Nucl. Mater.*, **363–365**, 319 (2007).

190. A. TANGA et al., *Nucl. Fusion*, **27**, 1877 (1987).

191. M. MALCARNE et al., *Plasma Physics Control. Fusion*, **29**, 1675 (1987).

192. A. HUBBARD et al., "Edge Fluctuation Measurements During *X*-Point Plasmas in JET," *Proc. 15th EPS Conf. Controlled Fusion and Plasma Physics*, Dubrovnik, Yugoslavia, Vol. II, p. 651 (1988).

193. E. LAZZARO et al., "Analysis of Current and Pressure Profiles in JET H-Mode Discharges," *Proc. 15th EPS Conf. Controlled Fusion and Plasma Physics*, Dubrovnik, Yugoslavia, Vol. I, p. 241 (1988).

194. D. P. O'BRIEN et al., "Ballooning Stability Analysis of JET H-Mode Discharges," *Proc. 16th EPS Conf. Controlled Fusion and Plasma Physics*, Venice, Italy (1989).

195. P. CRIPWELL et al., "An Interpretation of the Structure of ELMs and the H to L Transition," *Proc. 16th EPS Conf. Controlled Fusion and Plasma Physics*, Venice, Italy (1989).

196. S. ALI-ARSHAD et al., "ELM Precursors in JET," *Proc. 19th EPS Conf. Controlled Fusion and Plasma Physics*, Innsbruck, Austria, Vol. I, p. 227 (1992).

197. G. T. A. HUYSMANS, H. J. DE BLANK, W. KERNER, J. P. GOEDBLOED, and M. F. F. NAVE, "MHD Stability Models of Edge Localised Modes in JET Discharges," *Proc. 19th EPS Conf. Controlled Fusion and Plasma Physics*, Innsbruck, Austria, Vol. I, p. 247 (1992).

198. T. C. HENDER et al., "High Beta Poloidal MHD Activity in JET," *Proc. 19th EPS Conf. Controlled Fusion and Plasma Physics*, Innsbruck, Austria, Vol. I, p. 335 (1992).

199. N. DELIYANIKIS et al., "The VH-Mode at JET," *Proc. 20th EPS Conf. Controlled Fusion and Plasma Physics*, Lisbon, Portugal, Vol. I-39, p. 155 (1993).

200. P. SMEULDERS et al., "Beta Limits in H-Modes and VH-Modes," *Proc. 21st EPS Conf. Controlled Fusion and Plasma Physics*, Montpellier, France, Vol. I, p. 206 (1994).

201. T. T. C. JONES et al., *Plasma Phys. Control. Fusion*, **37**, A359 (1995).

202. T. C. HENDER et al., "Influence of Edge Instabilities on JET High Performance," *Proc. 22nd EPS Conf. Controlled Fusion and Plasma Physics*, Bournemouth, United Kingdom, Vol. I, p. 209 (1995).

203. G. T. A. HUYSMANS et al., "Influence of Edge Current Density and Pressure Gradients on the MHD Stability of Low-*n* External Kink Modes," *Proc. 22nd EPS Conf. Controlled Fusion and Plasma Physics*, Bournemouth, United Kingdom, Vol. I, p. 201 (1995).

204. M. F. F. NAVE et al., *Nucl. Fusion*, **37**, 809 (1997).

205. M. F. F. NAVE et al., *Nucl. Fusion*, **35**, 409 (1995).

206. P. SMEULDERS et al., "Influence of MHD Instabilities on JET High Performance," *Proc. 22nd EPS Conf. Controlled Fusion and Plasma Physics*, Bournemouth, United Kingdom, Vol. IV, p. 61 (1995).

207. A. B. MIKHAILOVSKII, G. T. A. HUYSMANS, W. KERNER, and S. E. SHARAPOV, "Optimisation of the Computational MHD Normal Mode Analysis in Tokamaks," JET-P(96) 25 (1996).

208. M. F. F. NAVE et al., *Nucl. Fusion*, **39**, 1567 (1999).

209. T. C. HENDER et al., "Identification of Outer Modes in JET," *Proc. 24th EPS Conf. Controlled Fusion and Plasma Physics*, Berchtesgaden, Germany, I-29 (1997).

210. G. T. A. HUYSMANS et al., *Nucl. Fusion*, **38**, 179 (1998).

211. M. F. F. NAVE et al., "I-1 Discharge Optimisation and the Control of MHD Modes," *Proc. 24th EPS Conf. Controlled Fusion and Plasma Physics*, Berchtesgaden, Germany (1997).

212. M. F. F. NAVE et al., *Plasma Phys. Control. Fusion*, **42**, A89 (2000).

213. P. BREGER et al., "Plasma-Edge Gradients and Transport Barrier Widths in L and H-Mode JET Plasmas," *Proc. 24th EPS Conf. Controlled Fusion and Plasma Physics*, Berchtesgaden, Germany, I-69 (1997).

214. P. BREGER et al., *Plasma Phys. Control. Fusion*, **40**, 347 (1998).

215. C. P. PEREZ et al., *Nucl. Fusion*, **44**, 609 (2004).

216. P. SMEULDERS et al., *Plasma Phys. Control. Fusion*, **41**, 1303 (1999).

217. J. STOBER et al., *Nucl. Fusion*, **45**, 1213 (2005).

218. M. BECOULET et al., *Plasma Phys. Control. Fusion*, **45**, A93 (2003).

219. Vl. V. BOBKOV et al., "Studies of ELM Toroidal Asymmetry Using ICRF Antennas at JET and ASDEX Upgrade," *Proc. 31st EPS Conf. Controlled Fusion and Plasma Physics*, London, United Kingdom (2004).

220. J. W. CONNOR et al., *Phys. Plasmas*, **5**, 2687 (1998).

221. J. S. LONROTH et al., *Plasma Phys. Control. Fusion*, **46**, 767 (2004).

222. T. ONJUN et al., *Phys. Plasmas*, **11**, 3006 (2004).

223. S. E. SNYDER et al., *Phys. Plasmas*, **12**, 112508 (2005).

224. S. SAARELMA et al., *Plasma Phys. Control. Fusion*, **47**, 713 (2005).

225. F. RIMINI et al., *Nucl. Fusion*, **45**, 1 (2005).

226. M. BECOULET et al., *Plasma Phys. Control. Fusion*, **44**, A103–A112 (2002).

227. I. NUNES et al., "Small ELMs in Quasi-Double Null Plasmas at JET," *Proc. 34th EPS Conf. Controlled Fusion and Plasma Physics*, Warsaw, Poland (2007).

228. T. EICH et al., *J. Nucl. Mater.*, **313–316**, 919 (2003).

229. P. MONIER-GARBET et al., *Nucl. Fusion*, **45**, 1404 (2005).

230. J. RAPP et al., *Nucl. Fusion*, **44**, 312 (2004).

231. S. JACHMICH et al., *Plasma Phys. Control. Fusion*, **44**, 1879 (2002).

232. M. MORI et al., *Plasma Phys. Control. Fusion*, **38**, 1189 (1996).

233. S. J. FIELDING et al., "ELM Control in COMPASS-D," *Proc. 28th EPS Conf. Plasma Physics and Controlled Fusion*, Funchal, Portugal, ECA, Vol. 25A, p. 1825 (2001).

234. T. EVANS et al., *Nature Phys.*, **2**, 419 (2006).

235. Y. LIANG et al., *Phys. Rev. Lett.*, **98**, 265004 (2007).

236. P. LANG et al., *Nucl. Fusion*, **44**, 665 (2004).

237. A. GERAUD et al., *Proc. 24th SOFT Conf.*, Warsaw, Poland, p. P4-H-201 (2006).

238. J. RAPP et al., *J. Nucl. Mater.*, **337–339**, 826 (2005).

239. G. F. MATTHEWS, *Nucl. Fusion*, **39**, 19 (1999).

240. J. RAPP et al., *Nucl. Fusion* (to be submitted).

241. S. A. SABBAGH et al., *Phys. Fluids B*, **3**, 2277 (1991).

242. Y. CORRE, *Europhysics Conference Abstracts 34th Conf. Controlled Fusion and Plasma Physics*, Warsaw, Poland, July 2–6, 2007, Vol. 31F, paper P-5.149, European Physical Society (2007).

243. K. BURRELL et al., *Plasma Phys. Control. Fusion*, **46**, A165 (2002).

244. M. GREENWALD et al., *Nucl. Fusion*, **37**, 793 (1997).

245. A. GIBSON and M. L. WATKINS, *Proc. 8th EPS Conf. Controlled Fusion and Plasma Physics*, Prague, Czech Republic, Vol. I, p. 31 (1977).

246. K. LACKNER and J. NEUHAUSER, *IAEA Technical Mtg. Divertors and Impurity Control*, Garching, Germany, p. 58, International Atomic Energy Agency (1981).

247. E. A. LAZARUS et al., *J. Nucl. Mater.*, **121**, 61 (1984).

248. E. A. LAZARUS et al., *Nucl. Fusion*, **25**, 135 (1985).

249. U. SAMM et al., *Proc. 18th EPS Conf. Controlled Fusion and Plasma Physics*, Berlin, Germany, Europhysics Conference Abstracts, Vol. 15C, Part III, p. 157, European Physical Society (1991).

250. U. SAMM et al., *Plasma Phys. Control. Fusion*, **35**, B167 (1993).

251. J. ONGENA et al., *Proc. 20th EPS Conf. Controlled Fusion and Plasma Physics*, Lisbon, Portugal, Vol. 17C, Part I, p. 127, European Physical Society (1993).

252. J. WINTER et al., *Phys. Rev. Lett.*, **71**, 1549 (1993).

253. A. M. MESSIAEN et al., *Nucl. Fusion*, **34**, 825 (1994).

254. A. M. MESSIAEN et al., *Phys. Rev. Lett.*, **77**, 2487 (1996).

255. A. M. MESSIAEN et al., *Phys. Plasmas*, **4**, 1690 (1997).

256. J. ONGENA et al., *Proc. 24th EPS Conf. Controlled Fusion and Plasma Physics*, Berchtesgaden, Germany, European Conference Abstracts, Vol. 21A, Part IV, p. 1693 (1997).

257. B. UNTERBERG et al., *Plasma Phys. Control. Fusion*, **39**, B189 (1997).

258. J. ONGENA et al., *Phys. Scripta*, **52**, 449 (1995).

259. M. Z. TOKAR' et al., *Plasma Phys. Control. Fusion*, **41**, L9 (1999).

260. M. Z. TOKAR' et al., *Phys. Rev. Lett.*, **84**, 895 (2000).

261. M. Z. TOKAR', *Plasma Phys. Control. Fusion*, **41**, B317 (1999).

262. J. ONGENA et al., *Plasma Phys. Control. Fusion*, **41**, A379 (1999).

263. J. ONGENA et al., *Phys. Plasmas*, **8**, 2188 (2001).

264. *Proc. Workshop on Research Programme on Radiative Modes on the Existing European Facilities*, Jülich, Germany, January 13–14, 1999.

265. *Proc. Workshop on Radiating Edge Plasmas for JET*, Abingdon, United Kingdom, June 21–23, 1999

266. J. STRACHAN et al., *Plasma Phys. Control. Fusion*, **42**, A81 (2000).

267. P. DUMORTIER et al., *Plasma Phys. Control. Fusion*, **44**, 1845 (2002).

268. M. E. PUIATTI, *Plasma Phys. Control. Fusion*, **44**, 1863 (2002).

269. M. F. F. NAVE et al., *Nucl. Fusion*, **43**, 1204 (2003).

270. G. MADISSON et al., *Nucl. Fusion*, **43**, 49 (2003).

271. U. SAMM, *Proc. 16th IEEE Symp. Fusion Engineering*, p. 470 (1995).

272. K. H. DIPPEL et al., *J. Nucl. Mater.*, **145–147**, 3 (1987).

273. R. WEYNANTS et al., *Nucl. Fusion*, **39**, 1637 (1999).

274. D. KALUPIN et al., *Plasma Phys. Control. Fusion*, **45**, 199 (2003).

275. G. MANK et al., *Phys. Rev. Lett.*, **85**, 2312 (2000).

276. D. R. MIKKELSEN, *Phys. Fluids B*, **1**, *2*, 333 (1989).

277. M. Z. TOKAR', *Plasma Phys. Control. Fusion*, **45**, 1323 (2003).

278. M. MATTIOLI et al., *J. Phys. B: At. Mol. Opt. Phys.*, **34**, 127 (2001).

279. P. DUMORTIER et al., *Proc. 31st EPS Conf. Plasma Physics*, London, United Kingdom, June 28–July 2, 2004, Europhysics Conference Abstracts, Vol. 28B, paper P-5.170 (2004).

280. K. D. ZASTROW et al., *Plasma Phys. Control. Fusion*, **46**, B255 (2004).

281. I. VOITSEKOVITCH et al., *Proc. 31st EPS Conf. Plasma Physics*, London, United Kingdom, June 28–July 2, 2004, Europhysics Conference Abstracts, Vol. 28B, paper P-1.158 (2004).

282. M. E. PUIATTI et al., *Plasma Phys. Control. Fusion*, **45**, 2011 (2003).

283. G. P. MADDISON et al., *Plasma Phys. Control. Fusion*, **45**, 1657 (2003).

284. P. DUMORTIER et al., *Proc. 30th EPS Conf. Controlled Fusion and Plasma Physics*, St. Petersburg, Russia, July 7–11, 2003, Europhysics Conference Abstracts, Vol. 27A, P-1.91 (2003).

285. G. L. JACKSON et al., *Proc. 28th EPS Conf. Controlled Fusion and Plasma Physics*, Funchal, Portugal, Europhysics Conference Abstracts, Vol. 25A, p. 993, European Physical Society (2001).

286. G. L. JACKSON et al., *Plasma Phys. Control. Fusion*, **44**, 1893 (2002).

287. M. Z. TOKAR', *Plasma Phys. Control. Fusion*, **44**, 1903 (2003).

288. M. Z. TOKAR', *Plasma Phys. Control. Fusion*, **36**, 1819 (1994).

289. J. WEILAND, in *Collective Modes in Inhomogeneous Plasmas: Kinetic and Advanced Fluid Theory*, Institute of Physics Publishing, Bristol, United Kingdom (2000).

290. P. STRAND et al., *Nucl. Fusion*, **28**, 545 (1998).

291. B. UNTERBERG et al., *Plasma Phys. Control. Fusion*, **46**, A241 (2004).